CHARACTERIZATION OF MICROSTRUCTURE OF NUCLEAR STRUCTURAL MATERIALS BY XRD

By
PRASUN SHARMA CHOWDHURY

Variable Energy Cyclotron Centre, Kolkata

A thesis submitted to the
Board of Studies in Physical Sciences

In partial fulfillment of requirements
for the Degree of
DOCTOR OF PHILOSOPHY
of
HOMI BHABHA NATIONAL INSTITUTE

September, 2011

Homi Bhabha National Institute

Recommendations of the Viva Voce Board

As members of the Viva Voce Board, we certify that we have read the dissertation prepared by Shri Prasun Sharma Chowdhury entitled "Characterization of Microstructure of Nuclear Structural Materials by XRD" and recommend that it may be accepted as fulfilling the dissertation requirement for the Degree of Doctor of Philosophy.

D. K. Srivastava — Date: 23/4/12

Chairman- Dr. D. K. Srivastava, VECC

P. Barat — Date: 23/04/2012

Guide/Convener- Dr. P. Barat, VECC

A Chakrabarti — Date: 23.04.2012

Member- Dr. Alok Chakrabarti, VECC

Date:

Member- Shri N. Saibaba, NFC

D. Srivastava — Date: 23.04.2012

Member- Dr. D. Srivastava, BARC

M. Vijayalakshmi 23.4.12 — Date: 23.4.12

Examiner- Dr. M. Vijayalakshmi, IGCAR

Final approval and acceptance of this dissertation is contingent upon the candidate's submission of the final copies of the dissertation to HBNI.

I hereby certify that I have read this dissertation prepared under my direction and recommend that it may be accepted as fulfilling the dissertation requirement.

Date: 23/04/2012

Place: VECC, Kolkata.

P. Barat

RECOMMENDATION OF THE VIVA VOCE EXAMINER COMMITTEE

23.04.2012

Reports of the examiners, Professor K. Linga Murty, Director of Graduate Programs, Nuclear Engineering, North Carolina State University, USA and Professor M. Vijayalakshmi, Associate Director, Physical Metallurgy Group, IGCAR, for the thesis entitled "Characterization of Microstructure of Nuclear Structural Materials by XRD" of the student **Sri PRASUN SHARMA CHOWDHURY (PHYS – 04200604001)** are satisfactory. Both the examiners have recommended for the award of the Ph.D degree to Sri PRASUN SHARMA CHOWDHURY after examining his thesis. However, some questions were raised by them and it was also suggested that Sri PRASUN SHARMA CHOWDHURY has to answers those questions in the open seminar. In this context the Viva Voce examination in the form of an open seminar has been arranged on 23rd of April, 2012 in VECC. A notice in this regard has been circulated in the VECC and SINP notice boards. In this seminar Sri PRASUN SHARMA CHOWDHURY answered all the questions raised satisfactorily. It is being felt that the answers to the questions raised by the examiners need not be incorporated in the thesis. The Viva Voce examiner committee recommends that **Sri PRASUN SHARMA CHOWDHURY (PHYS – 04200604001)** can now be awarded Ph.D. degree in Physical Sciences.

D. K. Srivastava

1. **Professor D.K. Srivastava, Associate Director (Physics), VECC – Charman**

2. **Sri N. Saibaba, Chief Executive, NFC, Hyderabad- Member**

3. **Professor Alok Chakrabarti, Associate Director (Accelerators), VECC – Member**

4. **Professor Dinesh Srivastava, Head, Physical Metallurgy Section, BARC – Member**

P. Barat 23/04/2012

5. **Professor P. Barat, Head Material Science Section, VECC – Convener**

M. Vijayalakshmi 23.4.12

6. **Professor M. Vijayalakshmi, Associate Director, Physical Metallurgy Group, IGCAR is the Viva- Voce Examiner.**

RE: DATE OF THE VIVA-VOICE EXAMINATION OF SRI PRASUN SARMA CHOWDHURY

CE's Office — Saturday, April 21, 2012 11:57AM

From: "CE's Office" <cenfc@nfc.gov.in> — Saturday, April 21, 2012 11:57AM

To: <pbarat@vecc.gov.in> — Hide Details

Cc:

Bcc:

Sent by: "CE's Office" <cenfc@nfc.gov.in>

Dear Dr. Barat,

Please refer to your e-mail dated April 16, 2012 on the subject matter. I regret to inform you that, due to pre-occupation, I will not be able to attend the Viva – Voice examination of Shri Prasun Sharma Chowdhury on April 23, 2012 at VECC.

Regards,

N. Saibaba
Chief Executive, NFC

From: pbarat@vecc.gov.in [mailto:pbarat@vecc.gov.in]
Sent: 16 April 2012 15:30
To: dinesh@vecc.gov.in; nsai@nfc.gov.in; cenfc@nfc.gov.in; mvl@igcar.gov.in; alok@vecc.gov.in; dsrivas@barc.gov.in; pbarat@vecc.gov.in
Subject: DATE OF THE VIVA-VOICE EXAMINATION OF SRI PRASUN SARMA CHOWDHURY

Dear All,

The viva – voice examination in the form of an open seminar of Sri PRASUN SHARMA CHOWDHURY has been arranged on 23rd of April at 11.30 AM in the Room No. 202, the Physics Conference Room. Sri PRASUN SHARMA CHOWDHURY has to defend his thesis entitled "Characterization of Microstructure of Nuclear Structural Materials by XRD". Kindly send your travel plans so that necessary arrangements can be made.

With regards,

P. Barat

attested.

P. Barat
23/04/2012

Dr. P. Barat
Head, Material Science Section
& Dean-Academic (VECC), Physical Sciences.
Government of India
VEC Centre
AF, Bidhan Nagar, Kolkata-700 064

STATEMENT BY AUTHOR

This dissertation has been submitted in partial fulfillment of requirements for an advanced degree at Homi Bhabha National Institute (HBNI) and is deposited in the Library to be made available to borrowers under rules of the HBNI.

Brief quotations from this dissertation are allowable without special permission, provided that accurate acknowledgement of source is made. Requests for permission for extended quotation from or reproduction of this manuscript in whole or in part may be granted by the Competent Authority of HBNI when in his or her judgment the proposed use of the material is in the interests of scholarship. In all other instances, however, permission must be obtained from the author.

Prasun Sharma Chowdhury

Prasun Sharma Chowdhury

DECLARATION

I, hereby declare that the investigation presented in the thesis has been carried out by me. The work is original and has not been submitted earlier as a whole or in part for a degree / diploma at this or any other Institution / University.

Prasun Sharma Chowdhury

Prasun Sharma Chowdhury

Dedicated to:

The source of

my inspirations...

Acknowledgements

First of all, I gratefully want to acknowledge the constant academic and personal support received from my supervisor Dr. P. Barat. I am very much thankful to him for his clear and effective discussions which helped me in finding the platform of research in the field of Materials Science.

I am very happy to convey my gratitude to my senior collaborators Dr. Paramita Mukherjee and Dr. N. Gayathri Bannerjee for their constant encouragement and support starting from the initial stages of my research career. I am really very very grateful to them for their constant effort for motivating me to be in Physics, and inspiring me at all the ups and downs in my research career. I also would like to convey my thanks to Dr. Mishreyee Bhattacharya for her helpful collaboration. I also want to acknowledge Shri Sanjoy Majumdar for his kind help during the experiments performed by me in VECC. I also acknowledge Shri Tapas Mallik for his kind help during the preparation of the flange and the samples in the VECC workshop. Beside these, I want to gratefully acknowledge Apu Da (Dr. Apu Sarkar) for his helpful suggestions and advices during different necessary moments of my research life. I also acknowledge Prof. P. M. G. Nambissan, SINP for his helpful collaboration.

I am very happy to take the opportunity to acknowledge Dr. Dinesh Kumar Srivastava (Head, Physics Group, VECC) for his valuable suggestions which helped me a lot to continue my research career in Physics.

Beside all these, I want to acknowledge all of my senior and junior research fellows in VECC (Victor, Hari, Santosh, Amal, Amlan, Sabyasachi, Mriganka Da, Sidharth Da, Saikat Da, Atanu Da and many others) for their memorable presence at different necessary times during my research life in VECC.

I am very grateful for taking this opportunity to acknowledge Dr. R. K. Bhandari, Director, VECC for his kind support which helped me a lot to continue my research work in VECC.

It is my pleasure to take this opportunity to acknowledge my parents for believing in me, for their patience, and for their continuous support which helped me a lot in continuing my research career.

Last but not the least, I want to take this opportunity to acknowledge all of my well wishers who inspired me in the every aspects of my life, and have been the support for me during all the necessary times.

Prasun Sharma Chowdhury

Synopsis

The zirconium based alloys and stainless steels are very important core structural materials in nuclear reactors. These alloys show very good performance in the mechanical properties at elevated temperatures and sustain the structural integrity of the nuclear reactor under the severe operating conditions. The important zirconium based alloys are the Zircaloy-2, Zr-2.5Nb, Zr-1Nb and Zirlo. Among them, Zircaloy-2 is used as the cladding material and Zr-2.5Nb is used as the pressure tube material in the Pressurized Heavy Water Reactor (PHWR). The binary alloy Zr-1Nb and the quaternary alloy Zirlo (Zr-1Nb-1Sn-0.1Fe) are also the candidate materials for the use as clad materials in PHWR. On the other hand, the stainless steels like SS316L and D9 alloy are the important core structural materials for Fast Breeder Reactor (FBR). The pre-irradiation microstructure of these materials plays significant role in controlling their structural integrity during the operation of the reactors. Hence it is of great interest to study the microstructure of these alloys under deformed and irradiated conditions.

There are various well known techniques to study the microstructure of the polycrystalline materials like optical microscopy, X-ray diffraction technique, electron microscopy etc. Out of all these techniques, only the X-ray diffraction technique provides statistically averaged information about the microstructure of the materials over a large volume of the sample ($\approx 10^9$ μm^3), whereas the other techniques provide localized information about the microstructure of the materials.

In the present thesis, the microstructure of different zirconium and stainless steel based reactor core structural materials have been characterized using X-ray Diffraction Line Profile Analysis (XRDLPA). The studies have been performed under the deformed and irradiated conditions of the materials. The post-irradiation microstructural changes of the Zr-1Nb alloy have been characterized using XRDLPA. Positron Annihilation Spectroscopy (PAS) has been used to characterize the nature of the point defects created during irradiation of Zr-1Nb alloy and their role in controlling the irradiated microstructure. Anomalous variation was observed in the microstructural parameters at some specific dose of irradiated Zr-1Nb alloy. This observation elucidates the fact that the irradiated microstructure is very much sensitive to dose and dose rate in the low dose regime.

Study of the deformed microstructure reported in this thesis can be classified into two different parts. In the first part, heavily deformed powders of different zirconium based alloys (Zircaloy-2, Zr-2.5Nb and Zirlo) have been obtained with the help of finely threaded jewelery files. The microstructures of these heavily deformed alloys have been characterized using the different model based techniques of XRDLPA. These different models of XRDLPA were found to be complementary to each other in characterizing the microstructure of the material. The studies show that, the pres-

ence of Nb enriched β-phase in α-Zr matrix in Zr-2.5Nb and Zirlo was responsible in controlling the domain growth, resulting in a smaller domain size compared to that of Zircaloy-2.

In the second part, the in-situ microstructural evolution of heavily deformed D9 alloy powders has been studied during the early stages of annealing, both with time and temperature. In this study, the evolution of the lowest length scale dislocation substructure at the earliest stages of annealing has been studied for the first time using XRDLPA. The growth of these lowest length scale substructures during the early stages of annealing have been modeled successfully from the light of the rearrangement and annihilation of dislocations.

Microstructural change of different nuclear structural materials during their irradiation, deformation and annealing, has been successfully studied using the different model based techniques of XRDLPA.

In the present thesis, Chapter 1 consists of a general introduction along with the scope of the thesis. The details of the experiments performed and the methods of analysis have been described in Chapter 2. Chapter 3 of the thesis is based on the post irradiated microstructural characterization of Zr-1Nb alloy. The study of microstructures of different zirconium based alloys under their heavily deformed condition has been discussed in Chapter 4. In Chapter 5, the in-situ study of microstructural evolution of heavily deformed D9 alloy powders has been discussed in detail. The overall conclusion on the studies performed in the present thesis is given in Chapter 6.

List of Figures

List of Tables

Contents

Chapter 1

Introduction

After the revolutionary invention of X-ray by Röntgen (November 8th, 1895), a large number of experiments were launched by different eminent scientists to find out the nature of this radiation and its interactions with matters. In 1914, M. Laue received the Nobel Prize for Physics for his discovery of X-ray diffraction by crystals. After that, besides the vast usefulness of the X-ray diffraction (XRD) technique to study the structure of crystalline materials, the technique also attracted utmost interest as a unique characterization tool to extract the microstructural features of polycrystalline materials [1, 2, 3]. These microstructural features play important roles in controlling different physical and mechanical properties of the materials, and hence their studies have gained vital importance in the field of materials science. Extensive early works about the microstructural characterization of these materials have been reviewed by Greenaugh [1], Warren [2] and De and Sengupta [3].

1.1 Microstructure of polycrystalline materials

Unlike the ideal crystal, the real crystal deviates from its perfect periodicity in a number of different ways. This deviation from the regular array of atoms in a crystal is termed as defects or imperfections. Depending on the sizes and dimensions of the defects present in the materials, they are termed as

point, line, surface and volume defects. If the deviation of the periodicity is localized within a few atoms, then it is termed as point defect or point imperfection. However, for the other three types of defects, the deviation extends over a wide range of the crystal, and these are termed as lattice imperfections.

The common point defects in the crystal are vacancies, vacancy clusters, interstitials and the presence of extra atoms not in regular positions. These point defects can be produced inside the crystal due to the thermal fluctuation and thus definite atomic concentrations of these point defects can exist in thermal equilibrium. The atomic concentration of these thermally activated point defects can be represented by a simple Boltzmann expression [4, 5]:

$$c = \exp(-\frac{H_f}{kT}) \tag{1.1}$$

where H_f is the formation enthalpy of that specific point defect. Since in case of solids, $H_f = E_f$, where E_f is the formation energy of that specific point defect, equation 1.1 can be wtitten as:

$$c = \exp(-\frac{E_f}{kT}) \tag{1.2}$$

This thermal vacancy concentration increases rapidly with increase in temperature. Thus, by rapid quenching of the material from a temperature closed to its melting point, these vacancies can be trapped as excess vacancies in room temperature [6]. However, a huge amount of excess vacancies can also be introduced in the material by extensive plastic deformation [7] or by ion irradiation [8].

The observed low values of critical shear stress of the materials can be explained by the motion of a line imperfection (dislocation) through the matrix of the atoms. This idea was proposed independently by Taylor [9], Orowan [10], and Polanyi [11]. In fact, dislocation is the most important line defect in crystal which is responsible for the plastic deformation, through the process of the slip. There are two main types of dislocations: edge and screw dislocations. In case of edge dislocations the slip occurs in a direction perpendicular to the dislocation line, whereas in case of screw dislocation,

this direction is parallel. However, the dislocations present in the real materials are of mixed types, i.e. they have both the edge and screw components. The stress field present around a dislocation [12] causes them to interact with the existing defects inside the crystals. Dislocations move across the crystal due to their mutual interactions as well as due to the influence of external conditions (e.g. mechanical stress, temperature gradient etc.). The mechanical properties of a material is primarily governed by the ability of movement of dislocations through the periodically arranged atoms.

Materials used frequently in different industries and other purposes are generally polycrystalline in nature, i.e. they are made of small crystallites or grains with each of them having specific crystallographic orientation. The boundary between the grains in a polycrystalline aggregate is called *grain boundary* which is an important example of surface defect present in polycrystalline materials. The grain boundaries are the regions of disturbed lattice having widths equal to a few atomic diameter, and contains the *grain boundary dislocations*. The order of the grain boundary is determined by the orientation difference of the grains on each side of the boundary. In case of *low angle grain boundaries*, this orientation difference can vary from a few minutes of a arc to a maximum of a few degrees. On the contrary, for *high angle grain boundaries*, this orientation difference is quite large. These high angle grain boundaries are the regions of high surface energy and hence they act as preferential sites for different solid state reactions like diffusion, phase transformation, precipitation reactions etc [6]. Beside the grain structure of polycrystalline materials, each grain also can contain a definite substructure network. The small crystallites within a grain, which construct the substructure network, are called *subgrains* and are bounded by *subgrain boundaries* which are the low angle boundaries, and thus contains less surface energy.

Apart from the existence of grain boundaries, the lineage and antiphase boundaries are also observed as surface defects in polycrystalline materials. On the other hand, voids may be formed inside polycrystalline materials due to the clustering of vacancy type defects. These voids are the examples of volume defects observed in the material. However, the presence of second phase particles as precipitates in the host atom matrix are also the examples of volume defects.

On the basis of the above discussion, the *microstructure* of a polycrystalline materials can be explained as the structure of the material in a micron or submicron range, consisting of different *microstructural features* like grains, subgrains, grain boundaries, presence of second phase particles etc. The length scale of different microstructural features can vary from nanometers to millimeters, depending on their types.

1.2 Effect of microstructure on the properties of polycrystalline materials

The properties of a polycrystalline material can be classified into two parts, one is the intrinsic and independent of microstructure, and the other is sensitive to microstructure. The former one mainly depends on the chemistry, atomic bonding and electronic configuration of atoms for that specific materials. Some typical intrinsic properties of a material are the elastic constants, melting point, specific heat, density and coefficient of thermal expansion. On the other hand, the later part is significantly controlled by the size, shape, distribution and orientation of the different microstructural features. Especially the different mechanical properties of the metals and alloys, e.g. the yield stress, ultimate tensile strength and the creep strength are very much sensitive to their microstructural features [13, 14, 15, 16, 17]. The values of these microstructural parameters can be affected significantly by means of extensive deformation or by irradiation, which in turn causes the change in the mechanical properties of those materials. Numerous studies are there which proved the significant change in the mechanical properties of different materials due to irradiation [18, 19, 20] and deformation [21, 22]. The electrical conductivity of metals is also a microstructural sensitive property [23, 24, 25]. Since the lattice defects act as obstacles for the transport of electrons through a metal lattice, this causes a significant change in the electrical conductivity of that material.

1.3 Microstructural changes due to plastic deformation

Under the application of external stress, the deformation of polycrystalline materials takes place mostly by the process of *slip*, which involves the movement of dislocation through the crystal [6, 12].The process of slip takes place most easily on certain crystallographic planes and along certain specific crystallographic directions, depending on the type of the crystal structure. In general, the *slip planes* are the highest atom density planes in the crystal and the *slip directions* are the closest packed directions lying on the slip planes. A slip plane together with the corresponding slip direction defines a *slip system* for a specific type of crystal structure. For example, in case of FCC structure, the highest atom density planes are the $\{111\}$ planes and the closest packed directions are the $\langle 110 \rangle$ directions, which give rise to 12 slip systems for this crystal structure. Since the motion of dislocations is preferred on the slip planes along the slip directions, the slip systems play a significant role in controlling the microstructure of the polycrystalline materials [26, 27].

Twining is another important process which takes place during the deformation of most metals and metallic alloys [6, 28, 29, 30, 31, 32]. In this process, a part of the crystal gets twisted in such a fashion that the twisted part is oriented as a mirror image of the parent crystal. The plane of symmetry between the parent crystal and the twisted region is called as *twin plane*. Twins may be formed during mechanical deformation of metals (*mechanical twin*) or during the annealing of a plastically deformed metal (*annealing twin*). Similar to the process of slip, twining also occurs on certain crystallographic planes and along certain crystallographic directions, depending on the crystal structure of that material. However, for the metals possessing many slip systems, twining does not take place as a dominant deformation process.

During deformation of polycrystalline materials, the most part of the supplied energy is dissipated in the form of heat. However, a very small amount of the supplied energy ($\approx 1\%$) is stored inside the material in the form of crystal defects, mostly point defects and dislocations. Many works have been performed on the stored energy of deformed metals and have been reviewed by Bever *et al.*

[33]. Since the mobility of the point defects is very high, they give a very less amount of contribution to the stored energy unless the deformation is performed at sufficient low temperature [7]. Hence it is the dislocation created during the plastic deformation which plays a significant role behind the formation of the deformed microstructure at ambient and higher temperatures. The microstructural changes during the deformation of polycrystalline materials involve the change in different microstructural features like grain shape, size and orientation; causing an increase in the total grain boundary area [34]. This excess amount of grain boundary area is formed due to the accumulation of newly created dislocations during deformation. Moreover, the accumulation of these dislocations also causes the formation of substructure network inside the grains, which is a very important feature of the deformed microstructure. Studies on the development of substructure in polycrystalline materials deformed under moderate strains have been started in the years of 1960 [35, 36, 37, 38] using Transmission Electron Microscopy (TEM). However around 1965, after the work by Embury *et al.* [39], the studies on the substructure developed at high strain have gained a huge interest. The recent studies in this area include Hughes and Hansen [40], Hansen and Juul Jensen [41] and Hughes [42].

The stacking fault energy (SFE) of a material also plays a significant role in controlling its substructure. In case of the metals with moderate or high SFE, the dislocations form cell structure [7]. However, presence of alloying elements as solute in the host atom matrix can prevent the formation of this cell structure. It has been observed that the addition of 3-5% Mg as solute element in the Al matrix can hinder its dynamic recovery as well as prevents the dislocations to form the cell structure [43, 44, 45, 46]. On the other hand, for the low SFE metals, the cell structure is not observed generally.

In addition to all these abovementioned microstructural changes, the orientations of individual grains also change with increasing degree of deformation. Since the deformation occurs predominantly on the most favorably oriented slip or twinned system, this orientation change is not random, rather it gives rise to a *preferred orientation* along certain crystallographic direction. The preferred orientation developed due to deformation of polycrystalline materials is generally termed as *deformation texture* [47, 48].

1.4 Microstructural changes due to ion irradiation

When a polycrystalline material is irradiated with energetic charged particles, a huge amount of energy is transferred into the material. Depending on the energy of the incident projectile, it's mass and charge state, the projectile first looses its energy into the target through the process of electronic excitation and then it interacts with the atoms of the target material, resulting in the production of *Primary Knock-on Atom* (PKA) [8, 49]. The passage of these PKAs through the target atom matrix causes the creation of additional knock-on atoms and this process goes on till the the energies of the knock on atoms become less than the *atomic displacement energy* of that target material. By this process, the PKAs create a distribution of point defects inside the target material, which is termed as *displacement cascade*. During irradiation, this entire series of processes take place within a very small duration of time ($\approx 10^{-11}$ s) [50].

The defects which are produced during irradiation, interact with themselves and also with the existing microstructure through the process of long range diffusion. During irradiation, due to the high concentration of the point defects in the target material, the rate of diffusion of these defects also gets affected significantly. The work performed by R. Sizmann [51] revealed that the *radiation enhanced diffusion* causes not only an enhancement of the usual diffusion path, but also opens new channels for defect reactions which is not observed in the normal thermally activated diffusion. Clustering of point defects is a very important process which takes place during irradiation. There is an extensive review by Eyer [52] which explains the ways of formation of small point defect clusters and their effect on the properties of the irradiated metals. These clusters can again collapse into the dislocation loops [53, 54, 55], resulting in an increase in the dislocation density of the irradiated material. In addition to this, some of the vacancies created during irradiation may interact with the impurity elements present in the target atom matrix, giving rise to the formation of vacancy-impurity complexes.

The extensive microstructural changes caused by the irradiation results in the dimensional changes of the materials as well as significant changes in their mechanical, physical and corrosion

properties [56, 57, 58]. There are a considerable amount of studies [59, 60] which have been carried out to understand the effect of ion irradiation on the microstructural changes in different nuclear structural materials. It was found that the type of ions, alloying elements and impurity variations significantly controls the nature of radiation damage in these materials [61]. There are also extensive works based on the proton, neutron and electron irradiation of pure Zr and Zircaloys [62, 63, 64, 65]. More studies on the microstructural changes due to irradiation have been reviewed by Stiegler and Mansur [66], Kiritani [67] and Vladimirov and Bouffard [68].

1.5 Microstructural changes due to annealing

The deformation or irradiation of solid polycrystalline materials causes introduction of high concentration of defects which exists in non equilibrium condition. Under the application of external thermal energy, these defects become mobile and interact with themselves and the existing microstructure. This process results in the removal of some of the defects and others to alternatively arrange to a lower energy configuration. Consequently, the different microstructure sensitive properties of the materials changes during the annealing. In 1829, Savart [69] showed that the cast ingots of various metals shows acoustic anisotropy, which changes due to plastic deformation and also due to subsequent annealing. This observation was the first evidence of the microstructural change of the materials during annealing. However, in the early times, it was believed that the plastic deformation causes the amorphisation of the metals, which can be recovered back by subsequent annealing treatment. During that period, this process was known as *crystallization* [70, 71]. In 1887, Sorby [72] introduced the metallographic technique and observed the elongated grain structures in cold worked iron and defined this structure as the *state of unstable equilibrium* which came into the stable condition through the production of new equiaxed grain structure due to subsequent heat treatment. Sorby termed this process of change in microstructure during heat treatment, as *recrystallization*.

The microstructural evolution during annealing of the solid polycrystalline materials usually consists three different stages: recovery, recrystallization and grain growth [7, 73]. Among these three processes, recovery is the most initial process of the annealing. During recovery, the dislocations get annealed out partially and the rest rearranges among themselves to attain a lower energy configuration. Since the dislocation structure is not completely removed during recovery, this process involves only a partial restoration of properties [7]. With further increase of annealing temperature, the *recrystallization* process starts where the new dislocation free grains are formed inside the materials. The growth of these newly formed grains and the consumption of the old grains then take place simultaneously, which results in a new arrangement of grains with a low dislocation density, causing a further restoration of the properties of the materials. The recrystallization process is followed by a third process called the *grain growth*. The process of grain growth was not clearly distinguished until the work done by Carpenter and Elam [74] and Altherthum [75], which revealed that the stored energy during cold work is the driving force for recrystallization, while the grain growth process is driven by the energy of the grain boundaries. During grain growth, the larger grains grow in order to minimize the total grain boundary energy. The smaller grains are generally eliminated during the grain growth process. Sometimes, the grain growth process leads to the selective growth of some larger grains, which is termed as the *abnormal grain growth*.

The initiation and rate of the different annealing processes significantly depend on the annealing temperature, type of the material and the degree of deformation it experiences prior to the annealing process. In the year of 1900, Ewing and Rosenhain [76] noted that the recrystallization temperature of a solid polycrystalline material has a strong dependance to its melting point. After that in 1902, Humfrey [77] showed that the rate of recrystallization increases with the increase of annealing temperature. The rate of recovery process is also strongly influenced by the melting temperature of the materials. Beside these, the stacking fault energy of the material also significantly controls the rate of the recovery mechanism [7]. For the materials with higher stacking fault energy (e.g Aluminium), the dislocation climb process is easier which causes the significant amount of re-

covery prior to recrystallization [78]. On the contrary, for the materials with low stacking fault energy (e.g. Copper), the climb process becomes difficult and hence a small extent of recovery takes place prior to recrystallization [7]. Even the presence of alloying elements in the host atom matrix may reduce it's stacking fault energy and thus inhibiting the recovery process. For example, presence of small amount of Mg in Al matrix, or the presence of a little amount of Mn as alloying element in iron, may restrict their recovery process by a significant amount [79, 80, 81].

The amount of plastic deformation the material experienced prior to the heat treatment, is also an important parameter which controls the extent of the recovery and its rate. It has been observed that the amount of recovery of a plastically deformed material at a constant temperature generally increases with strain [81]. However, for the heavily deformed polycrystalline materials, the similar observation may show the opposite trend [7]. The work by Masing and Raffelsieper [82] and Michalak and Paxton [83] revealed that for polycrystalline materials, a complete recovery prior to the recrystallization process can only take place if the material is lightly deformed. However, for single crystals, there are many reported works where complete recovery has been observed even after a considerable amount of plastic deformation [83, 84, 85].

1.6 Techniques of microstructural characterization

There are different techniques to study the microstructure of the polycrystalline materials. In general, the microstructural characterization is performed by using specific types of probes which interact with the material and give necessary signal carrying information about the microstructure. These probes may be the visible light, X-ray or the energetic electron beam. Depending upon the types of probes, these characterization techniques are known as the optical microscopy, X-ray diffraction technique and electron microscopy. However, the energetic positrons can also be used as the probe to get the microstructural information. This technique is called the Positron Annihilation Spectroscopy (PAS).

Depending upon the type of the information obtained, these techniques can be classified as direct and indirect techniques.

The direct techniques of microstructural characterization of solid polycrystalline materials involve the optical and the electron microscopy techniques. In these techniques, the direct images of the microstructure (*micrographs*) are captured and then analyzed to acquire the required information. Since the grain sizes of the polycrystalline materials are generally in the micron range, they can be clearly visible in a optical micrograph. However, the optical microscopy can not be used to extract the information about the dislocation substructure since the length scale of this substructure is very much less than the wavelength of the visible light. On the contrary, the wavelength of the electron used in the electron microscopy technique is comparable even up to the atomic spacing of the general polycrystalline materials, and hence the these techniques are the very much powerful to study the dislocation substructure in a localized region. The Scanning Electron Microscopy (SEM) and the Transmission Electron Microscopy (TEM) belongs to this category.

The most important and reliable indirect technique for characterizing the microstructure is the X-ray diffraction technique. Since the wavelength of X-ray is comparable with the lattice spacing of the materials, it can be used as a very reliable probe to extract the microstructural information. In fact, the X-ray diffraction technique is very much useful to extract the statistically averaged information of the microstructure of the materials in a non destructive way, and this statistically average information is very much relevant with different microstructure dependant properties of the materials. Specifically for the materials with very high dislocation density, the X-ray diffraction technique becomes an unique characterization tool to extract the microstructural information since the regions of high dislocation density is very much difficult to see by TEM. However, the X-ray diffraction technique is not useful to get the information about the point defects existing inside the materials. In this context, PAS is a very useful technique which can characterize the nature and concentration of the vacancy or vacancy clusters inside the materials. However, it is difficult to characterize the interstitial type de-

fects using PAS as the positron is very much insensitive to detect those type of defects. The resistivity method is also a useful indirect method to extract the information about the point defects.

1.7 Characterization of microstructure by X-ray diffraction technique

From the last few decades, the study of microstructure of polycrystalline materials by X-ray diffraction technique has become a great subject of interest. Beside the studies of crystal structure by X-ray diffraction technique, the studies of microstructure also gained utmost interest when Scherrer [86] pointed out that the finite sizes of the small crystallites inside the polycrystalline materials cause broadening in the X-ray diffraction peak. In 1944, the theory of line broadening was formulated by Stokes and Wilson [87] in a more exact and complex manner, where they incorporated the lattice strain as an important broadening parameter. Later, based on the formalisms of Wilson [88] and Stokes and Willson [87], Warren and Averbach [89, 90] developed a more general theory of X-ray line broadening of cold worked metals. In his theory, Warren proposed that the dislocation arrays in the cold work material form the substructure inside the grain. These substructure consists of coherently diffracting domains which is responsible for the XRD line broadening corresponding to the domain size [91]. In 1959, based on the works of Barret [92] and Paterson [93], this theory was further extended by Warren [94] to incorporate the effect of stacking fault on the X-ray line shape. However in 1967, after the development of Rietveld Refinement [95], the microstructural study using X-ray diffraction line profile analysis (XRDLPA) has took an effective step. The studies of the present thesis is mainly based on the microstructural analysis using X-ray diffraction technique. A detailed review of the extensive works in this field will be discussed in the upcoming chapters.

1.8 Zirconium and Stainless steel based alloys as core structural materials in nuclear technology

The works reported in the present thesis has been performed on different zirconium and stainless steel based alloys which are very important core structural materials used in the nuclear industry. There are different types of zirconium based alloys (e.g. Zircaloy-2, Zircaly-4, Zr-2.5Nb, Zirlo etc.) which are extensively used as core structural materials in Pressurized Heavy Water Reactors (PHWR). On the other hand, in case of the First Breeder Reactors (FBR), the stainless steel based alloys (e.g. SS316L, alloy D9 etc.) are used as the core structural materials. During operation of the reactors, these materials experience severe operating condition like extensive irradiation environment, which causes the degradation of their mechanical properties. Hence to achieve high burn up, these materials should be sustainable enough to that extreme operating condition. Extensive research is going on to develop different types of new alloys which can be used successfully as core structural materials in the nuclear reactors. However, since the mechanical properties of these materials are strongly dependant on their microstructure, the study of microstructure of these materials under deformed and irradiated condition has become the subject of utmost interest.

Zirconium based alloys are very important materials in the field of nuclear technology since they are extensively used as core structural materials in PHWR. This alloys have low thermal neutron absorption cross section, excellent corrosion resistance against the high temperature aqueous environment, better mechanical properties at elevated temperatures and better irradiation creep and growth resistance properties. Hence these alloys are sustainable under the severe operating condition of PHWR. However, to achieve higher burn up, a continuous research always persists their to develop new kind of alloys which are best suitable for the reactors. It has been observed that, if a small amount of niobium is added in the zirconium as alloying elements, the mechanical properties of the alloy enhances considerably. Beside this, after addition of Nb, the alloy also possesses considerably better

corrosion resistance and better irradiation and growth resistance properties. Hence the Zr-Nb alloys are very much sustainable to higher burn up of fuels and they have got immense interest as candidate materials of PHWR.

There are several important properties of Zirconium based alloys which made them unique as core structural materials of PHWR. The most important property is it's low thermal neutron absorption cross section which made this alloys best suitable for better neutron economy. At room temperature, these alloys exhibit α-phase which has HCP crystal structure with a c/a ratio less than the ideal value. This makes the $(10\bar{1}0)$ plane most predominant for the dislocation movements. This preferable movement of dislocations along some specific crystallographic directions results in the anisotropy in different microstructural features of these alloys during the thermo-mechanical treatments. This also causes the development of strong crystallographic textures during the fabrication of different core structural part of PHWR. The zirconium based alloys show allotropic change from HCP (α) to a BCC (β) structure at high temperature [96]. However, addition of a small amount of Nb causes the existence of finely dispersed β-phases in the α-matrix which enhances the mechanical properties of these alloys.

The zirconium based alloys developed for use in PHWR as core structural materials, can be broadly categorized into two series: the Zr-Sn and Zr-Nb series [97]. Zircaloy-2 (Zr-1.5Sn-0.1Fe-0.1Cr-0.1Ni) and Zircaloy-4 (Zr-1.5Sn-0.2Fe-0.1Cr) are the important alloys in the Zr-Sn series. The important alloys in the Zr-Nb series are Zr-1Nb, Zr-2.5Nb, Zr-2.5Nb-0.5Cu and M5 (Zr-1Nb-0.1O). The Zr-2.5Nb alloys is used as pressure tubes in PHWR where the Zircaloy-2 is used as the fuel clad materials. There are also developments in the new alloy series like Zr-Sn-Nb-Fe series, in which Zirlo (Zr-1Nb-1Sn-0.1Fe) and Alloy 635 (Zr-1.2Sn-1Nb-0.4Fe) are the important materials. The composition of different zirconium based alloys used for the present thesis is shown in table 1.1.

Unlike the PHWR, the Fast Breeder Reactors (FBR) operate at extensively high temperature (773-973K at the fuel clad) and the neutron flux also in this case is sufficiently high (10^{15} n/cm^2/s).

Table 1.1: Composition of different zirconium based alloys

Alloys	Sn (wt.%)	Fe (wt.%)	Cr (wt.%)	Ni (wt.%)	Nb (wt.%)	O (p.p.m.)	Zr (wt.%)
Zirlo	0.9-1.1	0.09-0.11	–	–	0.90-1.1	900-1300	rest
Zr-1Nb	–	–	–	–	0.90-1.1	900-1300	rest
Zr-2.5Nb	–	–	–	–	2.5-2.8	900-1300	rest
Zircaloy-2	1.2-1.7	0.07-0.2	0.05-0.15	0.03-0.08	–	1000-1400	rest

This high neutron flux in FBR causes the damage of the structural materials in two different mechanisms [97]. One is the creation of defects due to the radiation damage which is responsible for the irradiation hardening and embrittlement, irradiation creep and irradiation induced void swelling. The other mechanism is the (n,α) transmutation reaction which results in the helium embrittlement. Due to the higher operating temperature, the fuel clads experience extensive loads from the internal fission gas pressure and fuel clad interaction. The loads on the clad tubes also come from the temperature gradient and irradiation induced swelling gradient. Hence, in this case also, the core structural materials should be chosen in such a manner that they will be sustainable under this extensive operating conditions, allowing a high burn up of the fuels.

Several stainless steel based alloys have been developed for the use as core structural materials in FBR. The first generation clad and wrapper tube materials for FBR was the 304 and 316 grade stainless steels. However, to overcome the void swelling problem in the high irradiation environment, it became necessary to add different alloying elements as stabilizer, as well as to change in the chemical composition and modify the microstructure by the suitable series of thermo-mechanical processes. In india, for the Fast Breeder Test Reactor (FBTR), SS316L alloy have been chosen as the clad material. However, it is found [97] that the addition of the small amount of Ti, Si, P, Ni, B and C significantly increases the void swelling resistance properties of the stainless steel. The alloy D9 and D9I have been developed from this observation and they have shown satisfactory performance against the irradiation induced void swelling. The composition of the D9 alloy which has been used for the present thesis, is given below (table 1.2).

Table 1.2: Composition of the D9 alloy (in weight %)

Cr	Ni	Mo	Mn	Si	C	Ti	Nb	P	S	B	N	Co	Fe
13.5-14.5	14.5-15.5	2.0-2.5	1.65-2.35	0.5-0.75	0.035-0.0	0.25	0.05	0.02	0.01	10-20 p.p.m.	0.005	0.05	balance

1.9 Scope of the thesis

The zirconium and stainless steel based alloys are very important as core structural materials used in today's nuclear technology. These alloys show very good performance in the different mechanical properties at elevated temperatures and sustain the structural integrity of the reactor under the severe operating conditions. The important zirconium based alloys are the Zircaloy-2, Zr-2.5Nb, Zr-1Nb and Zirlo. Among them, Zircaloy-2 is used as cladding materials and Zr-2.5Nb is used as pressure tube materials is PHWR. The binary alloy Zr-1Nb and the quaternary alloy Zirlo (Zr-1Nb-1Sn-0.1Fe) are also the candidate materials for the use as clad materials in PHWR. On the other hand, the stainless steel based alloys (SS316L and D9 alloy) are the important core structural materials for FBR. The pre-irradiation microstructure of these materials play significant roles in controlling their structural integrity during the operation of the reactors. It has been reported that the initial microstructure, dislocation density and the domain size significantly controls the in reactor deformation and growth of zirconium alloys [98, 99, 100]. The irradiation induced void swelling of the stainless steel based alloys are also significantly controlled by the amount of prior deformation the materials experience before irradiation [101]. Hence it is of great interest to study the microstructure of these alloys under deformed and irradiated condition.

In the present thesis, the microstructure of different zirconium and stainless steel based reactor core structural materials have been characterized using XRDLPA. The studies have been performed under the deformed and irradiated conditions. The post-irradiation microstructural changes of the Zr-1Nb alloy have been characterized using XRDLPA. PAS has been used to characterize the nature of the point defects created during irradiation of Zr-1Nb alloy and their role in controlling the irradiated microstructure. Anomaly was found in the variation of irradiated microstructure at some specific

irradiation dose, which proves that the irradiated microstructure is very much dose and dose rate dependent in the low dose regime.

Study of the deformed microstructure reported in this thesis can be classified into two different parts. In the first part, heavily deformed powder of different zirconium based alloys (Zircaloy-2, Zr-2.5Nb and Zirlo) have been obtained with the help of finely threaded jewelery files. The powder materials coming out in this process experience extreme shear deformation and hence a huge amount of defects can be introduced in the materials by this process. The microstructure of these different zirconium based alloys then have been characterized using the different model based techniques of XRDLPA. The methods were found to be complementary to each other in characterizing the microstructure of the material. Beside this, the presence of Nb enriched β-phase in α-Zr matrix in Zr-2.5Nb and Zirlo was found to be responsible in controlling the domain grown, resulting in a smaller domain size compared to that of Zircaloy-2.

In the second part, the in-situ microstructural evolution of heavily deformed D9 alloys have been studied during the early stages of annealing, both with time and temperature. In this study, the evolution of the lowest length scale dislocation substructure at the earliest stages of annealing has been studied for the first time using XRDLPA. The growth of these lowest length scale substructures during the earliest stages of annealing have been modeled successfully from the light of the rearrangement and annihilation of dislocations.

Chapter 2

Experimental and Method of Analysis

2.1 Preparation of samples

2.1.1 Preparation of heavily deformed powder specimen

A large part of the present thesis is based on the study of microstructure of different reactor core structural materials under heavily deformed powder condition. The powder specimens were obtained from the core structural materials by careful hand filing with the help of finely threaded jwellery files.The powder particles obtained in this way experience extreme shear deformation and ensures high population of dislocations inside them. The details about the preparation of heavily deformed powder samples has been described under the experiemental section in Chapters 4 and 5.

2.1.2 Preparation of irradiated specimen

Irradiation of different Zr1Nb samples have been carried out with the Variable Energy Cyclotron at Kolkata, using 116 MeV O^{5+} ions. The target holder assembly used in the irradiation is shown in figure 2.1. Figure 2.2 shows the schematic diagram of the target holder assembly. This target holder

assembly consists of an aluminium flange over which the sample is mounted. The aluminium is used as the flange material because of its low nuclear reaction cross section for 116 MeV oxygen ion.

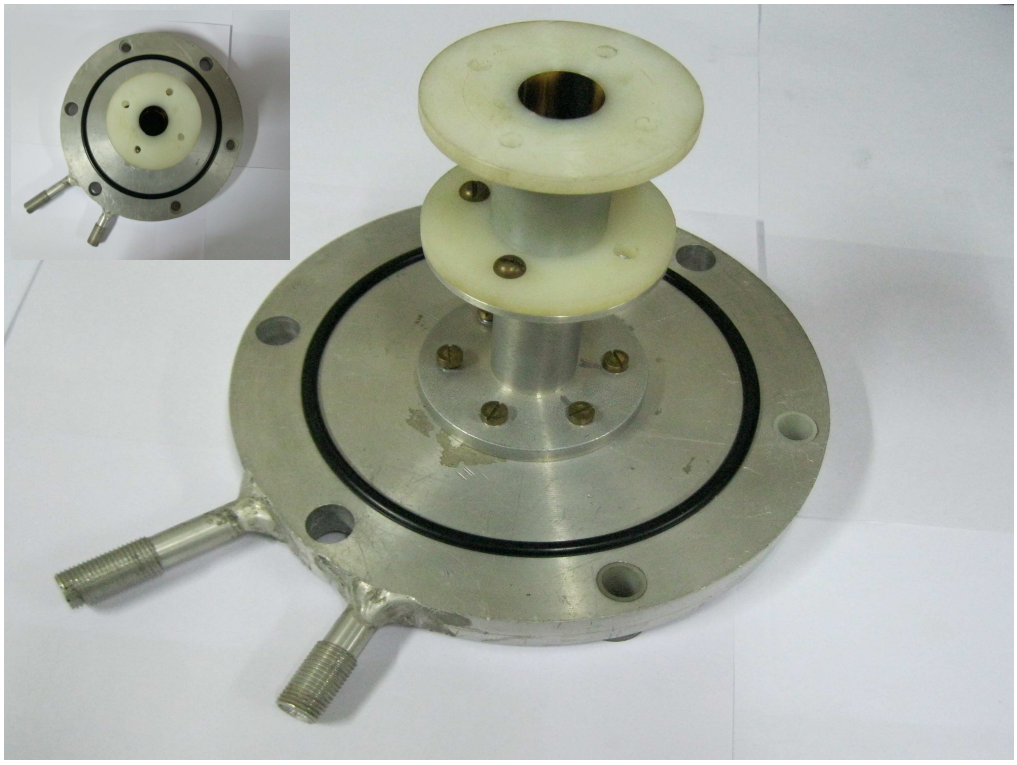

Figure 2.1: The target holder assembly used in the irradiation beamline: the top view of the flange is shown in the inset.

To ensure the proper focussing of the beam on the target, a 10 cm long collimator has been attached above the sample. This collimator consists of two different parts. The lower part of the collimator was made of conducting materials which ensures the proper suppression of the secondary electrons generated from the target during its irradiation. The upper part of the collimator was made of teflon so that the charge particles falling on the collimator wall does not contribute to the projectile particle count, giving an error to the measurement of irradiation dose.

The dose of irradiation on the samples was measured from the total amount of charge of the projectiles deposited on the target during its irradiation. As the samples used in the study are electrically conducting, the deposited charge have been collected directly from the back surface of the aluminium flange and measured with the help of a current integrator which was electrically connected

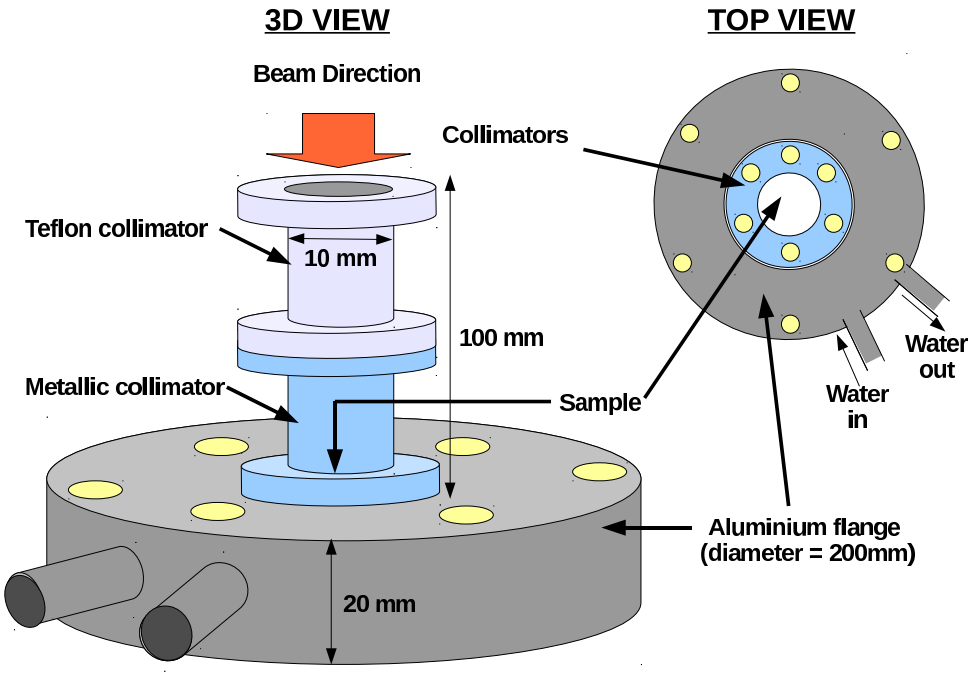

Figure 2.2: Schematic diagram of the target holder assembly

with the aluminium flange. The whole target holder assembly was kept insulated from the beamline by a perpex flange.

During irradiation a considerable amount of kinetic energy is deposited by the projectiles to the target material per unit time. A large amount of this deposited energy is liberated in the form of heat, resulting in a rise in the sample temperature. This increase in temperature during the irradiation of the samples affects the irradiated microstructure. Hence it is necessary to cool the sample. In our case, the sample was cooled by a continuous flow of water. The beam current was also maintained at 150 nA. Under these circumstances, the temperature of the sample did not rise above 313 K as measured by a thermocouple attached to the closest proximity of the sample. The rise of temperature of the sample upto 313 K was attained within 160 seconds at each case and then a constant temperature was maintained. The detailed information about the different irradiation doses and the dimension of the samples irradiated are given in Chapter 3. Microstructure of the irradiated samples were characterised by X-ray Diffraction Technique.

2.2 Collection of X-ray Diffraction Data

The X-ray Diffraction (XRD) data has been collected using the Bruker AXS D8 Advance Diffractometer (figure 2.3). The diffractometer works in $\theta - \theta$ Brag-Brentano geometry which is very useful for dealing with different types of samples (e.g. any block or sheet like sample, powdered samples or liquid samples) as the sample stage does not move in this case. Different types of X-ray sources (e.g.Cu, Co and Mo sources) can be attached with the source arm of this diffractometer. The detector arm consists of a Lynx-Eye^{TM} detector provided by Bruker AXS which gives a very high count rate. Two types of sample stages are there for this instrument. One is the conventional spinner stage (figure 2.4) for performing the room temperature XRD. The other one is an in-situ high temperature attachment from Anton Paar (figure 2.5).This high temperature attachment consists of a joule heated platinum strip as sample stage, along with a high vacuum chamber and a high temperature controller HTK 16 from Anton Paar. The high vacuum chamber for this the high temperature stage helps one to maintain the sample at high vacuum during the collection of the the high temperature XRD data. Details about the collection of the XRD data during the different types of studies have been discussed at the respective chapters.

2.3 Characterization of microstructure by X-ray Diffraction Line Profile Analysis (XRDLPA)

The deformation or irradiation of materials results in the change in their microstructure. These microstructural changes cause changes in the broadenings and the shape profiles of the XRD peaks. These shapes and broadenings of the XRD peak profiles take contribution fom two main causes, one is the contribution from the instrumental limitations, and another is the contribution from the microstructural imperfections like finite domain size and microstrain within the domain. Thus by

Figure 2.3: Bruker AXS D8 Advance Diffractometer.

Figure 2.4: Spinner stage for Bruker AXS D8 Advance Diffractometer

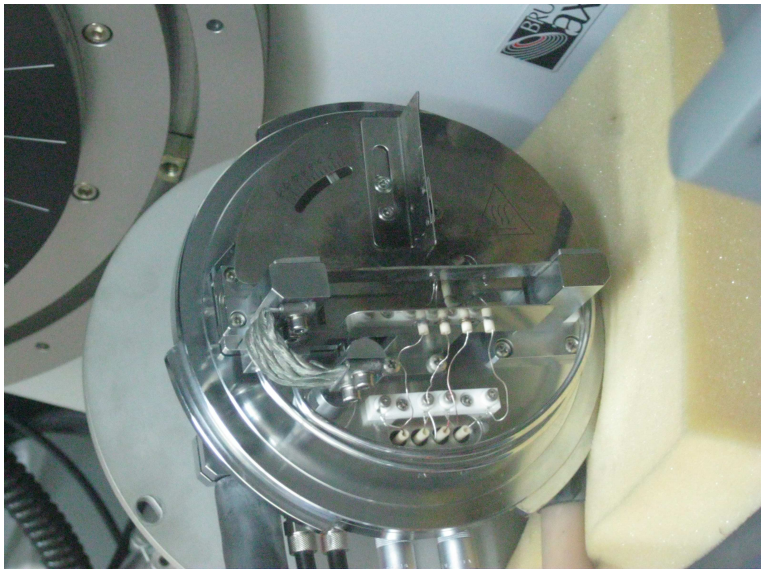

Figure 2.5: Anton Paar high temperature attachment HTK 16.

analysing the XRD data in some suitable manners, we can extract microstructural information when the broadening due to the instrumental limitations is eliminated. There are different model based techniques of XRDLPA which can be used to characterise the microstructure of the materials.

The integral breadths of the XRD peaks are the crucial parameters which carry the information about the broadening of the peaks. The integral breadth for an XRD peak profile is defined as the area under the peak divided by its maximum height. Hence for the XRD peaks, integral breadth takes the dimension of the diffraction angle ($\Delta 2\theta$) and can be treated as the broadening of the peak. However, unlike the FWHM, the integral breadth carries the information about the shape of the peak.

The domain size which is estimated as an important microstructural paramter during the XRDLPA, can be defined in two different ways. In one method, the domain size is estimated by averaging over the whole volume of the domain. The domain size estimated in this way is called the *volume weighted domain size*. However, there are also different methods where the the domains are projected on a certain crystallographic plane and then the domain size is estimated by taking the average over the area of the projection. The domain size estimated in this way is called the *surface weighted domain size*.

Since the information about the microstructural imperfections inside the materials is hidden in the shape of the XRD peak profiles, it is very important to choose a proper profile peak function so that the microstructural parameters can be extracted successfully by matching the experimentally observed XRD peak profiles with the assumed peak function. The different mathematical peak functions used frequently by different model based techniques of XRDLPA are as follow:

a) *Gaussian function*: A Gaussian function can be expressed as

$$G(x) = I_G(0)\exp(-\frac{ln2x^2}{w^2}) \tag{2.1}$$

where $I_G(0)$ is the peak intensity and w is the HWHM of the peak. Here $x = (2\theta - 2\theta_0)$, where θ is the diffraction angle and $2\theta_0$ is the peak position. For this function, the integral breadth can be written as $\beta = w\sqrt{\frac{\pi}{ln2}}$.

b) *Lorentzian function*: The Lorentzian function is also known as Cauchy function. It is expressed as

$$C(x) = I_C(0)\frac{1}{1+\frac{x^2}{w^2}} \tag{2.2}$$

here $I_C(0)$ is the peak intensity. The integral breadth for this function can be expressed as $\beta = w\pi$

c) *Voigt function*: A Voigt function is the convolution of a Gaussian and a Lorentzian function. it is expressed as

$$V(x) = I_V(0)\frac{\beta}{\beta_G}Re\{erf[\frac{x\sqrt{\pi}}{\beta_G} + ik]\} \tag{2.3}$$

here $I_V(0)$ is the peak intensity. The integral breadth of a Voigt function can be expressed as $\beta = \frac{\beta_G^{-1}exp(k^2)}{1-erf(k)}$, where $k = \frac{\beta_C}{\sqrt{\pi}\beta_G}$, β_C and β_G being the Cauchy and the Gaussian components of the integral breadth.

d) *Pseudo-Voigt function*: A pseudo-Voigt function is a linear superposition of a Cauchy function $C(x)$ and a Gaussian function $G(x)$ having equal widths. The function is defined as

$$pV(x) = I_{pV}(0)[\eta C(x) + (1-\eta)G(x)] \tag{2.4}$$

here η is the mixing parameter. The integral breadth for this function can be expressed as $\beta = w[\pi\eta + (1-\eta)\sqrt{\frac{\pi}{ln2}}]$

e) *Pearson VII function*: The Pearson VII function is expressed as

$$PVII(x) = I_{PVII}(0)[1 + 4(2^{-m} - 1)\frac{x^2}{w^2}]^{-m} \tag{2.5}$$

where m is the Pearson index. The integral breadth for this function is $\beta = \frac{\sqrt{\pi}\Gamma(m-0.5)}{\sqrt{2^{-m}-1}\Gamma(m)}w$.

2.4 Different model based techniques of XRDLPA

There are different model based techniques of XRDLPA which are very useful to extract the information about the microstructural imperfections inside the materials. These techniques are mainly based on the profile fitting method. In this method, a suitable Profile Shape Function (PSF) is assumed. The observed XRD peak profile is then fitted with this PSF. The main three parameters of a PSF are the peak position (2θ), the maximum intensity of the peak (I_0) and the FWHM of the peak. The best fit is attained by using a suitable optimizing algorithm. the various types of model based techniques of XRDLPA used in the present thesis is discussed below.

2.4.1 Single peak analysis by Scherrer's method

Among the different model based techniques used in XRDLPA, the simplest method is the Scherrers method [102], in this method it is assumed that the microstructural broadenings associated with the

XRD peak profiles are solely due to the effect of finite domain size, and no strain broadening is associated with this. The volume weighted domain size D_v is calculated from the values of total integral breadth of the XRD peak. This value of D_v represents the volume weighted domain size along a specific crystallographic direction corresponding to the XRD peak. According to Scherrer's method, the expression for D_v can be represented as:

$$D_v = \frac{0.9\lambda}{\beta cos\theta} \tag{2.6}$$

2.4.2 Single peak analysis by simplified breadth method

Unlike the Scherrer's method, in case of simplified breadth method [103] both the size and strain broadening effects are taken care. In this method, the size effect in the XRD peak shape is assumed to follow a Cauchy distribution whereas the strain effect is assumed to follow as Gaussian. The analytical form of each diffraction profile is approximated by Voigt function which is the convolution of the Cauchy and Gaussian function. The quality of the XRD peak is defined by a shape factor ϕ which is expressed as the FWHM of the XRD peak divided by its integral breadth. To make the fitting possible, the value of ϕ should be in a suitable range (0.63 to 0.94).The values of D_v (volume weighted domain size) and ε (upper value of the microstrain) are estimated using the following two relations [104]:

$$D_v = \frac{\lambda}{\beta_C cos\theta} \tag{2.7}$$

$$\varepsilon = \frac{\beta_G}{tan\theta} \tag{2.8}$$

where β_C and β_G are the Cauchy and Gaussian components of the integral breadths.

2.4.3 Double voigt method

Unlike the Scherrer's method and the simplified breadth method, the double Voigt method [105] assumes that both the size and strain effects in the broadening get the contribution from both Cauchy and Gaussian distribution. Here the XRD peak profile is fitted with a Voigt function and then the function is transformed into a Fourier series. The Fourier coefficient F(L) in terms of the column length L is then obtained and can be represented as follows:

$$F(L) = -2L\beta_C - \pi L^2 \beta_G^2 \tag{2.9}$$

where β_C and β_G are the cauchy and gaussian part of the total integral breadth β. β_C and β_G can be represented as:

$$\beta_C = \beta_{SC} + \beta_{DC} \tag{2.10}$$

$$\beta_G^2 = \beta_{SG}^2 + \beta_{DG}^2 \tag{2.11}$$

where, β_{SC} and β_{DC} are the Cauchy components of size and strain integral breadth respectively and β_{SG} and β_{DG} are the corresponding Gaussian components. The size and distortion coefficients are then obtained considering at least two reflections from the same family of the crystallographic planes.

After estimating the different components of integral breadths, these values are used to extract the size-strain information. The surface weighted average domain size D_s and the rms microstrain $\langle {\varepsilon_L}^2 \rangle^{\frac{1}{2}}$ can be expressed as:

$$D_s = \frac{1}{2\beta_{SC}} \tag{2.12}$$

$$\langle \varepsilon_L^2 \rangle^{\frac{1}{2}} = \frac{[\frac{\beta_{DG}^2}{2\pi} + \frac{\beta_{DC}}{\pi^2 L}]}{S^2} \tag{2.13}$$

where $S = \frac{2sin\theta}{\lambda}$

The volume weighted domain size D_v can be represented as:

$$D_v = \frac{1}{\beta_S} = \frac{\lambda}{\beta cos\theta} \tag{2.14}$$

The volume weighted column length distribution functions are given by:

$$P_v(L) \propto L \frac{d^2 A_S(L)}{dL^2} \tag{2.15}$$

For a size-broadened profile, the size coefficient can be represented as:

$$A_S(L) = \exp(-2L\beta_{SC} - \pi L^2 \beta_{SG}^2) \tag{2.16}$$

hence we get,

$$\frac{d^2 A_S(L)}{dL^2} = [(2\pi L\beta_{SG}^2 + 2\beta_{SC})^2 - 2\pi\beta_{SG}^2] A_S(L) \tag{2.17}$$

It has been shown by Selivanov and Smislov [106] that the equation 2.17 is a satisfactory approximation of the size distribution functions.

2.4.4 Williamson-Hall method

The Williamson-Hall method [107] is a very useful method of XRDLPA to study the isotropicity in the microstructural parameters. Though the method is based on the single peak analysis, the interpretation requires a collective information from all the XRD peak profiles over a wide range. In this method, it is assumed that both the size and strain broadened profiles are Lorentzian. Based on this assumption, a mathematical relation can be established between the integral breadth (β), the volume weighted average domain size (D_v) and the upper limit of the microstrain (ε) as follows:

$$\frac{\beta cos\theta}{\lambda} = \frac{1}{D_v} + 2\varepsilon S \tag{2.18}$$

where $S = \frac{2sin\theta}{\lambda}$. The plot of $\frac{\beta cos\theta}{\lambda}$ versus S gives the value of ε from the slope and D_v from the ordinate intercept. However, for anisotropic size and strain distributions, the values of D_v and ε become different along different crystallographic directions. Hence in this case it is not possible to find any linear trend in the Williamson-Hall plot.

2.4.5 Modified Rietveld method

The different model based techniques discussed above are mainly based on the analysis of each of the XRD peaks individually. On the other hand, the usefulness of the modified Rietveld method [108] is that it is based on the Whole Powder Pattern Fitting method. In this method, a wide range of the X-ray data containing a number of peaks is fitted simultaneously. The method is known as the modified Rietveld method due to its difference from the original Rietveld method [109, 110] which was mainly based on the crystal structure refinement technique. The earlier Rietveld technique has been modified by Lutterotti [108] to refine the structural and the microstructural parameters simultaneously. The corrections for preferred orientations have also been incorporated by him in the modified Rietveld technique. The beautiful feature of the Rietveld method is that it does not show any prior interest in advance to look at the observed intensity for to detecting the Bragg reflections, or to resolve the overlappped peaks.

In case of the constant wavelength X-ray diffracttion pattern, the recorded data is the intensity values with the variation of diffraction angle. A wide range of XRD data containing a significant number of XRD peak profiles is required to perform the modified Rietveld method sucessfully. The method requires the information about the crystal structure (e.g. the lattice parameters and the cell angles, atom coordinates), atom types (to know the atomic scattering factors) and the instrumental parameters to calculate the XRD full profile and to match it with the experimental one. A non linear least square fitting method is used to obtain the best fit. The quantity which is minimised during the

fitting process is:

$$S_y = \sum_i W_i (Y_i - Y_{ci})^2 \tag{2.19}$$

where Y_i and Y_{ci} are the observed and calculated intensity at the i-th step and $W_i = \frac{1}{Y_i}$. The expression for the calculated intensity Y_{ci} is:

$$Y_{ci} = S \sum_k L_k |F_k|^2 \phi(2\theta - 2\theta_k) P_k A + Y_{bi} \tag{2.20}$$

Here S is the scale factor, the miller indices h, k, l for a particular Bragg reflection is represented as k. The term L_k contains Lorentz, polarization and multiplicity factors. The reflection profile function is represented by ϕ. P_k and A are the preferred orientation function and the absorption factor respectively. F_k is the structure factor of the k-th bragg reflection and Y_{bi} is the background intensity at the ith step. The background is generally refined by assuming some polynomial function of higher order. The order of the polynomial is normally taken as four or some other larger value.

The reflection profile function ϕ controls the shape of the XRD peak profile which is a very important factor carrying the microstructural information of the materials. Beside this, ϕ also contains the effects due to instrumental limitation and limitations due to the specimen features. The observed XRD profile $h(2\theta)$ can be expressed as:

$$h(2\theta) = W(2\theta)) * f(2\theta) = [W(2\theta) * G(2\theta)] * f(2\theta) + background \tag{2.21}$$

Where $W(2\theta)$ is the contribution due to the spectral distribution [111] and $G(2\theta)$ is the instrumental contribution. The intrinsic function $f(2\theta)$ takes the contribution from the inherent Darwin width [112] (which comes during diffraction due to the uncertainity principle) as well as from the microstructural imperfections (like finite domain size and the microstrain within the domain) inside the sample. The convolution of all these three factors results in the observed diffraction pattern.The convolution operator in between the functions is indicated by the sign $*$.

The function $G(2\theta)$ contains five non spectral instrumental contribution as stated below:

i) X-ray source image: For a closed tube system, the contribution for the X-ray source image can be approximated with a symmetric Gaussian curve having FWHM of 0.02° using a take off angle of 3°. The effects of the monochromators to this contribution have been described by Cox *et al.* [113] and do not introduce any asymmetry to the Gaussian shape.

ii) Specimen flatness: Under the Bragg-Brentano focussing condition, the specimen surface should be flat so that it lies on the perimeter of the focussing circle. However, with change in the diffraction angle, the focussing circle continuously changes its radius. Due to this 'out of focus' condition, a $cot\theta$ dependent term is introduced which produces a small asymmetry in the profile. This error becomes noticable particularly at low angle since in this case the effect due to the 'out of focus' condition becomes large.

iii) Beam divergence: The axial divergence of the incident beam also contributes as an error to the observed XRD profile. This error follows a $cot\theta$ dependence to the observed profile at low angle and introduces significant amount of asymmetry, especially at the lowest angle.

iv) Specimen transparency: Due to the finite absorption coefficient of the specimen, a part of the incident X-ray beam looks deeper inside the sample. Due to this reason, an 'out of focus' condition comes into play which afects the observed XRD profile. For the materials with low absorption coefficient and for the loosely bound powder samples, this effect produces a substancial amount of asymmetry in the observed profile.

v) Receiving slit width: Due to the presence of the receiving slit before the detector, a symmetric term is contributed to the observed profile.

In the present thesis, all the microstrutural analysis by modified Rietveld method have been performed using the program LS1 [108]. In this program, the reflection profile is modelled using the pseudo-Voigt function. For the successful extraction of the microstructural parameters using modified Rietveld method, it is very important to incorporate the instrumental corrections during the fitting

process. According to Caglioti *et al.* [114], if no microstructural effects are involved in the observed profile, then the variation of the FWHM(H) of the reflection profiles with the diffraction angle can be written as:

$$H = \sqrt{U\tan^2\theta + V\tan\theta + W} \tag{2.22}$$

here U, V and W are called the Caglioti parameters. The variation of the pseudo-Voigt mixing parameter (η) is expressed as:

$$\eta = a + b(2\theta) \tag{2.23}$$

The terms U, V, W, a and b are constants and they are known as the instrumental broadening parameters. To estimate the values of these instrumental broadening parameters, a full range X-ray data for the standard LaB_6 powdered sample has been collected. Every peak of that data has been fitted individually with the pseudo-Voigt function and the values of the FWHM and η has been noted. Hence with the help of the obtained values of H and η, the instrumental broadening parameters have been estimated using equations 2.22 and 2.23. Figure 2.6 shows the variation of H^2 with $tan\theta$. The data have been fitted using the equation 2.22 and the values of U, V, W have been estimated from the fit. The variation of the pseudo-Voigt mixing parameter η with 2θ has been shown in figure 2.7. Equation 2.23 have been used to fit this data and the parameters a, b have been estimated.

After the successful determination of the instrumental broadening parameters, the sample XRD data has been used for analysing to extract the size-strain information. According to the Fourier analysis developed by Nandi *et al.* [115] using single peak method, The normalised Fourier coefficient (T_{pV}) of the pseudo-Voigt function can be written as:

$$\frac{dT_{pV}}{dL_{L=0}} = -\frac{1}{D_{av}} \tag{2.24}$$

Where D_{av} is the average domain size. In this case, it is assumed that the domain is isotropic in size along all the crystallographic directions. L is the column length. The expression for T_{pV} for $L = \frac{D_{av}}{2}$

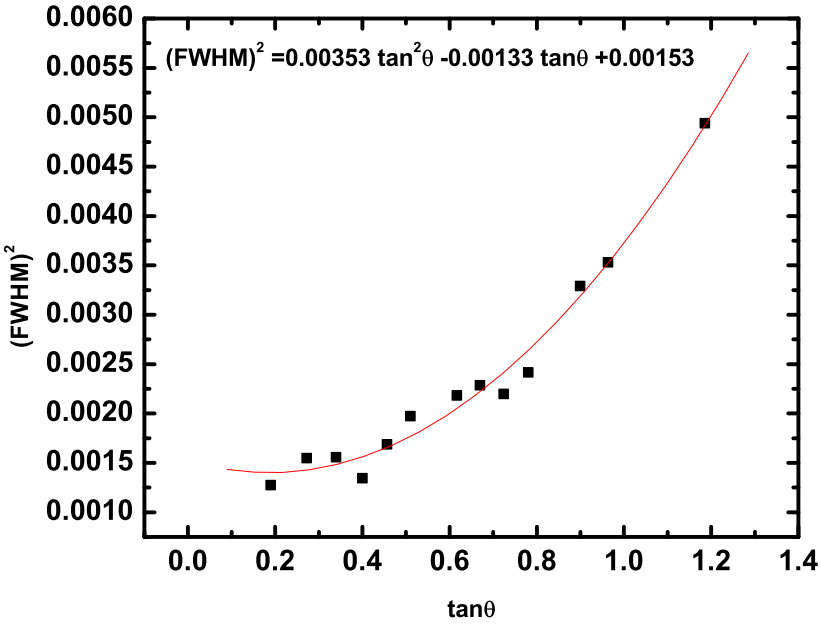

Figure 2.6: The caglioti plot:variation of H^2 with $tan\theta$.

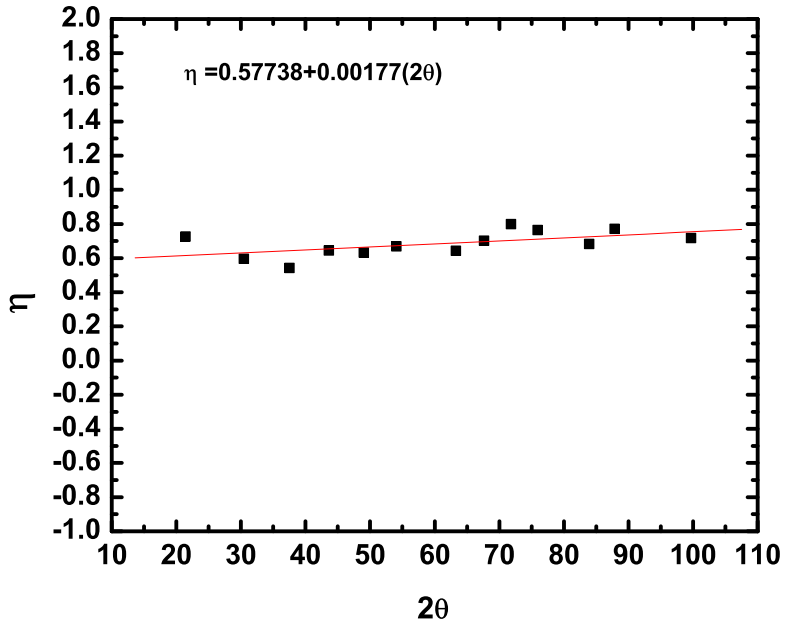

Figure 2.7: variation of the pseudo-Voigt mixing parameter η with 2θ.

can be written as:

$$T_{pV_{L=\frac{D_{av}}{2}}} = [1 - \frac{\pi^2 \langle \varepsilon_L^2 \rangle D_{av}^2}{2d^2}] \exp(-\frac{1}{2}) \tag{2.25}$$

where $\langle \varepsilon_L^2 \rangle^{\frac{1}{2}}$ is the microstrain and d is the interplanar spacing. If the Gaussian distribution of microstrain is assumed, then equation 2.25 can be represented as:

$$T_{pV_{L=\frac{D_{av}}{2}}} = \exp(-\frac{\pi^2 \langle \varepsilon_L^2 \rangle D_{av}^2}{2d^2} - \frac{1}{2}) \tag{2.26}$$

On ther other side, the expression for T_{pV} in terms of the pseudo-Voigt fitting parameters can be represented as [116]:

$$T_{pV}(L) = \frac{Z}{1+Z} \exp(\frac{-\pi^2 \sigma^2 L^2}{ln2}) + \frac{1}{1+Z} \exp(-2\pi\sigma L) \tag{2.27}$$

where,

$$Z = \frac{\eta}{(1-\eta)(\frac{\pi}{ln2})^{\frac{1}{2}}} \tag{2.28}$$

and

$$\sigma = \frac{2}{\lambda}[sin(\theta_0 + HWHM) - sin\theta_0] \tag{2.29}$$

Using equations 2.24, 2.26 and 2.27 we get:

$$\frac{Z}{1+Z} \exp(-\frac{(Z+1)^2}{16ln2}) + \frac{1}{1+Z} \exp(-\frac{(Z+1)}{2}) = \exp(-\frac{\pi^2 \langle \varepsilon_L^2 \rangle D_{av}^2}{2d^2} - \frac{1}{2}) \tag{2.30}$$

$$HWHM = sin^{-1}[\frac{\lambda(Z+1)}{4\pi D_{av}} + sin\theta_0] - \theta \tag{2.31}$$

$$\eta = \frac{Z}{Z + (\frac{\pi}{ln2})^2} \tag{2.32}$$

Some known values of D_{av} and $\langle \varepsilon_L^2 \rangle^{\frac{1}{2}}$ are used to perform the refinement process using the non-linear least square fitting method. After the best fit is obtained, the values of D_{av} and $\langle \varepsilon_L^2 \rangle^{\frac{1}{2}}$ are recorded as results.

The preferred orientation is also a very important parameter which can affect the observed XRD peak significantly. For the metals and alloys having less number of slip systems, this preferred orientation of the domains comes into picture during the metallic fabrication, directional melting or solidification etc, and causes significant changes in the integrated intensity of the observed profile. The distortion in the observed XRD profile caused by the preferred orientation can be mathematically modelled using the preferred orientation function P_k. Numorous studies are there to find the nature of this preferred orientation function P_k [110, 117, 118, 119, 120, 121, 122, 123]. Among them, the March-Dollase preferred orientation function [117, 118] is the most popular. This function is expressed as:

$$P_k(\alpha) = (r^2 cos^2\alpha + \frac{sin^2\alpha}{r})^{\frac{3}{2}} \tag{2.33}$$

where α is the angle between the hkl plane and the preferred orientation plane and r is an adjustable parameter.

During the Rietveld refinement process, the refinable parameters are adjusted until the residual in the equation 2.19 is minimised. The quality of this 'best fit' depends on the suitability of the model and also on type of the minimum condition (e.g. is it local or global minima) it reaches. Hence, it is very necessary to introduce some criteria of fit during the refinement process. In case of the modified Rietveld refinement, the criteria of the fit is defined as:

$$R_{wp} = \{\frac{\sum_i W_i(Y_i - Y_{ci})^2}{\sum_i W_i Y_i^2}\}^{\frac{1}{2}} \tag{2.34}$$

The goodness of the fit (Gof) can be represented as:

$$Gof = \frac{R_{wp}}{R_e} \tag{2.35}$$

where,

$$R_e = [\frac{(N-P)}{\sum_i W_i Y_i^2}]^{\frac{1}{2}} \tag{2.36}$$

here N is the number of observatios and P is the number of parameters adjusted. For a best acceptable fit, Gof should be near to 1.

2.5 Microstructural Characterization by XRDLPA: a brief review

There are various types of model based techniques of XRDLPA developped by different eminent scientists which have been reviewed by Langford [124], Toraya [125] and Langford and Louer [126]. Among them, the modified Rietveld method is the most reliable one because it is based on the whole powder pattern fitting technique. The method was developed by Rietveld in 1969 [110] where the X-ray diffraction lines and their intensities are constrained by a structural model comprising of the different crystallographic parameters as well as the atomic information. In the early times (before 1980) the studies of X-ray diffraction pattern from the microstructural point of view was restricted only to the materials of higher symmetry. However after the introduction of the Rietveld method and method of pattern decomposition [127], scientists started showing their interest to apply these methods to study the materials of the lower symmetry. At the first stages, just after the introduction of the Rietveld method, it was used mainly for structural refinement of different materials. In 1978, Langford [104] and Nandi and SenGupta [115] introduced the Voigt function modelling of combined size-strain broadened profiles. After that, modelling by Voigt, pseudo-Voigt and Pearson VII function has attracted a great interest for determining the size-strain parameters using either multiple order integral breadth method [128], or single line integral breadth method [103]. Extensive number of studies on the microstructural characterisation by different model based techniques have been performed by Enzo *et al.* [129], Benedetti *et al.* [130], Scardi *et al.* [131, 132], Langford [133], Balzar [134], Balzar and Ledbetter [135, 136] and Shee *et al* [137].

Beside the studies on the size broadening effects on the XRD profile, there is also an extensive amount of reported works to study the effect of strain distribution on the observed XRD profile. There are numorous amount of studies reported by Wilson [138], Wilkens [139, 140] and Ungar

et al. [141] where the line profile based modelling was performed to study the strain fields of the dislocations and their distribution. In a restrictedly random dislocation model proposed by Wilkens [139], he showed a discrepancy between the theoretically calculated strain Fourier coefficients and that obtained from Warren Averbach analysis [89, 90]. He introduced an extra factor in the expression of Fourier coefficients which was called the contrast (orientation) factor and produces anisotropic line broadening corresponding to dislocation contrast. The above theory was applied by Kuzel and Klimanek [142] to plastically deformed zirconium to determine the dislocation content and type from the anisotropic strain broadening in the deformed material. Beside this, a general type of theory about the line broadening due to dislocations was developed by Groma *et al.* [143].

2.6 Positron annihilation spectroscopy

Beside the studies of different microstructural parameters which are mainly controlled by dislocations, it is also very interesting to study the nature of the point defects inside the materials and there role in controlling their microstruture. The positron annihilation spectroscopy (PAS) is a very useful tool for performing these types of studies because the positron is highly sensitive to the vacancy type of defects [144, 145]. Especially for the materials under irradiation, the irradiation induced point defects play significant roles in controlling their resultant microstructure. In the present thesis, a successful attempt has been made to use PAS to know how the point defects control the microstructure of Zr1Nb alloy under heavy ion irradiation.

The positron (e^+) being an antiparticle of electron, it has the rest mass same as that of an electron (511 KeV) and the charge is $+e$. This particle interacts with electron via electromagnetic interaction and annihlates in a very short time. When a positron enters in a material, it first looses it's kinetic energy through different processes. After thermalization, the positron propagates throgh the material as a Bloch wave and then annihilates through the interaction with the electrons present in the material, resulting in the emission of photons [146]. Hence the lifetime of a positron inside

a material depends on the electron density distribution inside that material, and is a very important signature carrying the information about the materials which are closely related to the elctron density distribution.

There are two different modes in which the positron annihilates with the electron. One is the two gamma annihilation mode, another is the three gamma annihilation modes. However, the two gamma annihilation mode is much more favourable and hence the occurence of the three gamma annihilation mode is neglected in PAS. For the non-relativistic case, the cross section of the two gamma annihilation mode for a free positron and a free electron is

$$\sigma_{2\gamma} = \frac{\pi r_0^2 c}{v} \tag{2.37}$$

where r_0 is the classical radius of the elctron or positron and v is the positron velocity. hence the annihilation rate of the positron (probability of annihilation per unit time) can be written as:

$$\lambda_{2\gamma} = \sigma_{2\gamma} v n_e = \pi r_0^2 c n_e \tag{2.38}$$

where n_e is the localised electron density at the position of the positron. From equation 2.38 it is clear that the lifetime of the positron (τ) in a material, which is just the inverse of the postron annihilation rate, is independent of the positron velocity and only depends upon the electron density it faces during the annihilation.

However, the situation is somewhat different when the positron enters in a system with a large number of electrons. In this case, the interaction between the coulomb field of the positron and the coulomb field due to the electron cloud results in an increase in the localised electron density faced by the positron. In these circumstances, equation 2.38 can be modified as:

$$\lambda_{2\gamma} = \varepsilon \pi r_0^2 c n_e \tag{2.39}$$

here the parameter ε refers to the increase in the localised electron density due to the presence of the positron.

2.6.1 The two-state trapping model

From equation 2.39 it is clear that, for a defect free solids the positrons will get annihilated after having the same lifetime, as they will face a uniform distribution of the electron. However, the picture will be somewhat different if the defects are present in the material. In this case, at the positions of the defects, there will be a lack in the concenration of electrons and they will act as the trapping centers for the positrons. Hence the positron which will get annihilated at the defect sites, will have a different lifetime depending on the nature of the defect. An extensive review on this topic has been given by Siegel [147, 148].

Thus the trapping model of positrons is a very useful tool to know about the nature and concentration of the defects inside a material [149, 150]. According to this model, there are two different states of positrons inside a material. One is the Bloch state, and another is the defect trapped state. the lifetime of the positrons in a completely defect free materials can be represented as:

$$\tau_b = \lambda_b^{-1} = \frac{1}{\pi r_0^2 c n_e} \tag{2.40}$$

However, if defects are present in the materials, three differet processes take place:

i) The annihilation of the positrons in the defect free regions during their propagation as Bloch wave, with an annihilation rate λ_b.

ii) The trapping of the positrons from the Bloch state to the defect trapped state, with a trapping rate κ_t.

iii) The annihilation of the trapped positrons with an annihilation rate λ_t.

If n_b is the concentration of the positrons in the bulk and n_t is that for the trapped positrons, then the corresponding rate equations can be written as:

$$\frac{dn_b}{dt} = -\lambda_b n_b - \kappa_t n_b \tag{2.41}$$

and

$$\frac{dn_t}{dt} = -\lambda_t n_t + \kappa_t n_b \tag{2.42}$$

Solving these two equations we get,

$$n_b = N_0 e^{-\lambda_1 t} \tag{2.43}$$

where $\lambda_1 = \lambda_b + \kappa_t$. The corresponding lifetime of the positron is $\tau_1 = \frac{1}{\lambda_1} = \frac{1}{\lambda_b + \kappa_t}$. The solution of the equation 2.42 is give by:

$$n_t = \frac{N_0 \kappa_t}{\lambda_1 - \lambda_t}\{e^{-\lambda_t t} - e^{-\lambda_1 t}\} \tag{2.44}$$

The total number of positrons present in the system at time t can be represented as:

$$N(t) = n_b(t) + n_t(t) = N_0 e^{-\lambda_1 t} + \frac{N_0 \kappa_t}{\lambda_1 - \lambda_t}\{e^{-\lambda_t t} - e^{-\lambda_1 t}\} = I_1 e^{-\lambda_1 t} + I_2 e^{-\lambda_t t} \tag{2.45}$$

The lifetime of the trapped postrons can be written as $\tau_2 = \frac{1}{\lambda_t}$. I_1 and I_2 are the corresponding intensities. After normalization with N_0, I_1 and I_2 can be represented as:

$$I_1 = 1 - \frac{\kappa_t}{\lambda_1 - \lambda_t} \tag{2.46}$$

and

$$I_2 = \frac{\kappa_t}{\lambda_1 - \lambda_t} \tag{2.47}$$

Here τ_2 is a vary important parameter which carries the information about the nature of the defects present in the material. Since the electron density at the defects is less than the bulk electron density, it is obvious that $\tau_2 > \tau_b$. The more is the value of τ_2, more is the size of the defect.

The trapping rate κ_t is also a significant paramter which depends upon the concentration of the defects present in the material. It is represented as:

$$\kappa_t = \sum_i \mu_i C_i \tag{2.48}$$

where μ_i and C_i is the trapping coefficient and the concentration for the i-th type of defects.

2.6.2 Positron annihilation spectroscopy: the experiemental details

In the present thesis, the PAS experiment have been carried out to know about the role of defects in controlling the irradiated microstructure of Zr-1Nb alloy samples. The positron source used in this case is the salt of ^{22}Na. ^{22}Na is a radioactive isotope of sodium which emits one positron and simultaneously one gamma photon with energy 1.274 MeV (figure 2.8). A weak positron source (having a strength arround 10 μCi) was prepared by depositing the ^{22}NaCl solution on a thin nickel foil (thickness arround 2 μm). Then the foil was sandwitched between the two identical sheets of same sample and placed in between two BaF_2 detectors. Thus when the positron enters into the material, it interacts with the electron density present in the material and gets annihilated by producing two gamma photons each having energy $\approx$ 511 KeV energy. The lifetime of the positron is estimated by measuring the small time difference between the birth gamma photon (1.274 MeV) and the annihilation gamma photon (511KeV). This time difference is referred as the lifetime of that specific positron. The time resolution of the prompt gamma-gamma coincidence of the circuit was 200ps as measured by a ^{60}Co gamma source.

The data obtained from the PAS experiement contains three contributions: the background, the instrumental part and the part containing the information about the materials (the residual spectrum). The programs RESOLUTION and POSITRONFIT [Kirkegaard (1981)] was used to analyse the data. After the background correction, the instrumental part has been deconvoluted from the data. The

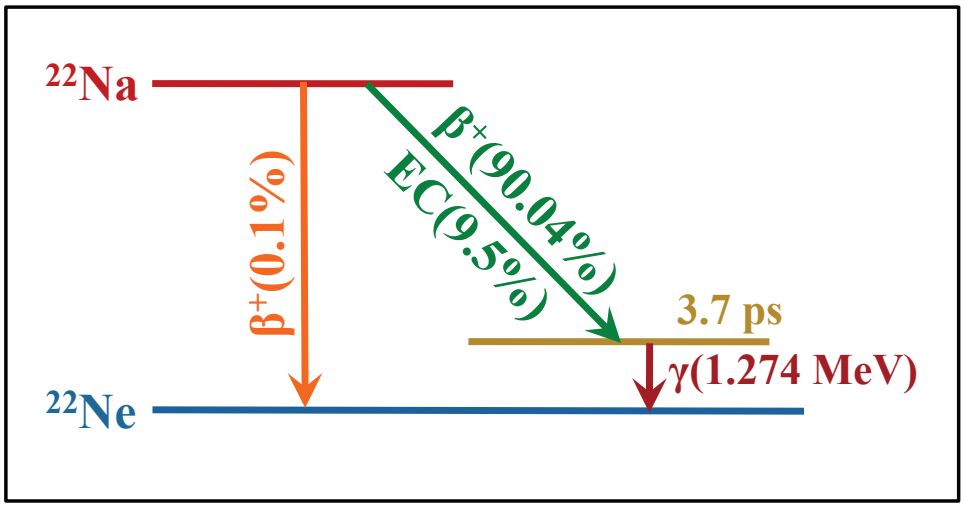

Figure 2.8: Energy level diagram for the decay of ^{2}2Na.

residual spectrum have been used for fitting. The fitting was done with a multi exponential decay function and the best fit is obtained.

Chapter 3

Study of Microstructure of Oxygen Irradiated Zr-1Nb Alloy using XRD and PAS

3.1 Introduction

Zirconium based alloys are very important structural materials in nuclear industries, because of their low neutron absorption cross section, good corrosion resistance, better mechanical properties at elevated temperatures and better resistance to irradiation induced dimensional changes [151]. It is very popular structural materials in PHWR. To meet the demands of high burn up , higher coolant temperature and partial boiling of coolant, there is always a search for new zirconium alloys which can withstand the severe operating conditions inside a nuclear reactor. In this respect, several zirconium based alloys such as Zirlo (Zr-1Nb-1Sn-0.1Fe), Zr-1Nb, Zr-0.1Nb-1.0Sn-0.2Fe-0.1Cr have been developed as candidate materials for fuel cladding tube and have shown considerable promises [151, 152, 153]. The performance of these cladding materials is mainly influenced by their microstructures, alloying elements, precipitate characteristics, nature of defects etc. The irradiation induced point defects also play a significant role in controlling the microstructure, mechanical and creep properties of these alloys [153]. However, the nature of production of these defects is very complex and depends on the initial microstructure, alloying elements, dose and dose rate. Even the presence of impurity atoms

at the substitutional or interstitial position of the host atom matrix play significant role in affecting the interaction of these defects with the existing microstructure. Especially at the low dose and low dose rate, a transient variation of microstructure is observed before attaining a steady state, where the microstructure becomes dose dependent [154]. So it is interesting to study the evolution of microstructure in the low dose.

3.2 Objective of the present study

In this work, the Zr-1Nb alloy samples have been irradiated with 116 MeV O^{5+} with low dose and low dose rate. XRDLPA has been used to characterize the microstructural parameters of these irradiated samples. The nature of vacancy clusters created in the irradiated samples has been studied by PAS. During the XRD experiment X-ray probes an average volume of 10^9 μm^3 of the sample. Thus the global information about the microstructure of the irradiated samples can be extracted successfully in a statistical manner using XRDLPA. On the other hand, PAS helps us to study the intrinsic characteristics of the lattice defects in much shorter length scale. Though these two experiments are independent, the results obtained from them are complementary to each other, and corroboration of these results can give a detail account of the irradiated microstructure in a non destructive way.

3.3 Experimental details

The Zr-1Nb alloy was prepared by hot extrusion and beta-quenching followed by a second hot extrusion and cold rolling. This cold rolled sheet of Zr1Nb were then annealed at 853K for one hour. The thickness of the sheet was 0.6 mm. Samples of dimension 10mm $\times$ 10mm were cut from that sheet.

The irradiation experiment was performed on the samples using the 116 MeV O^{5+} beam from Variable Energy Cyclotron (VEC), Kolkata. The irradiation doses were 5×10^{17}, 1×10^{18}, 2×10^{18} and

8×10^{18} O^{5+}/m^2. The beam current was kept constant at 150 nA. The sample was kept press-tight with an aluminium flange which was directly cooled by continuous flow of water. During irradiation, the average temperature of the sample did not rise above 313 K as measured by the thermocouple connected to the closest proximity of the sample. The rise of temperature upto 313 K was attained within 160 seconds in each case and then became stable at that temperature.

The X-ray diffraction profiles of all the samples were recorded with the help of Bruker D8 Advance diffractometer with Cu-Kα radiation. The range of 2θ was 30° to 101° with a step scan of 0.02°. The time per step was 20 seconds. PAS experiment was performed on the unirradiated sample as well as on the samples irradiated at different doses. Detail of the experimental method for PAS has been discussed already in Chapter 2. ^{22}Na with strength $\approx$ 10 μCi was used as the positron source for this experiment. The time resolution of the prompt gamma-gamma coincidence of the circuit was 200ps as measured by a ^{60}Co gamma source.

Isochronal annealing experiment was also performed on the sample irradiated at a dose of 1×10^{18} O^{5+}/m^2 in a temperature range of 373K to 1073K at an interval of 100K (1 hour annealing at each temperature stage). PAS measurements were carried out on this sample at different temperature stages of the isochronal annealing experiment.

3.4 Method of analysis

The broadenings associated in the XRD peaks obtained from the unirradiated and irradiated samples, carry the information about the microstructural features inside the samples. This microstructural information can be extracted from the X-ray diffraction patterns by analyzing them using suitable model based approaches. The Williamson-Hall technique and the Modified Rietveld Method have been adopted here to study the microstructural variation as a function of dose from XRDLPA. The data obtained from PAS have been analyzed using the conventional two-state trapping model. Detailed discussion on the abovementioned methods have been given in chapter 2.

3.5 Results and discussion

SRIM 2003 [155] was used to calculate the range of 116 MeV O^{5+} ions in Zr-1Nb. The total target displacements of the collision events in Zr1Nb alloy has been shown in Figure 3.1. The range was found to be 66 μm. The maximum dpa at the peak region was found to be 0.15 for the highest dose of irradiation. The average dose rate was estimated and it was found to be 2.4×10^{-5} dpa/s for the highest dose of irradiation.

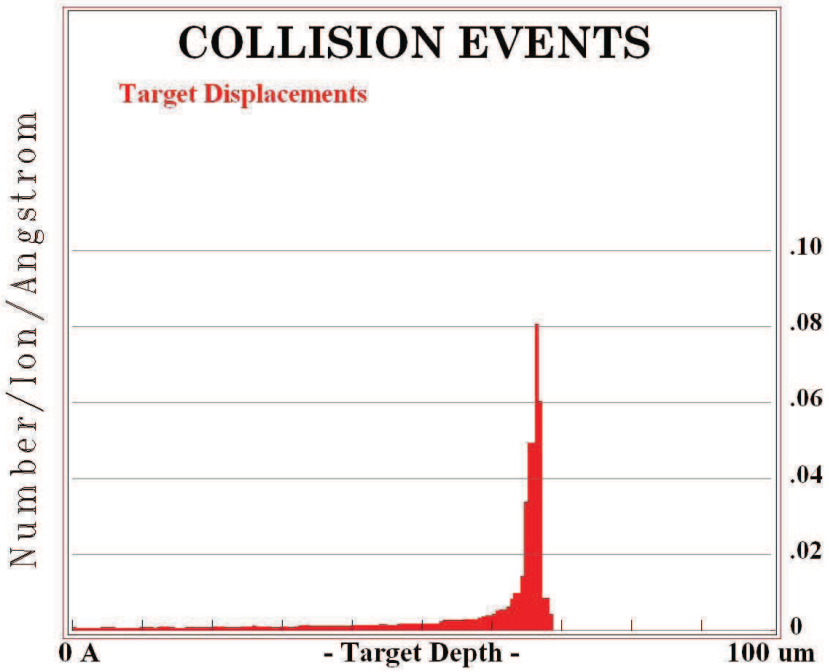

Figure 3.1: Target displacements by 116 MeV $O^{5}+$ ions on Zr1Nb alloy.

The X-ray diffraction patterns obtained from the unirradiated sample as well as from the highest irradiated samples has been shown in Figure 3.2. The enlarged view of the (101) peaks for both of the diffraction patterns has been shown in the inset. In this figure, broadenings can be clearly observed for the XRD patterns for irradiated samples. This broadening has been arisen due to the microstructural changes in the samples due to the heavy ion irradiation. Again, it is clear from Figure

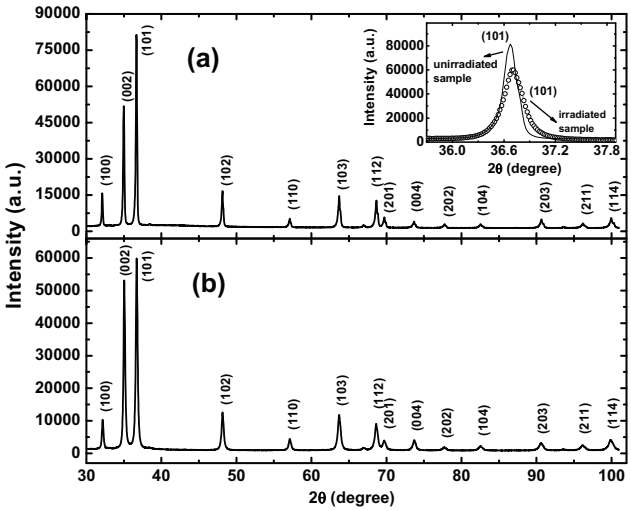

Figure 3.2: XRD profiles for (a) unirradiated sample and (b)sample irradiated at the highest dose (8×10^{18} O^{5+}/m^2.) The broadening of the (101) peak for the irradiated sample with respect to the unirradiated one has been shown clearly in the inset.

3.2 that, the relative intensities of the XRD peaks did not change much even up to the highest dose of irradiation. This observation ensures that, the initial texture of the sample did not change significantly due to the effect of heavy ion irradiation. Thus the broadenings associated in the XRD profiles for irradiated samples have been arisen solely due to the change in domain size and microstrain inside the samples.

The Williamson Hall (W-H) plots for the unirradiated and irradiated samples have been shown in Figure 3.3. If the domain size and strain distributions in the sample become isotropic, i.e. if their values along different crystallographic directions remain unchanged, then the plots obtained from the W-H equation (equation 2.18) will show a linear trend. However, for our case, the points in the W-H plots were found to be scattered for all the samples which implies a strong anisotropy in the domain size and microstrain along different crystallographic directions. Moreover, starting from the unirradiated sample, the scattered nature of the points in the W-H plots becomes less with increasing dose of irradiation, tending to get a nearly linear trend at the dose of 2×10^{18} O^{5+}/m^2. However, after this dose of irradiation, the points in the W-H plot again get more scattered. Since the initial texture

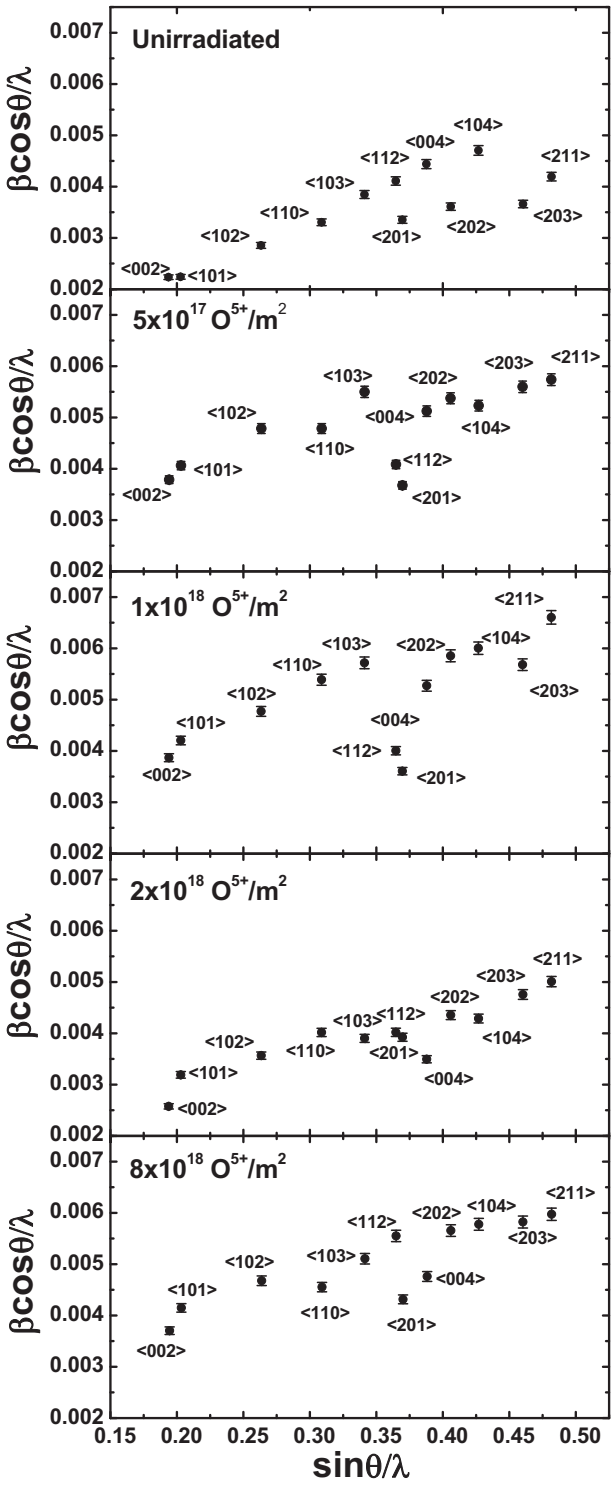

Figure 3.3: Williamson-Hall plots for the unirradiated and irradiated Zr-Nb samples.

of the sample did not change much due to irradiation, so the changes in the nature of the W-H plots is mainly due to the changes in the domain size and strain distribution inside the samples caused by the heavy ion irradiation.

The estimated values of the integral breadth β along each crystallographic direction have been plotted against the dose of irradiation, which is shown in Figure 3.4. In general, during heavy ion irradiation, since the microstructural imperfections in the irradiated samples increase with the dose of irradiation and then saturates at the higher doses, so one should also get an increase in β with increasing dose of irradiation. However in the present study, sudden decrease in the value of β was observed at a dose of $2\times10^{18}O^{5}+/m^{2}$, along the most crystallographic directions. Since the integral breadth β for a certain XRD peak profile carries the microstructural information of the sample along the corresponding crystallographic plane, so it is expected that the change in microstructure of the samples during the heavy ion irradiation is responsible behind this type of anomalous observation. However, a detailed discussion on this observation will be made in the later part of this section.

A typical Rietveld fit for the XRD pattern of Zr-1Nb sample with highest dose of irradiation (2×10^{18} O^{5+}/m^{2}) has been shown in Figure 3.5. The microstructural parameters like surface weighted domain size (D_S), average microstrain ($\langle\varepsilon_L^2\rangle^{\frac{1}{2}}$ and average dislocation density (ρ) has been estimated by Modified Rietveld method. The variations of these microstructural parameters against the dose of irradiation have been plotted in Figure 3.6. A drastic decrease in domain size (Figure 3.6(a) and subsequent increase in microstrain (Figure 3.6(b) is observed at the initial stages of irradiation, which tend to saturate at the higher irradiation doses except at the dose of 2×10^{18} O^{5+}/m^{2} (marked by arrow). The variation of the estimated dislocation density has been shown in Figure 3.6(c). The dislocation density also increases initially with increasing dose of irradiation and then shows an anomaly at that specific dose of 2×10^{18} O^{5+}/m^{2}. All of these observations are in correspondence with the result shown in Figure 3.4, and can be explained as follows:

The radiation damage by heavy ions (O^{5+}) produces displacement cascade in the irradiated sample consisting of highly localized interstitials and vacancies. During irradiation, these mobile

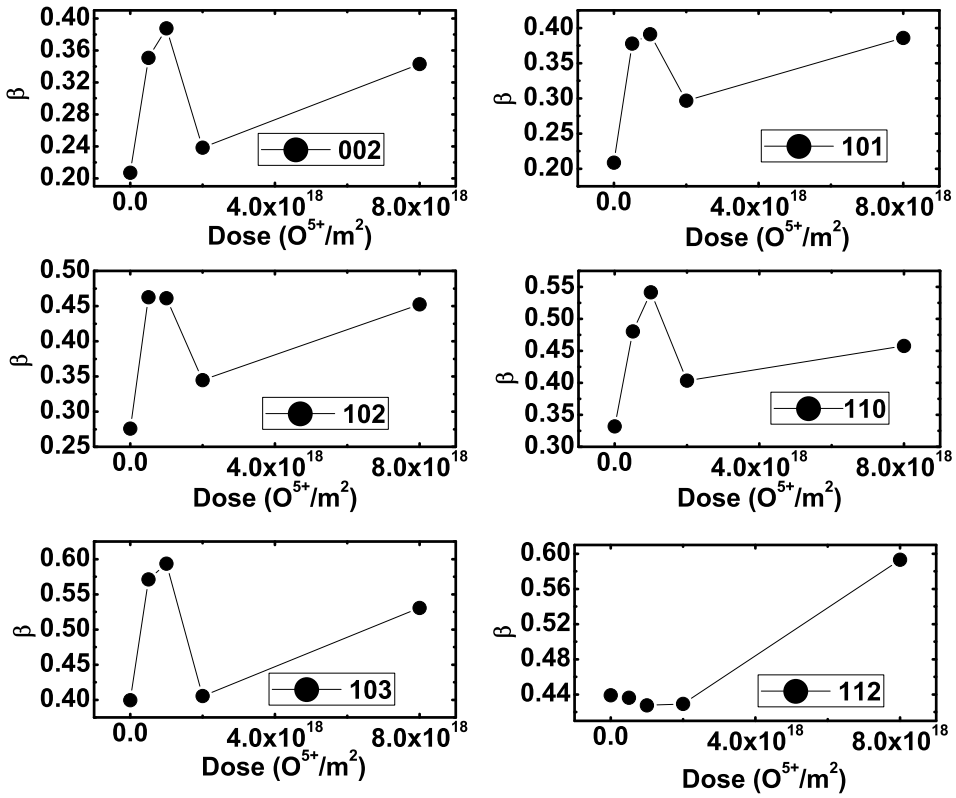

Figure 3.4: Variation of β with irradiation dose for the XRD peaks of Zr1Nb samples along different crystallographic directions.

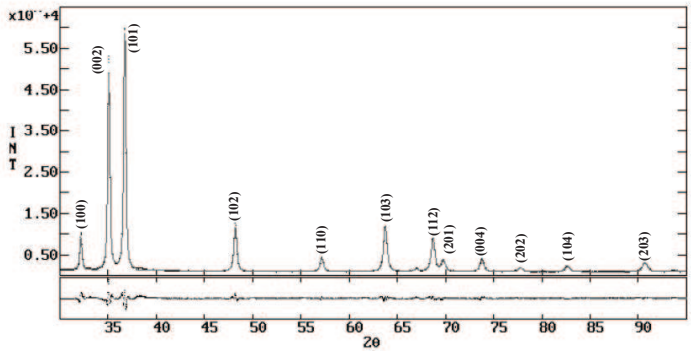

Figure 3.5: Rietveld fit for the XRD porfiles of oxygen irradiated Zr1Nb sample at a dose of 8×10^{18} O^{5+}/m^2.

point defects interact with the existing microstructure of the sample by long range diffusion [156]. The mechanism behind the migration of these mobile point defects is mainly governed by three different reaction paths: i) the annihilation of point defects at the extended sinks such as surfaces, grain boundaries and the existing dislocation network, ii) the nucleation of the point defects to make defect clusters; this process take place by the homogeneous reaction between the point defects of the same type, iii) the growth of the defect clusters like the dislocation loops and voids by agglomeration of the point defects.

The enhancement of the radiation induced diffusion during irradiation results in the migration of the vacancies, their agglomeration and then collapsing in the shape of dislocation loops. However, the formation of the dislocation loops by collapsing of the vacancy clusters is only possible when the concentration of the vacancies in the irradiated materials is in excess to their equilibrium values. It is observed that, at the initial stages of irradiation, the density of dislocation increased up to an order of magnitude. This increased dislocation density in turn act as a sink for the vacancies. Hence, annihilation of the vacancies also takes place during irradiation as a competing process to the generation of

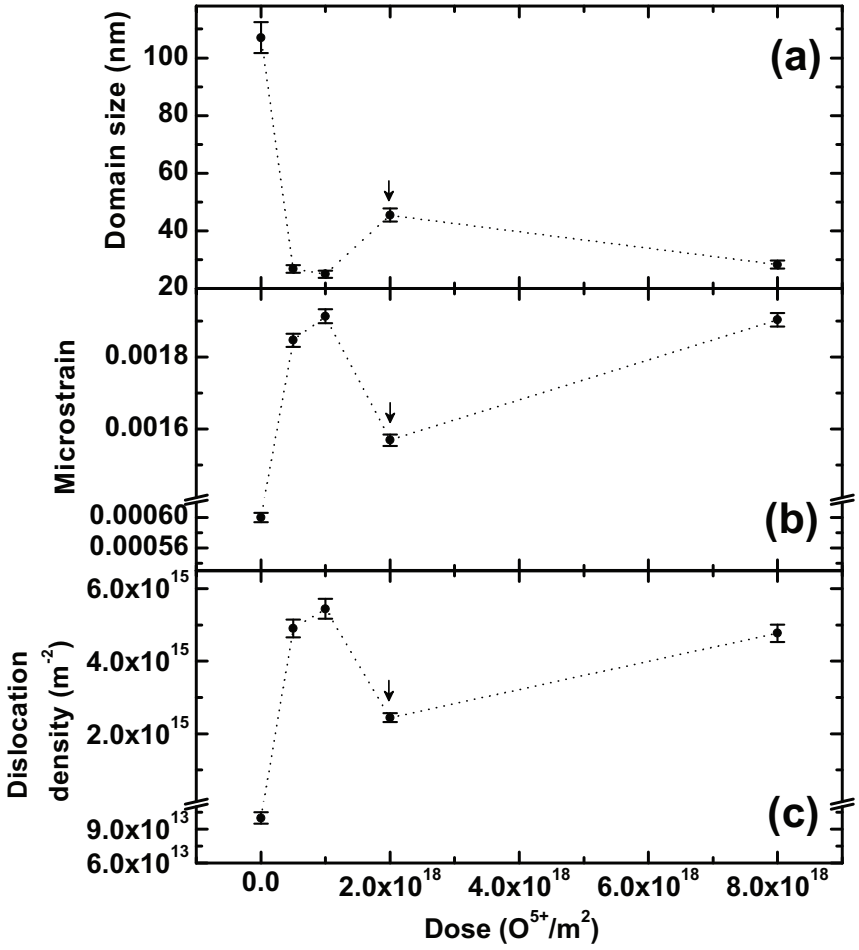

Figure 3.6: Variation of (a) average domain size, (b) average microstrain and (c) average dislocation density for Zr1Nb samples with different irradiation doses.

vacancies. With further increase in irradiation dose, the annihilation of vacancies increases because of the increase in sink density (dislocation density) due to the collapse of new vacancy clusters. When the rate of annihilation of vacancies is comparable with the rate of its generation, a saturation of the dislocation density is observed. This effect has been observed in the earlier work with Ne^{6+} and O^{5+} irradiated Zr-1Nb-1Sn-0.1Fe samples [157, 158, 159]. However, in case of proton (light ion) irradiation studies [160], no clustering beyond trivacancy was observed even up to the highest dose of irradiation characterized by PAS. Moreover, the dislocation density also did not show any significant change in case of the proton irradiated Zr-1Nb-1Sn-0.1Fe samples [161].

In our present work, a sudden decrease in the dislocation density has been observed at a specific irradiation dose of 2×10^{18} O^5+/m^2 (Figure 3.6(c)). This anomaly can be well explained by taking recourse to the PAS results obtained in our samples. The value of the positron lifetime in case of the unirradiated sample was found to be 231ps (Figure 3.7) which corresponds to that of a monovacancy in pure Zr (228 ps) [162].

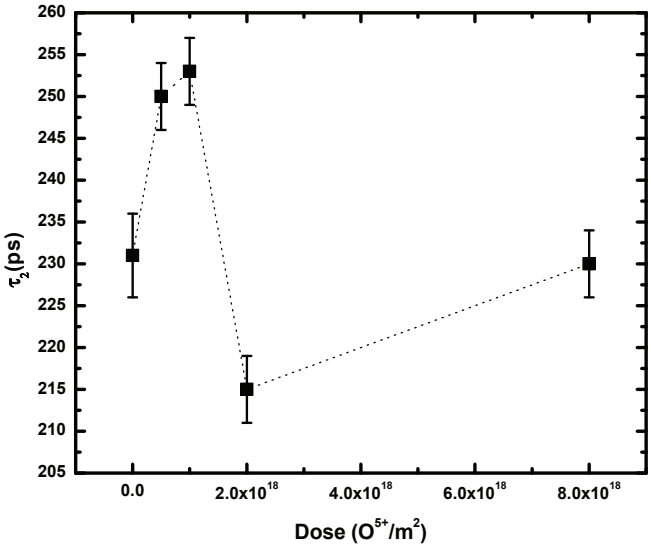

Figure 3.7: Variation of τ_2 with irradiation doses for the Zr1Nb samples.

Table 3.1: Values of τ_1, τ_2 and I_2 for the unirradiated and irradiated Zr1Nb samples.

Irradiation doses (O^{5+}/m^2)	τ_1 (ps)	τ_2 (ps)	I_2
Unirradiated	128±3	231±5	43.4±3.4
5×10^{17}	132±2	250±4	47.7±2.4
1×10^{18}	137±3	253±4	50.7±2.8
2×10^{18}	119±4	215±4	56.1±3.8
8×10^{18}	125±4	230±4	52.3±3.7

Table 3.2: Effective domain size, microstrain and dislocation density along different crystallographic planes for the unirradiated and irradiated Zr1Nb samples.

	Domain size (nm) Error=±2					Microstrain (10^{-3}) Error=$\pm10^{-5}$					Dislocation density ($10^{15}m^{-2}$) Error=$\pm5\times10^{13}$				
Dose (O^{5+}/m^2) $\longrightarrow$	Unirradiated	5×10^{17}	1×10^{18}	2×10^{18}	8×10^{18}	Unirradiated	5×10^{17}	1×10^{18}	2×10^{18}	8×10^{18}	Unirradiated	5×10^{17}	1×10^{18}	2×10^{18}	8×10^{18}
002	107	30	30	51	34	0.6	1.91	1.94	1.52	1.94	0.1	4.52	4.60	2.10	4.05
101	106	30	26	46	34	0.6	1.86	1.95	1.55	1.70	0.2	4.37	5.24	2.39	3.52
102	109	30	29	49	34	0.7	1.89	1.94	1.53	1.85	0.1	4.46	4.83	2.20	3.84
103	111	30	29	50	34	0.7	1.90	1.94	1.53	1.89	0.2	4.49	4.71	2.15	3.95
112	107	29	26	47	32	0.7	1.88	1.92	1.54	1.89	0.2	4.66	5.16	2.32	4.24

The estimated values of τ_2 for the irradiated samples indicates the presence of the mono and divacancies inside the samples except at a dose of 2×10^{18} O^{5+}/m^2, where the values is 215 ps. This low value of τ_2 at this specific dose of irradiation helps us to conclude that there are no dominant vacancies in the material at this dose. Hence this low value of τ_2 can be attributed solely to the presence of the dislocation loops [163]. The absence of vacancies and the lower value of dislocation density at this dose (Figure 3.6(c)) can be explained as follows. At the particular dose of irradiation, if the rate of annihilation of vacancies into the sink (dislocation loops) dominates over the rate of their creation, a situation may arise where all the vacancies that are created gets annihilated in the sinks lowering the sink density (dislocation density) itself. In our earlier studies of irradiation on Zr-1Sn-1Nb-0.1Fe [157, 158] by Ne^{6+} and O^{5+} energetic ions we did not observed this anomaly. The details of the PAS results have been shown in table 3.1.

The estimated values of effective domain size (D_e), microstrain and dislocation densities along different crystallographic planes have been shown in Table 3.2. In this case also, anomaly was observed in the values of effective domain size, microstrain and dislocation density at the dose of 2×10^{18}

O^{5+}/m^2. Moreover, for the cases of the unirradiated sample and the samples irradiated at doses of 1×10^{18} and 2×10^{18} O^{5+}/m^2, significant changes were observed in the values of effective domain size along different crystallographic direction. But when considering the samples irradiated at the doses of 5×10^{18} and 8×10^{18} O^{5+}/m^2, these values remained almost unchanged along different crystallographic directions. In order to get a clear picture about the shapes of the domains at different doses of irradiation, the projections of D_e on two mutually perpendicular crystallographic directions ($\langle200\rangle$ and $\langle002\rangle$) were estimated and plotted on a third plane containing both the directions (Figure 3.8). From Figure 3.8, it is clear that the shapes of the domains are almost isotropic for the samples

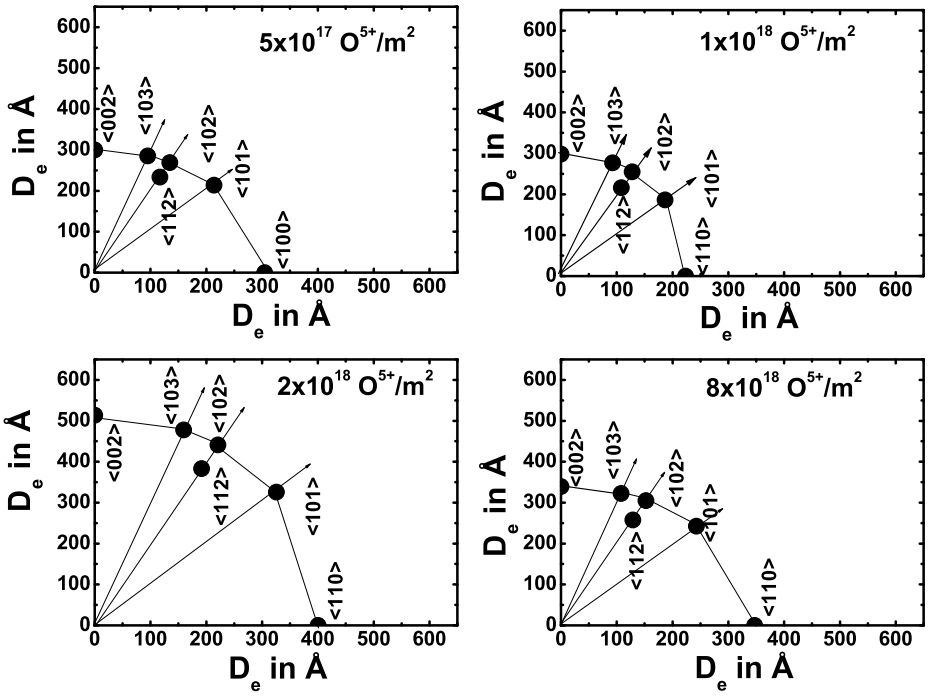

Figure 3.8: Projections of effective domain size on the plane containing the directions $\langle002\rangle$ and $\langle100\rangle$ (first quadrant) for Zr1Nb samples.

irradiated at doses of 5×10^{17} and 8×10^{18} O^{5+}/m^2. However, for the samples irradiated at doses of 1×10^{18} and 2×10^{18} O^{5+}/m^2, the domains are slightly anisotropic in shape, with larger values along $\langle002\rangle$ directions.

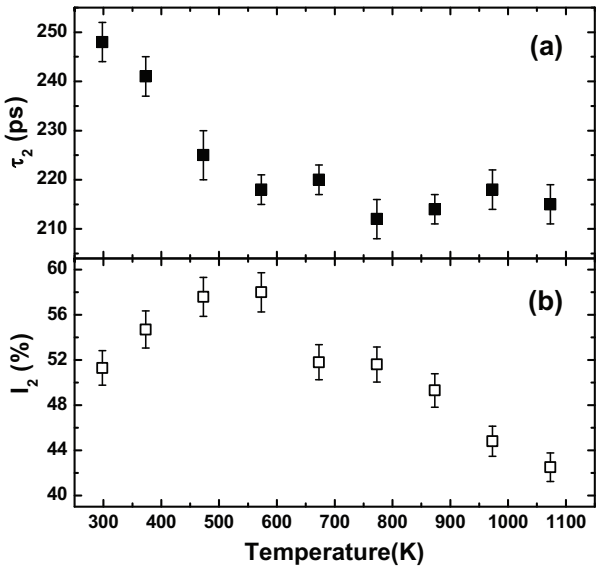

Figure 3.9: Variation of τ_2 and I_2 with isochronal annealing temperature for the Zr-1Nb sample irradiated at a dose of 1×10^{18} O^{5+}/m^2.

The isochronal annealing experiments following the PAS studies on the 1×10^{18} O^{5+}/m^2 sample reveals a drastic fall of τ_2 (Figure 3.9(a)) up to a temperature of 573K due to the annihilation of the vacancies. As observed in Figure 3.9(b), the initial increase in I_2 can be attributed to the increase in the concentration of mono-vacancies resulting from the dissociation of vacancy-impurity complexes. Upadhyaya et al. [164] have observed the dissociation of vacancy-impurity complexes in Zr-0.5Nb system around a temperature 523K. According to Cottrell [165], the following relation approximately describes the binding energy of a vacancy with a foreign atom which has a size misfit η with the matrix lattice:

$$E_b = 8\pi\mu r_0^3\eta^2 \tag{3.1}$$

where μ is the shear modulus of the matrix, r_0 is the matrix atom radius and $\eta = \pm\langle\frac{r_1-r_0}{r_0}\rangle$ where, r_1 is the impurity atom radius. Using Eq. 3.1, E_b for vacancy-niobium complexes in zirconium matrix is found to be around 0.08 eV which corresponds to a temperature around 619 K. This value approximately matches with the peak temperature observed in Figure 3.9(b).

3.6 Conclusion

XRDLPA have been used successfully to extract the microstructural parameters like the average domain size, microstrain and average dislocation density in the oxygen irradiated Zr-1Nb samples. Anomaly in the change of these microstructural parameters have been observed at some specific dose of irradiation, which proves that the irradiation induced microstructure in this alloy is very much dose dependent in the low dose regime. PAS results also reveal the same anomaly at that specific dose of irradiation. Isochronal annealing studies followed by the PAS experiments reveal the signature about the presence of vacancy solute atom complexes at the initial stages of annealing, which get dissociated at the higher annealing temperatures.

Chapter 4

Studies of Microstructural Imperfections of Powdered Zirconium Based alloys

4.1 Introduction

The dimensional changes of different zirconium based alloys under severe operating condition inside nuclear reactors are mainly governed by their initial microstructure of the α-phase. Even the mechanical properties of these materials are highly controlled by the α-phase texture and its dislocation structure. However, the presence of the second phase particles in the α-phase microstructure is also responsible in controlling the different important mechanical properties of these materials. These microstructural changes cause the significant change in the shape and breadth of the XRD peak during the X-ray Diffraction experiment. Hence, by applying suitable model based techniques, the XRD line profiles can successfully be analysed to extract the microstructural features inside the materials. There is a number of different theories developed to relate various dislocation distributions to the shape or breadth of an X-ray diffraction line [166, 167, 168, 169, 170, 171, 172]. In most of the cases, the broadening of XRD peaks due to microstructural changes in the samples comes from (1) the heterogeneous elastic strain distribution inside the sample which arises due to the presence of dislocations (microstrain); and (2) the finite size of the region bounded by dislocations from which the diffraction

is coherent (domain size). For heavily deformed Zr alloys with a random distribution of dislocations, i.e. no dislocation polygonization or pileup, it has been assumed in some treatments that the coherent diffracting domain size corresponds to the average distance between dislocations [173].

Among the different techniques to analyse the XRD line profiles to extract the microstructural features, the most common *ab-initio* tecnique is the Warren and Averbach [166] technique which has allready been successfully applied to determine the dislocation densities in deformed Zr and Zr-alloys [174, 175, 176]. In the case where all dislocations have the same Burgers vector, the conversion to dislocation density is achieved by the use of appropriate calibration factors, determined by direct measurements of the dislocation densities using transmission electron microscopy. However, this method posses a large degree of experimental error due to the complex nature of the dislocation structure (mixed screw and edge character), which are also not uniformly distributed throughout a given material. Moreover for heavily deformed samples, the overlapping of the highly strained regions impose a limitation in viewing the microstructure by TEM. On the contrary, the X-ray diffraction Line Profile Analysis (XRDLPA) evaluates the microstructural parameters in a statistical manner, averaged over a large volume ($10^9 \mu m^3$) [177], and the analysis is much easier, reliable and quick.

4.2 Objective of the present study

In the earlier observation [178], the detailed microstructural studies on lattice imperfections in heavily deformed Zircaloy-2, Zr-2.5Nb and Zr-1Nb-1Sn-0.1 Fe (trade name Zirlo) have been performed using Warren-Averbach Technique. The values of the average domain sizes estimated for all the alloys appeared to be smaller compared to that in pure Zr due to the presence of second phase (β-phase) and intermetallic particles. In our present study, the microstructural characterization on these heavily deformed powder samples of zirconium-based alloys has been carried out using Integral Breadth method by single peak analysis, Modified Rietveld Method based on whole powder pattern fitting technique and Double Voigt analysis.

4.3 Experimental

The alloy ingots of Zircaloy-2, Zr-2.5Nb and Zirlo were prepared by double vacuum arc melting followed by β-quenching. The ingots were hot extruded at 1073K and then air-cooled. The powders were obtained by careful hand filing of the homogenised alloy ingots. The flat diffractometer samples from these powders have been prepared by making briquettes in standard sample holders using solution of canada balsam in xylene as binder [179]. X-ray diffraction profiles have been recorded using a Bruker AXS D8 Advance Diffractometer using CuK_α radiation. All the diffraction profiles were obtained by varying 2θ from 25° to 100° with a step scan of 0.02° and a scan time of 0.5 sec/step. The diffraction profiles were corrected for the instrumental broadening using a silicon sample, which had large crystallites and was free from defects.

4.4 Method of analysis

The heavy deformation of the samples using the finely threaded jwellery files cause the introduction of a large number of dislocations inside the samples. The arrangement of dislocation inside the materials is significantly responsible for microstructural change of these materials. Generally, the line width of a XRD peak arises due to the instrumental width of the diffractometer, broadening due to the small cell or domain and microstrain within the domain. Hence, using the suitable model based techniques of XRDLPA, these microstructural features can be extracted successfully. The analysis of line shapes allows one to characterise the microstructure more thoroughly in terms of microstrain and average domain size. The Simplified Breadth Method using the Voigt function modelling for single peak analysis, the Modified Rietveld Method using whole powder pattern fitting technique and the double Voigt method have been adopted here in order to analyse the diffraction peaks of Zircaloy-2, Zirlo and Zr-2.5Nb. All these three techniques are based on the analysis of the shapes of the broadened diffraction profiles. In case of the Simplified Breadth Method, the individual peak

have been fitted by a Voigt function to extract the volume weighted average domain size (D_v) and the microstrain (ε) along the corresponding crystallographic direction. The Modified Rietveld Method has been used to fit all the diffraction peaks simultaneously with suitable weightage by a pseudo-Voigt (pV) function. The surface weighted average domain size (D_s), effective domain size (D_e) along different crystallographic directions and the average microstrain values within the domain were then evaluated. The double Voigt technique has been adopted to seperate the Cauchy and Gaussian part of both the size and strain component of the microstructural broadening, and the results have been used to estimate the values of D_s, D_v and $\langle \varepsilon^2(L) \rangle^{\frac{1}{2}}$.

Here it should be noted that,The maximum solubility of Nb in α-Zr is about 1.5 wt percentage [180] and the rest of the Nb occurs as the β-phase. So, in case of Zr-2.5Nb and Zirlo the volume fraction of the beta phase is very low. Moreover the β-phase is finely dispersed [181] throughout the matix in the alloys after annealing, and hence it can not be detected by Xray diffraction technique [180, 181]. Due to this reason, the analysis in each case was based on single phase α (h.c.p) only.

4.5 Results and discussion

The values of D_v and ε for heavily deformed powdered samples of Zircaloy-2, Zirlo and Zr-2.5Nb obtained by single peak analysis have been shown in Table 4.1. It can be observed that the values of D_v is lowest in case of all the XRD peaks for Zr-2.5Nb as compared to Zircaloy-2 and Zirlo. This observation can be explained as due the presence of Nb which restricts the grain growth, resulting in a finer average domain size for the presence of higher volume fraction of β-phase. The microstrain values did not vary significantly with the variation of compositions as observed in Table 4.1.

Figure 4.1 shows a typical Rietveld fit for the deformed Zirlo sample. The results obtained from the Modified Rietveld technique and the double Voigt technique has been given in Table 4.2 Table 4.3 respectively. Here the values of D_s obtained from the Modified Rietveld technique has been found to

Table 4.1: Values of D_v and ε for heavily deformed powdered samples of Zirlo, Zr-2.5Nb and Zircaloy-2 obtained by single peak analysis. The maximum errors in D_v and ε are ± 25 angstrom and $\pm 0.5 \times 10^3$, respectively.

Peak	Zirlo		Zr-2.5Nb		Zircaloy-2	
	D_v(angstrom)	ε(10^{-3})	D_v(angstrom)	ε(10^{-3})	D_v(angstrom)	ε(10^{-3})
(1,0,0)	151	4.98	210	3.53	265	3.42
(0,0,2)	431	5.99	249	3.56	257	2.7
(1,0,1)	225	5.33	183	4.36	312	4.25
(1,0,2)	-	-	151	4.31	160	6.11
(1,1,0)	384	4.98	98	1.34	169	2.47
(1,0,3)	184	3.62	102	1.61	120	6.06
(0,0,4)	288	3.79	87	1.98	147	1.43

be comparable with the results obtained by double Voigt technique. In case of Zirlo and Zr-2.5Nb, smaller values of the domain size have been observed for the presence of two phase structure i.e $\alpha+\beta$ in both of the alloys.

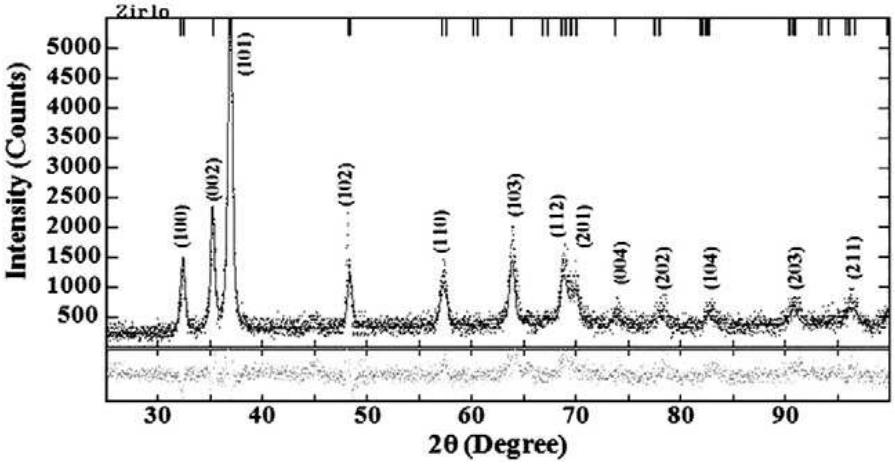

Figure 4.1: Typical Rietveld fit for deformed powdered Zirlo sample.

The similar observation has also been obtained in the earlier work [178]. However, since Zircaloy-2 is a single phase alloy, the domain sizes estimated for this alloy has shown larger values. During the

Table 4.2: Values of D_v and $\langle \varepsilon^2(L) \rangle^{\frac{1}{2}}$ for heavily deformed powdered samples of Zirlo, Zr-2.5Nb and Zircaloy-2 obtained by Modified Rietveld method

Sample	D_s(angstrom) maximum error= ± 12	$\langle \varepsilon^2(L) \rangle^{\frac{1}{2}}(10^{-3})$ maximum error= $\pm 5 \times 10^{-5}$	$\rho(10^{15}\mathrm{m}^{-2})$ maximum error= $\pm 5 \times 10^{13}$
Zirlo	103	1.17	8.09
Zr-2.5Nb	100	1.31	9.30
Zircaloy-2	168	1.51	6.38

Table 4.3: Values of D_s, D_v and $\langle \varepsilon^2(L) \rangle^{\frac{1}{2}}$ for heavily deformed powdered samples of Zirlo, Zr-2.5Nb and Zircaloy-2 obtained by Double Voigt method

Sample	β_{SC} (10^{-2})	β_{SG} (10^{-2})	β_{DC} (10^{-2})	β_{DG} (10^{-2})	D_s(angstrom) maximum error= ± 15	$\langle \varepsilon^2(L) \rangle^{\frac{1}{2}}(10^{-3})$ maximum error= $\pm 5 \times 10^{-5}$	D_v(angstrom) maximum error= ± 17
Zirlo	0.43	0.31	0.02	0.18	116	2.46	156
Zr-2.5Nb	0.42	-	-	0.32	117	3.38	233
Zircaloy-2	0.29	0.20	0.10	0.04	172	2.77	236

deformation of this alloy, the predominant slip occurs on the primary glide plane ((100) plane) and the dislocation form coplanar arrays. As the deformation proceeds furthur, the process of cross slip takes place and the multiplication process operates. By this process, the cold worked structure is formed which is made of high dislocation density regions in the form of tangled network or cells. Hence the characteristic microstructure of Zircaloy-2 in the heavily deformed state is a cellular substructure which results in due to the entanglement of dislocations. In this analysis also, the average microstrain ($\langle \varepsilon^2(L) \rangle^{\frac{1}{2}}$) values did not change significantly in these three alloys.

On the other hand, the microstructure of both Zr-2.5Nb and Zirlo contains fine distribution of the β-phase. Since the Nb enriched β-phase is softer than the α phase, the dislocations generated during deformation of this soft β phase form loops around the α phase. This process leads to the creation of cell structures or domains. This phenomenon takes place since the generation of dislocations retains the continuity between the two phases, which is necessary to avoid any void and micro-cracks during deformation.

In the Double-Voigt method, at least two reflections from the same family of crystallographic planes were considered for analysis. Here both the size and strain broadened profiles were approximated by a Voigt function and the Cauchy and Gaussian components of the size and strain broadened

profiles (β_{SC},β_{SG},β_{DC} and β_{DG}) were separated along $\langle 001 \rangle$ and listed in Table 4.3. From table 4.3, it can be observed that the size broadened profile contains both the Cauchy and Gaussian components of the integral breadth except for Zr-2.5Nb. The size brodening profile in case of Zr-2.5Nb is found to be Cauchy in nature whereas the strain broadened profile is Gaussian.The D_s values obtained from the Modified Rietveld method are found to be less in case of both Zirlo and Zr-2.5Nb. The variation of microstrain ($\langle \varepsilon^2(L) \rangle^{\frac{1}{2}}$) with the Fourier length L for the deformed powdered samples has been shown in Figure 4.2. The ε values for all the samples have been found similar. Figure 4.3 represents the

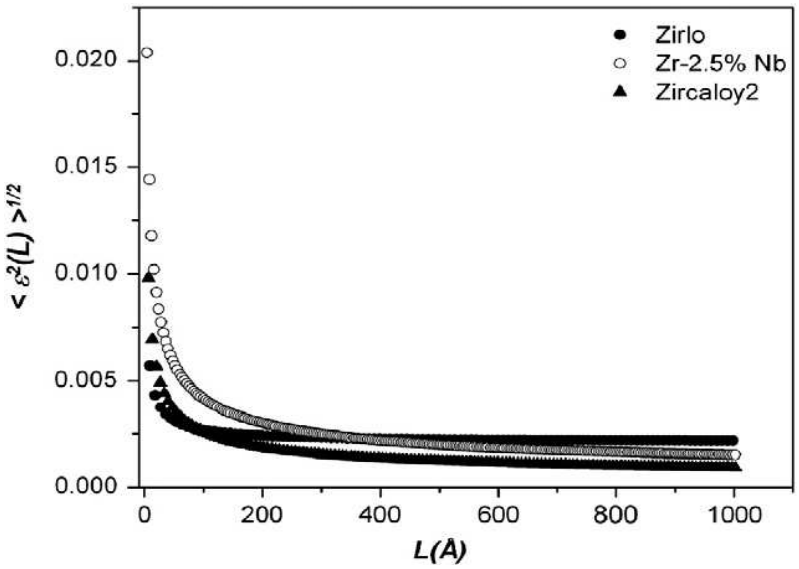

Figure 4.2: Variation of $\langle \varepsilon^2(L) \rangle^{\frac{1}{2}}$ with Fpurier length L for heavily deformed powdered samples of Zirlo, Zr-2.5Nb and Zircaloy-2 obtained by Double Voigt method.

volume weghted column length distribution function $P_v(L)$ with L. It has been observed from Figure 4.3 that the size distribution has been significantly narrowed down in case of zirlo.

The different model based techniques of XRDLPA used in the present study, are very popular and widely applied to many studies in the field of materials science. For extracting the different microstructural parameters, these techniques are complimentary to each other. However the single peak and the paraller peak analysis as done in the Simplified Breadth Method and in the Double Voigt

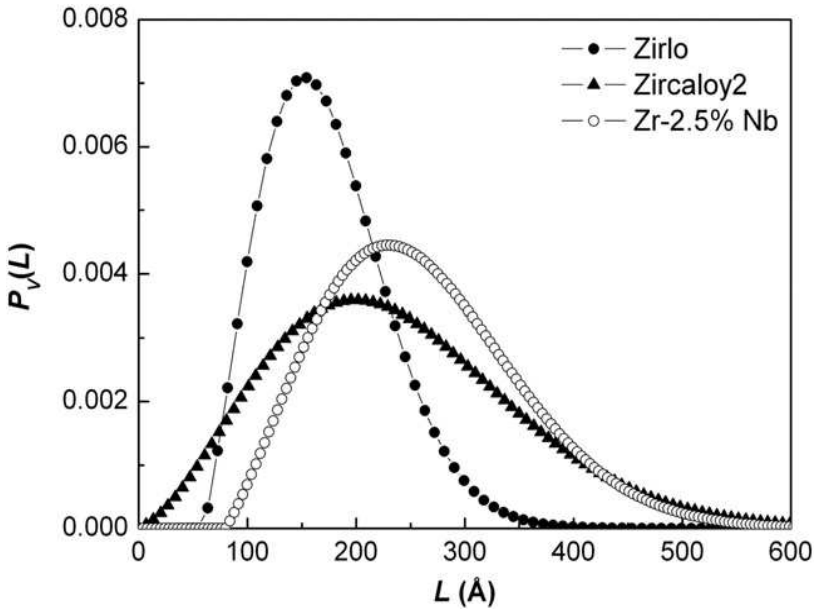

Figure 4.3: Volume weighted column length distribution function for heavily deformed powdered samples of Zirlo, Zr-2.5Nb and Zircaloy-2 obtained by Double Voigt method.

Technique, does not require any structural model and hence the analysis are much simpler in these cases.

This study helped us to understand the microstructure of different zirconium-based alloys under their heavily deformed condition, with the help of different model based techniques of XRDLPA. Among these techniques, the Simplified Breadth Method and the Double Voigt analysis gave information of the microstructure based on only the individual peak analysis. On the contrary, the Modified Rietveld Method gave quantitative information of the microstructural parameters considering all the diffraction peaks.

4.6 Conclusion

Different model based approaches of X-ray Diffraction Line Profile Analysis have been used to characterize the microstructure of the heavily deformed Zirconium-based alloys. These techniques are suitable as the analysis is much easier, reliable and quick and can be easily adopted in the shop floor

practice where characterisation of the average microstructural parameters are mandatory. These techniques help one to achieve the information of the microstructural parameters like cell size or domain size, dislocation density, microstrain within the domains, averaged over a volume of 10^9 μm^3.

Chapter 5

In-situ Studies of Evolution of the Microstructure with Temperature in Heavily Deformed Ti-modified Austenitic Stainless Steel by X-ray Diffraction Technique

5.1 Introduction

The deformation of solid polycrystalline materials causes generation of a large amount of dislocations inside the materials. Mutual interactions of these dislocations significantly controls the resulting microstructure of the deformed materials. However, besides the different microstructural alteration resulting from the dislocation dislocation interaction, the deformed microstructure also contains a complex feature like texture (grain orientation and grain rotation). Again the microstructural changes of these deformed materials during annealing involve not only the changes in the configurations of the dislocations, but at the same time the process also involves a change in the texture. Around the year of 1950, extensive works on the recovery of deformed materials during annealing has been reviewed by Beck [182], Bever [183] and Titchener and Bever [184]. After that, in spite of the growing interest on the search of quantitative physically-based models for the annealing process [185], the study of the evolution of the microstructural features during disentanglement of the dislocation network at the

earliest stage of annealing has not been addressed. This type of study can be performed only by XRD technique, after eliminating the effect of texture. This can be done using an aggregate of powder samples in heavily deformed state which contains a huge population of dislocations in the form of tangles, but completely looses the information of preferred orientation due to the randomization of the crystallographic orientation.

5.2 Review of the earlier studies

The process of annealing of the deformed materials can be devided into three different stages like recovery, recrystallization and grain growth. During the recovery of deformed materials, the microstructural changes occur in a smaller length scale, and hence can not be observed by optical micrography. However, recovery of deformed materials causes the partial restoration of their physical and mechanical properties. Hence the recovery process can be studied indirectly by measuring the changes in the different physical and mechanical properties of a deformed materials. Another important method to study the recovery is to measure the release of the stored energy of the deformed microstructure during its recovery.

There is a series of experiments performed by Clareborough and colleagues [186, 187, 188] in which they have studied the stored energy release in copper, nickel and aluminium during recovery. However, during the recent years after the development of high sensitivity Differential Scanning Calorimetries (DSC), the study of recovery from measuring the release of the stored energy became very much popular in the field of materials science. During 1990, Schmidt and Haessner [189] studied the recovery of deformed high purity aluminium at low temperature with the help of DSC. In this experiment, the material was deformed at 77K and maintained at that temperature until the DSC has been done. They have observed a small and a wide peak in the DSC curve around 203K along-with a large and a narrow peak around 253K. The wide peak was the signature of the recovery of the material where the narrow peak was observed due to the recrystallization.

The indirect ways to study the recovery of a deformed material involve the measurement of different mechanical and physical parameters like hardness, yield stress, resistivity etc. The kinetics of the recovery process is explained based on the rate of changes observed in these parameters during recovery [7]. Besides a large number of studies based on the kinetics of the recovery of single crystals deformed in single slip [190, 191, 192, 193, 194, 195, 196], there is also a good number of reported works on the studies of recovery kinetics of the deformed polycrystalline materials [197, 198, 199]. However, the interpretation of the different types of recovery kinetics require the understanding of the different physical processes which are taking place during recovery. According to Humphrey et al., there are three different mechanisms acting during the process of recovery: dislocation rearrangement, dislocation annihilation and subgrain growth [7]. Hence the study of recovery and it's interpretation from the view of dislocation interactions became a field of huge interest. In 1966, Li [200] studied the recovery in deformed copper and explained the recovery process as originating from the kinetics of dislocation dipole annihilation and showed that the rate of change of the dislocation density (ρ) is proportional to ρ^m, where m=2. The similar type of variation in dislocation density (with m=3) was also observed later on by Prinz. et al. [201] when the studies were performed on the deformed nickel.

However, in case of deformed polycrystals, the dislocation structure is much more complex and the recovery process is not controlled fully by the mechanism of dislocation dipole annihilation. In this case, the mechanism of dislocations movement become also an important factor in controlling the rate of recovery. Although under the application of sufficient thermal energy, the dislocation movement is significantly controlled by the climb process resulting in a faster rate of recovery, at moderate temperatures, the movement of dislocations is controlled simultaneously by the climb and glide mechanism which become a significant factor in controlling the rate of recovery [191, 202, 203].

The Stacking Fault Energy (SFE) of the material is an essential parameter which significantly controls the arrangement of the dislocation network under deformed condition. For materials with medium or high stacking fault energy, dislocations are arranged during deformation to form a three dimensional cell structure, with the cell walls made of the complex dislocation tangles. The sizes of

the cells depend upon the material's property and the amount of the deformation experienced by the material. During the initial process of recovery, the loosely tangled dislocations along the cell walls rearranges them to form low angle grain boundaries (subgrain boundaries). In case of the metals and alloys with low melting points, dynamic recovery takes place where the dislocations form the well defined subgrain structure during or after the deformation. In these cases, the recovery process involves mainly a coarsening of the subgrain structure. However the deformation of the materials with low stacking fault energies does not result in a well defined subgrain structure, rather the dislocations form loosely bound tangles inside the material. Recovery of these materials also does not result in the well defined subgrain formation because in these cases, recrystallization starts before the significant recovery can take place.

Hence, the most important microstructural evolution during recovery is the formation of subgrains from the cell structure, or from the loosely tangled dislocation networks which are formed during deformation. A number of TEM studies were performed during the years of 1960-1980 by Bailey and Hirsch [204], Carrington *et al*. [205], Hu [206], Lytton *et al*. [207] and Hasegawa and Kocks [208]. Besides the microstructural changes observed during this stage of recovery, significant changes in the mechanical properties of the materials were also reported by Lytton *et al*. [207] and Hasegawa and Kocks [208].

Besides the evidences of subgrain formation, there are also evidences of subgrain rotation during the last stages of recovery process where thin foils of few alloy systems were studied in-situ at High Voltage Transmission Electron Microscope [209]. Studies of subgrain growth in polycrystals have also been performed using the Molecular Dynamics simulation [210, 211].

There are a large number of reported theoretical and experimental studies which involve the kinetics of the subgrain growth during the recovery period of the annealing process. For most of the cases, the kinetics of the subgrain growth was found to follow the following equation:

$$D^n = D_0^n + Kt \tag{5.1}$$

where D is the subgrain size after a time t from the starting of recovery process. D_0 is the subgrain size at t=0 and K is a temperature dependent rate constant. Different recovery studies performed by Smith and Dillamore [212], Sandström et al. [213], Varma and Willits [214], Varma and Wesstrom [215] and Varma [216] revealed that the value of exponent n is close to 2. However, the larger values of n has also been reported in the the later investigations [217, 218, 219]. Studies on the kinetics of the subgrain growth during the recovery of single crystal deformed in plane strain condition, have been performed by Ferry and Humphreys [220] and Huang and Humphreys [221].

5.3 Objective of the present study

Though a large number of studies have been performed to study the kinetics of the subgrain growth during recovery of the deformed materials, the sizes of the subgrains in all these studies [212, 213, 214, 215, 216, 217, 218, 219] were found to vary within the range of 0.1 m to few microns. However, in the very early stages of microstructural evolution during annealing of heavily deformed materials, the length scales of the substructures are much less than these subgrains ($\approx$10nm). Humphrey et al. [7] emphasized that, it is difficult or rather impossible to understand the mechanism of the formation of the subgrains from the lowest length scale substructure, as the microstructural evolution during this stage cannot be observed in-situ. Moreover, in heavily deformed sample, the dislocation strain fields overlap due to the presence of high density dislocation tangles. This overlapped strain fields imposes a limitation to view the region by TEM during the earliest stage of annealing. On the contrary, since the X-Ray probes an average volume of $10^9 \mu m^3$ within the sample and the wavelength of the X-ray is comparable with the length scale of these substructures, the XRD can be a unique characterization tool to acquire the statistically averaged information from the spatially heterogeneous substructure of the deformed polycrystalline materials in situ during annealing. In this work, for the first time, XRD technique has been used to study the evolution of this lowest length scale substructure at the earliest stage of annealing. However, in case of pure metals or dilute alloys, the dynamical process rate of

the evolution of these substructures at the earliest stage of annealing is very fast and hence imposes a restriction to capture the data in short interval of times. Thus the evolution of the microstructure at this stage can be studied only if the kinetics can be slowed down by the addition of alloying elements. There are substantial evidences that the fine particle dispersion may exert strong pinning forces on the growth of subgrains [222, 223]. Because of this reason the present study has been performed on Ti-modifed austenitic stainless steel (D9), rich in alloying elements, which is an important core structural material for Prototype Fast Breeder Reactor [224], being built at Indira Gandhi Centre for Atomic Research (IGCAR), India. The material exhibits high resistance against the irradiation induced void swelling and creep phenomena, as well as an appreciable combination of high temperature tensile and creep strength properties [225, 226]. The powder samples have been obtained from the bulk annealed material by introducing severe deformation with the help of finely threaded jewelry file. The evolution of the lowest length scale substructure of this powdered sample has been studied in-situ using high temperature XRD technique, both with time and temperature. In the following text, these substructures will be referred to, as domain.

5.4 Experimental details

The alloy D9 was obtained in the form of rods of 30 mm diameter in the hot rolled condition. Rods of 26 mm diameter were machined from these hot rolled rods and given a solution annealing treatment at 1373K for $\frac{1}{2}$ h followed by water quenching.

The heavily deformed D9 powder was obtained from these annealed rods by careful hand filing using the finely threaded jewelry file. The powder particles come out by this method experience extreme shear deformation [227] possible in case of bulk samples and thus ensures the presence of high population of dislocations inside them. Fine particles in the size range of 74-88 μm were extracted from this D9 powder with the help of 170 and 200 mesh sieves.

The High Temperature X-ray Diffraction experiments were performed on these samples using the Bruker AXS D8 Advance Diffractometer with the Anton Paar high temperature attachment HTK 16. The attachment consisted of an electrically heated Platinum strip of dimension 100mm$\times$10mm$\times$1mm which acted as the sample stage as well as the heater. The two ends of the Pt strip were water cooled and maintained at the temperature of 293K (temperature of the water chiller). A Pt-Rh thermocouple was attached at the bottom middle of the strip and the temperature was controlled at the required level with the help of an Anton Paar HTK16 temperature controller.

A required amount of the severely deformed D9 sample was collected on a slide and then it was mixed with a few drops of isopropyl alcohol and a drop of Zapon^{TM} which acted as a binder. The mixture was then pasted uniformly on the Pt stage with the help of a spatula. An external metallic groove was used to maintain the uniformity in dimension and packing of the sample on the stage during mounting, which was taken out after mounting the sample. The whole stage was then isolated from the surroundings by a vacuum chamber which was connected to a turbo molecular pump to maintain a high vacuum inside the chamber. During the experiments, the vacuum inside the chamber was better than 5×10^{-5} mbar.

Two different types of high temperature XRD experiment were performed on these samples using the Co-Kα radiation. The first experiment deals with study of the kinetics of the microstructural evolution of heavily deformed D9 samples at different elevated temperatures 673K, 773K, 823K, 838K, 845K, 853K and 873K. As the kinetics of the microstructural evolution is a thermally assisted phenomenon and becomes fast at high temperature, thus to detect this evolution using XRD with a good precision, the study has been limited up to a temperature of 873K. In each case, the desired temperature was attained to the samples at a rate of 1.66 K/sec and then the X-ray scan was started. As the process of microstructural evolution is very fast, it is required to collect the information of the evolution in-situ at a close interval of time. However, the time required for a full profile scan was much larger (almost around 30 minutes with the scan step of 0.02° taken at 0.5 sec/step) and that's why the study was limited to the highest intensity peak (111) only which is also the slip plane of the

Ti-modified austenitic stainless steel. The scan was performed between 48° and 53.5° which required a minimum scan time of 222 seconds including the instrument adjustment time after optimizing different instrumental parameters for obtaining an acceptable peak to background ratio for the (111) peak. One hundred and forty five number of X-ray scans for (111) peak were collected successively within a time of 9 hours to understand the kinetics.

In the second experiment, the X-ray data was collected in situ at room temperature and subsequently at different elevated temperatures ranging from 323K to 873K. At each temperature, the scan range of 2θ was 26° to 122° with a step of 0.02° taken at 0.5 sec/step. Each sample was heated to the different pre-defined set temperatures followed by a soaking of 9 hours to stabilize its microstructural evolution before acquisition of the data. The experiment was performed several times to check the reliability and repeatability of the observed data.

TEM studies were carried out on the deformed and annealed (annealed at 873K for 9 hours) powder samples. In each case, a small quantity of the powder was suspended in acetone solution and the solution was sonicated for 7 hours. A drop of this solution was put onto the TEM grids and was allowed to dry and stored in a vacuum dessicator. The micrographs were obtained using a JEOL 200kV TEM at the unit of Nanoscience and Technology, IACS, Kolkata, India.

5.5 Method of analysis

The X-ray data obtained from different experiments have been analyzed using suitable model based techniques. The single peak analysis of the diffraction pattern of the (111) plane has been performed to characterize the in-situ time dependent evolution of the microstructure at different elevated temperatures. The true integral breadth (β) of each XRD (111) peak profile was evaluated after correcting for the Debye Waller factor at that particular temperature and also for the instrumental broadening contribution. This β was used to calculate the volume weighted average domain size (D_v) using the Scherrer's method. The microstructural variation with temperature has been studied by full powder

pattern fitting technique using the Modified Rietveld method on the diffraction profiles. Considering the isotropic model, the lattice parameter (a), surface weighted average domain size (D_s) and the average microstrain $\langle \varepsilon_L{}^2 \rangle^{\frac{1}{2}}$ were used simultaneously as the fitting parameters to obtain the best fit. Having obtained the values of D_s and $\langle \varepsilon_L{}^2 \rangle^{\frac{1}{2}}$, the average domain size and microstrain were further refined using anisotropic model to estimate the effective domain size (D_e) for each crystallographic plane.

5.6 Results and discussion

Figure 5.1 represents the variation of normalized integral breadth ($\frac{\beta}{\beta_0}$, β_0 being the initial values of the integral breadth at each temperature) with time at different elevated temperatures. From figure 5.1

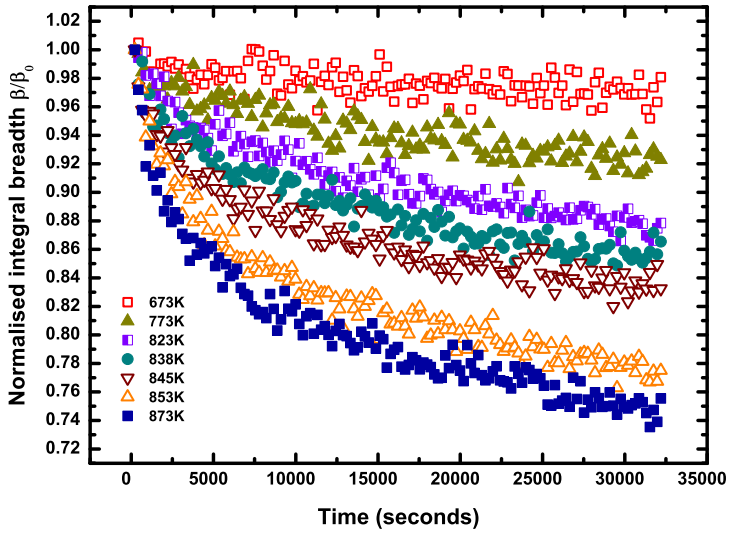

Figure 5.1: Variation of normalized integral breadth with time at different elevated temperatures.

it is observed that the normalized integral breadths with time become almost stationary at different temperatures after 9 hours. This happens due to the saturation in the microstructural evolution after that specified interval of time, and helps us to choose a definite soaking time of 9 hours for the second part of our experiment.

Figure 5.2 represents the XRD profiles of the samples at room temperature and at different elevated temperatures after soaking of 9 hours. The changes in the intensity patterns in this figure are

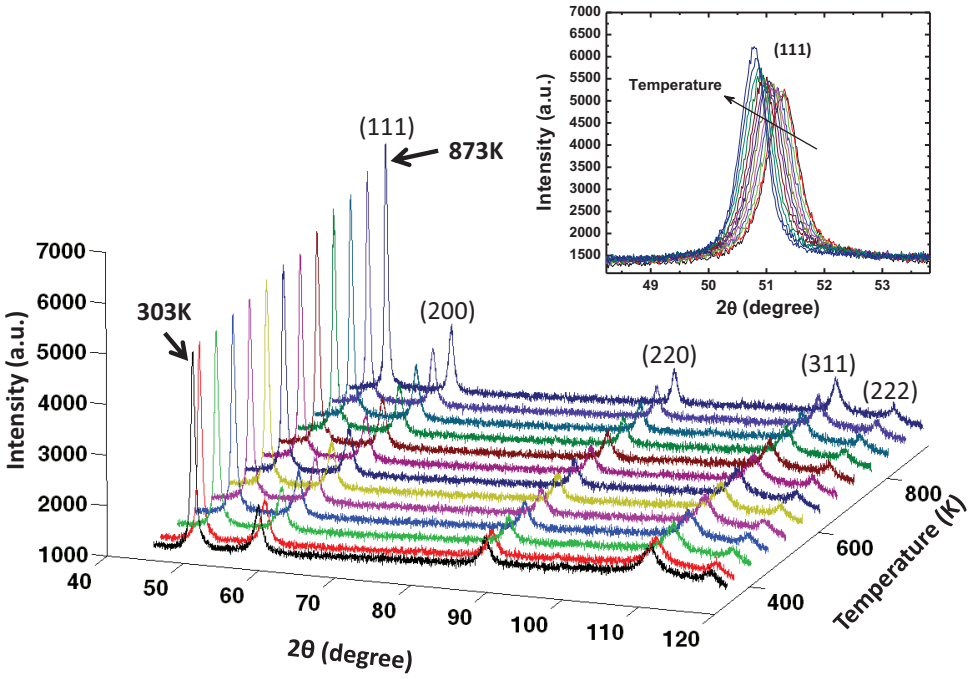

Figure 5.2: XRD profiles of the heavily deformed D9 powder samples at room temperature and at different elevated temperatures.

observed due to the microstructural changes in the samples due to change in the temperature. The inset of Figure 5.2 shows changes in the intensity of the (111) peak in an expanded scale.

The Rietveld fit of a typical XRD profile at a temperature of 823K has been shown in Figure 5.3. The variations of D_s and $\langle \varepsilon_L{}^2 \rangle^{\frac{1}{2}}$ of these samples are shown as a function of temperature in Figure 5.4 and Figure 5.5 respectively. Figure 5.4 reveals significant changes in the values of D_s with temperatures. The average domain size for the sample at room temperature was found to be around 14nm. A small increase in D_s is observed up to 673K followed by a steep rise, reaching to an average value of 29 nm at 873K. The formation of domains at room temperature and at high temperature mainly depends on two factors: i) the initial arrangement of dislocations in the deformed materials which was established during the process of deformation and ii) the mobility of dislocations by the climb and glide processes during annealing. Since the climb process is the thermally activated phenomenon,

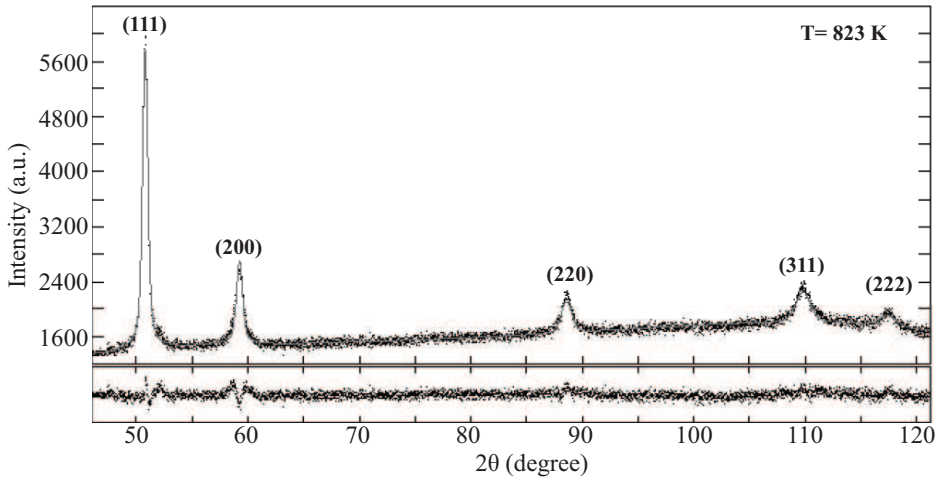

Figure 5.3: Rietveld fit of a typical XRD profile at a temperature of 823K.

this provides additional degrees of freedoms for the movement of dislocations at higher temperatures. Thus the probability of dislocation movements by climb increases with increase in temperature which in turn increases the probabilities of their rearrangements and annihilations. Hence, the steep increase in D_s after 673K can be attributed to the higher probability of dislocation rearrangement and annihilation at high temperature by the process of climb.

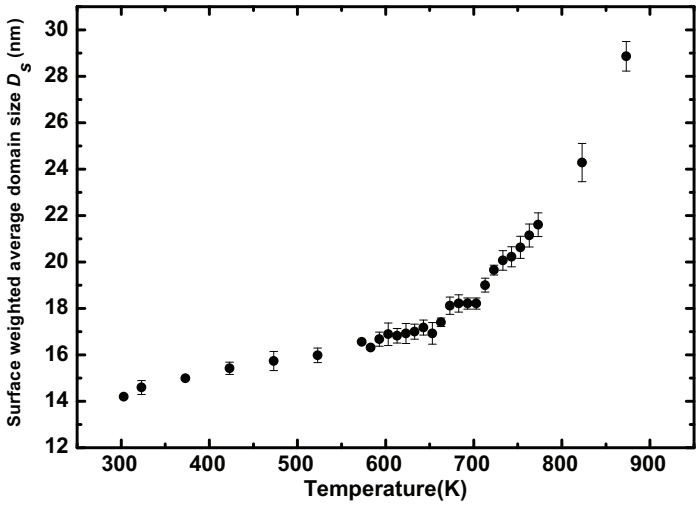

Figure 5.4: Variation of surface weighted domain size D_s for D9 powder samples as a function of temperature.

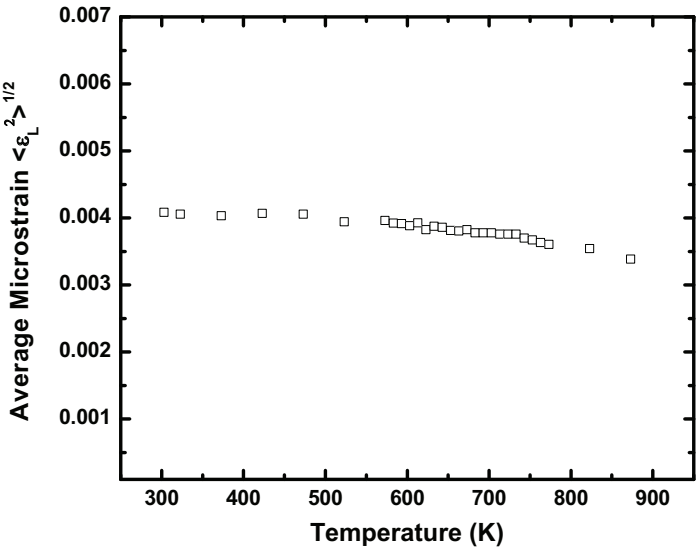

Figure 5.5: Variation of average microstrain $\langle {\varepsilon_L}^2 \rangle^{\frac{1}{2}}$ for D9 powder samples as a function of temperature.

The variation of effective domain size D_e with temperature along different crystallographic planes is represented in Figure 5.6. The value of D_e at different crystallographic planes shows strong anisotropy at all temperatures. The increase in D_e up to 673K may be attributed to the glide process only. Since the movement of dislocations by glide is more preferable in the crystallographic planes (111) and (220), a monotonic increase in D_e with temperature has been observed for those two crystallographic planes. On the other hand, the movement of dislocations by glide is restricted for the other two crystallographic planes, which gives rise to a non monotonic variation in D_e with temperature along (200) and (311). However at higher temperatures after 673K, the climb process gets activated which results in a smooth and steep increase in D_e with temperature, for all the crystallographic planes.

Figure 5.5 represents the variation of microstrain $\langle {\varepsilon_L}^2 \rangle^{\frac{1}{2}}$ with temperature. From the figure it is clear that the microstrain values did not change significantly even after the soaking of 9 hours at the highest temperature (873K). This observation is quite expected in case of D9 alloy which is rich in alloying elements. The high solute content of this alloy restricts the movement of dislocation [73], and thus prevents the microstrain to be relaxed even up to the temperature of 873K. Thus the

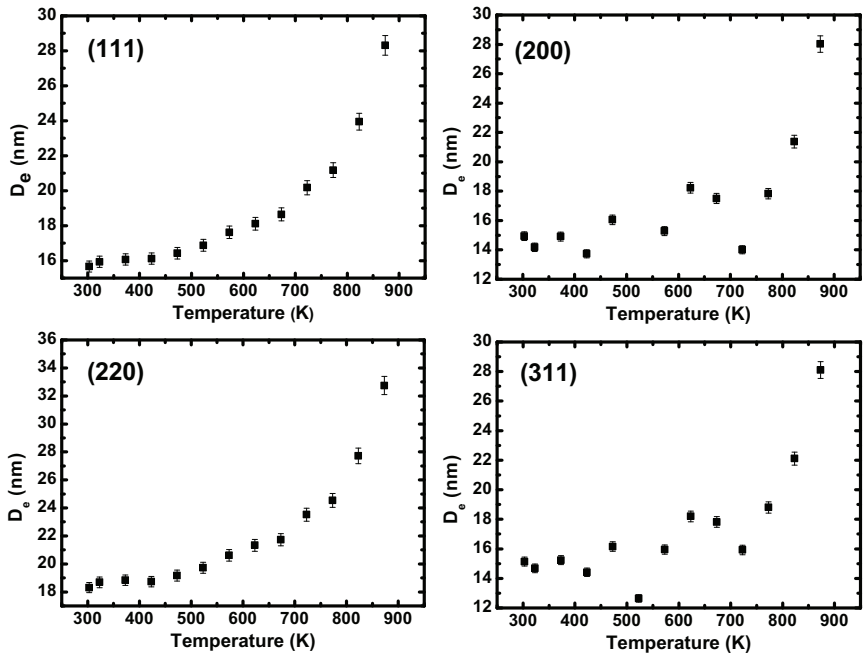

Figure 5.6: Variation of effective domain size D_e for D9 powder samples along different crystallographic planes.

variation in the XRD peak shape with temperature and time during the earliest stage of annealing can be considered as solely due to the variation in the domain size only. Hence in the next part of our discussion, it is considered that the variation in the XRD peak broadening with time and temperature has arisen solely due to the change in the finite domain size.

The variation of the normalised volume weighted domain size D_v (with respect to D_0 at each data set, where D_0 is the initial domain size) with time at different elevated temperatures is presented in Figure 5.7. From the figure it can be clearly observed that the growth rate of domains at the initial stage is significantly high as compared to the later stage. The huge amount of dislocations introduced inside the samples during deformation, are randomly arranged as loosely bound tangles all over the sample as shown in Figure 5.8(a). When a thermal energy is supplied to the sample, the dislocation mobility increases and the dislocations start rearranging (Figure5.8(b)) due to the mutual interactions among themselves. This rearrangement of the dislocations results in a decrease of the configurational entropy of the system. Consequently the internal energy is also lowered, which in effect reduces the total free energy (Helmholtz free energy) of the system. This overall dynamical process leads to

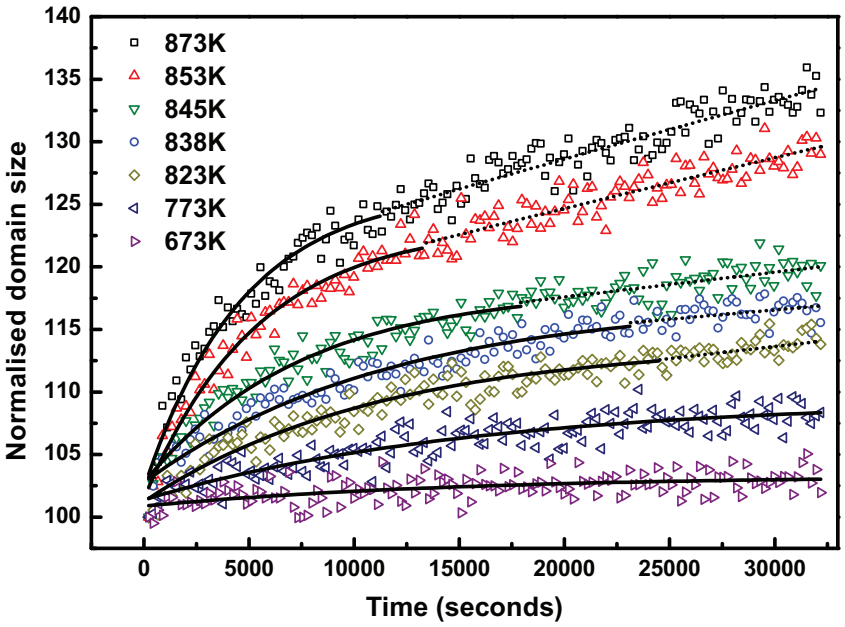

Figure 5.7: Evolution of normalized volume weighted domain size D_v with time at different temperatures for the D9 powder sample.The solid and the dotted lines represent the final fit of the experimental data using Eqs. 5.3 and 5.5 respectively.

the formation of domains as shown in Figure 5.8(c,d). During the formation of the domains through the mechanism of rearrangement of dislocations, the localized dislocation density becomes very high along the domain boundaries as compared with the interiors of the domains. Hence the probability of the annihilation of these dislocations becomes high along the domain boundaries, resulting in the growth of the domains as shown in Figure 5.8(e). Hence the evolution of the domain growth at the very early stages of recovery may be explained as to be governed by two distinct mechanisms. During the initial stage (stage I), the rearrangement of dislocations becomes the predominant mechanism which leads to the formation of the domains. At the later stage (stage II), the annihilation of dislocations at the domain boundaries become predominant, leading to the growth of the domains. The dynamics of domain rotation has not been considered here as it is well known that this mechanism plays significant role only at high temperature [7].

In the initial stage, the randomly arranged loosely bound dislocations present in the heavily deformed sample participate in the formation of domains by the process of rearrangement among

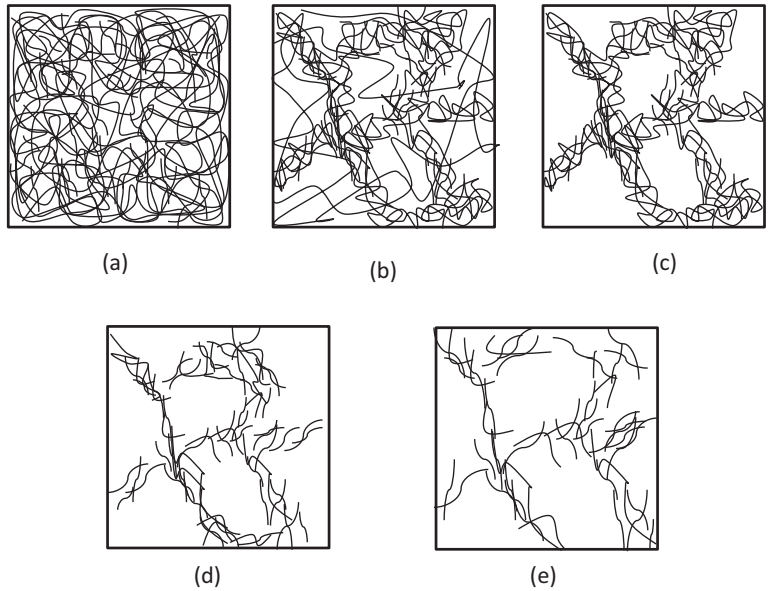

Figure 5.8: Schematic representation of the (a) randomly distributed dislocations in heavily deformed sample, (b) initial stage of dislocation rearrangement, (c) formation of domains with rearrangement of dislocation, (d) annihilation of dislocation and (e) growth of domains due to dislocation annihilation.

themselves. This process of rearrangement continues till a low angle tilt boundary with a high dislocation density is achieved and the formation of domain is almost complete. Hence we get a significantly high rate in the increase of domain size at stage I compared to stage II. After the formation of domain, the domain attains almost a fixed size surrounded by the highly entangled dislocations, which act as domain boundary. Due to the presence of these highly entangled dislocations, annihilation among the dislocations predominates at the domain boundaries and the domain boundary thickness decreases leading to the growth of the domain with a rate which is much slower than stage I.

During the initial stage (stage I), the dislocations starts rearranging themselves to attain the equilibrium condition (minimum energy configuration), and this process leads to the formation of domains. If we consider the rearrangement of dislocations as the sole mechanism to be responsible behind the growth of the domains, then after the equilibrium condition reached, the domain size certainly will reach at some maximum value (D_m). Now as the rearrangement process goes forward towards its equilibrium condition, the process rate gets slower. Hence, if we consider D_v as the

instantaneous domain size, then the rate of increase of D_v will be proportional to the difference ($D_m - D_v$), i.e.

$$\frac{dD_v}{dt} = k_1(D_m - D_v) \tag{5.2}$$

where k_1 is the rate constant. This leads to:

$$D_v(t) = D_m - (D_m - D_v|_{t=0})\exp(-\frac{t}{\tau}) \tag{5.3}$$

where $\tau = \frac{1}{k_1}$, which is the characteristic time of the dynamical process.

When a domain is formed, the dynamical process involved in stage II becomes predominant as the localised dislocation density takes a high value at the domain boundaries. Since, the average dislocation density per unit volume will be larger for smaller domains, the localisation of dislocations at the domain boundaries will be more in this case and hence the annihilation probability will also be higher, leading to a higher rate of domain growth. Hence the rate of domain growth in stage II can be mathematically modelled as:

$$\frac{dD_v}{dt} = \frac{k_2}{D_v^n} \tag{5.4}$$

where k_2 is the rate constant. This leads to the equation:

$$D_v^2 = D_0^2 + Bt \tag{5.5}$$

with $n = 1$. Here, D_0 is the initial average domain size of this process and B is a constant.

The variation of D_v as seen in Figure 5.7, has been modelled using the equations 5.3 and 5.5. The final fit of the experimental data using these two equations have been represented in the Figure 5.7 by the solid and dotted line respectively. Since the dislocation climb is a thermally activated process, it makes the movement of dislocations much easier at higher temperatures, thus facilitating the rearrangement and annihilation of the dislocations to take place much faster. This observation can be

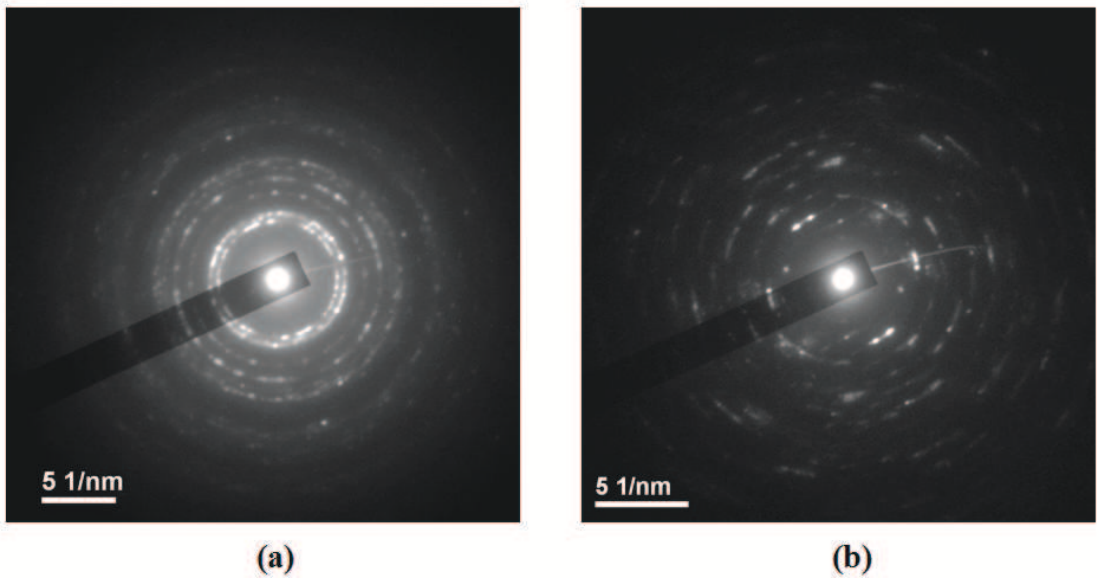

Figure 5.9: Selected Area Diffraction (SAD) patterns for (a) heavily deformed D9 powder sample, (b) sample after 9 h annealing at a temperature of 873 K.

seen clearly from Figure 5.7 where the first mechanism (rearrangement of dislocations) switches over to the second mechanism (annihilation of dislocation) at a lower time with the increase in temperature. However, it is interesting to note that, below 823K the data (at temperatures 673K and 773K) could be fitted with equation 5.3 only. This signifies that the rearrangement of dislocations is the sole mechanism behind this small increase of domain size. This observation helps us to conclude that below 823K, even if the annealing is done for a sufficiently long time, complete recovery would never be achieved in Ti- modified austenitic stainless steel.

TEM studies were carried out at room temperature on heavily deformed powder sample and on annealed sample at 873K for 9 hours. Figure 5.9(a) and 5.9(b) shows the Selected Area Diffraction

(SAD) pattern for the deformed and annealed samples respectively. The corresponding micrographs has been shown in Figure 5.10(a) and 5.10(b). The presence of highly strained regions are observed in Figure 5.10(a) which are formed due to the presence of high dislocation tangles throughout the matrix as expected in a heavily deformed structure. These highly strained regions could not be romoved significantly even after the annealing at 873K for 9 hrs, and is clearly seen in Figure 5.10(b). The

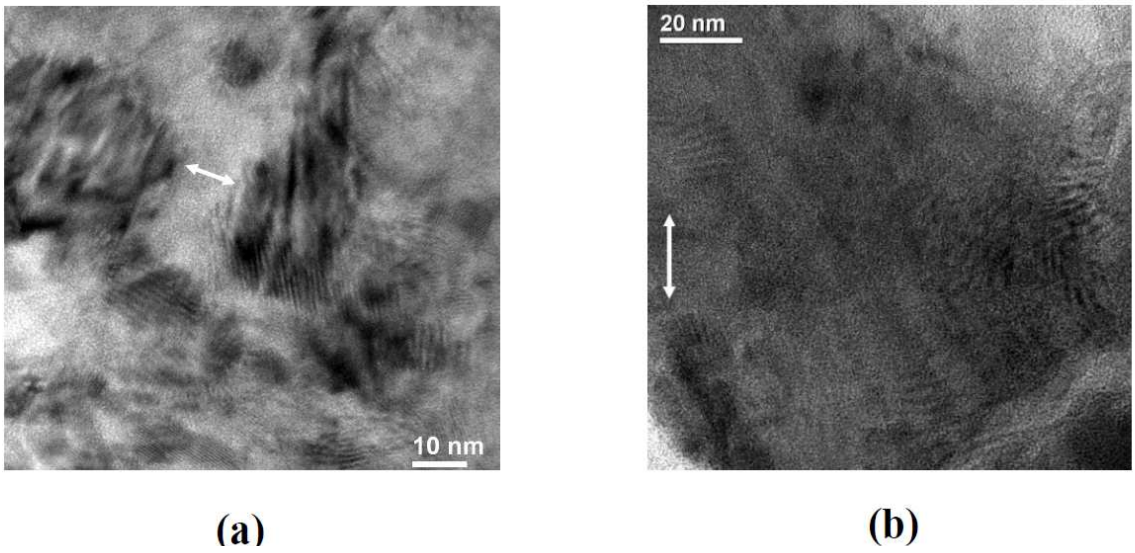

Figure 5.10: Transmission Electron Micrographs for (a) heavily deformed D9 powder sample, (b) sample after 9 h annealing at a temperature of 873 K.

spacing between the consecutive distorted regions was found to be of the order of 10nm for heavily deformed sample and 20nm for the annealed sample. These values correspond to the coherent region (domain) as detected by the XRD.

5.7 Conclusion

The high temperature XRD technique has been used successfully to study the microstructural evolution of the heavily deformed D9 powder samples during the earliest stages of annealing, both with time and temperature. The domain size was found to increase systematically with increase in tem-

perature. Two distinct mechanisms were found to be responsible in controlling the kinetics of the microstructural evolution at the earliest stage of recovery, one is the rearrangement of dislocations and another is their annihilation. The climb process becomes active at high temperature which finally governs the kinetics of both rearrangement and annihilation of the dislocations.

Chapter 6

Conclusions

In the present thesis, the microstructures of different nuclear structural materials have been studied using the XRD technique. The studies have been performed on different types of PHWR and FBR core structural materials under their deformed or irradiated conditions. In case of the Zr based alloys, the studies have been performed under heavily deformed and irradiated conditions. The heavily deformed powders of D9 alloy have been used to study the in-situ microstructural evolution during the early stages of annealing. Different model based techniques of XRDLPA have been used to analyze the XRD data obtained from the different samples. The microstructural information inside the different nuclear core structural materials could be extracted successfully using these model based techniques of XRDLPA.

The irradiation of Zr-1Nb alloy samples with 116 MeV O^{5+} ions caused significant changes in their microstructure. The XRD data obtained from these samples have been analysed successfully to extract the different microstructural parameters like domain size, microstrain and dislocation density. These microstructural parameters have been found to vary significantly with the variation of the irradiation doses. Anomaly was found in the values of these microstructural parameters at a specific dose of irradiation (2×10^{18} O^{5+}/m^2) which proved that the post irradiated microstructure of Zr-1Nb alloys are very much dose dependent in the low dose regime.

The microstructural information of different Zr-based alloys under their heavily deformed powdered condition have been extracted successfully using different model based techniques of XRDLPA. The methods were found to be complementary to each other. However among the different model based techniques of XRDLPA, the Modified Rietveld Technique is the most reliable technique as it is based on the whole pattern fitting method. The domain sizes were found to be smaller in case of the Zr-2.5Nb and Zirlo compared to that of Zircaloy-2. The presence of Nb enriched β-phase in α-Zr matrix of Zr-2.5Nb and Zirlo was found to be responsible in controlling the domain growth, resulting in a smaller domain size compared to that of Zircaloy-2.

Beside the successful application of the different model based techniques of XRDLPA to study the deformed and irradiated microstructure of diiferent reactor core structural materials, the techniques also have been used successfully to study the microstructural evolution of the heavily deformed D9 powder samples during the early stages of annealing, both with time and temperature. In this study, high temperature XRDLPA has been used successfully for the first time to know about the evolution of the lowest length scale dislocation substructures at the early stages of annealing. Systematic increase in the domain size have been observed with increase in the temperature. The kinetics of the microstructural evolution at the early stages of annealing was found to be controlled by two distinct mechanisms, one is the rearrangement of dislocations and another is their annihilation. The growth of these lowest length scale substructures during the early stages of annealing have been modeled successfully from the light of these two mechanisms. The climb process was found to become active at higher temperature which finally governed the kinetics of both rearrangement and annihilation of dislocations.

Bibliography

[1] Greenough G.B., (1952) Prog. Met. Phys., 3, 176.

[2] Warren B.E., (1959) Prog. Met. Phys., 8, 147.

[3] De M. and Sen Gupta S.P., (1984) Pramana, 23, 721.

[4] Allen S.M. and Thomas E.L., (1999) The Structure of Materials. Wiley, New York.

[5] McClintoc A. and Argon A.S., (1966) Mechanical Behaviour of Materials. Addison-Wesley, Reading, MA.

[6] Dieter G.E., (1988) Mechanical Metallurgy,McGraw-Hill Book Company Limited, London.

[7] Humphreys F.J. and Hatherly M., (2004) Recrystallization and Related Annealing Phenomena, Elseiver Ltd, Oxford.

[8] Was G.S., (2007) Fundamentals of Radiation Materials Science, Springer-Verlag, Berlin, Heidelberg, New York.

[9] Taylor G.I., (1934) Proc. Royal Soc., A145, 352.

[10] Orowan E., (1934) Z. Phys., 89, 605, 614, 635.

[11] Polanyi M., (1934) Z. Phys., 89, 660.

[12] Weertman Johannes and Weertman Julia R., (1992) Elementary Dislocation Theory, Oxford University Press, Oxford.

[13] Tomita Yoshiyuki and Okawa Takeyoshi, (1993) Mater. Sci. Eng. A, 172, 145.

[14] Hagiwara M. and Ch$\hat{e}$ne J., (1984) Scipta Metall., 18, 871.

[15] Cao H. and Wesse'n M., (2004) Metall. Mater. Trans. A, 35, 309.

[16] Tang Zhenghua and Stumpf Waldo, (2008) Mater. Sci. Eng. A, 490, 391.

[17] Hamzah E., Kanniaha M. and Harun M., (2008) Mater. Sci. Eng. A, 483, 555.

[18] Garner F.A., Henager C.H. and Igata N., (1988) Influence of radiation on material properties: 13th international symposium, ASTM STP 956.

[19] Garner F.A. and Perrin J.S., (1985) Volume II, ASTM STP 870.

[20] Moteff J., (1973) Effects of Radiation on Substructure and Mechanical Properties of Metals and Alloys, ASTM STP 529.

[21] Stachowicz Feliks, (1989) J. Mech. Working Tech., 19, 305.

[22] Khristenko I.N., Tomenko Yu.S. and Dryukova I.N., (1986) Strength of Materials, 18, 269.

[23] Wanga Zhiqiang, Zhong Yunbo, Lei Zuosheng, Ren Weili, Ren Zhongming and Deng Kang, (2009) Journal of Alloys and Compunds, 471, 172.

[24] Feng Yi, Zheng Haiwu, Zhu Zhengang and Zu Fangqiou, (2003) Mater. Chem. Phys., 78, 196.

[25] Semboshi Satoshi, Al-Kassab Talaat, Gemma Ryota and Kirchheim Reiner, (2009) Ultramicroscopy, 109, 593.

[26] Chang L.L., Shang E.F., Wang Y.N., Zhao X. and Qi M., (2009) Mater. Charac., 60, 487.

[27] Li Daquan, Wang Qudong and Ding Wenjiang, (2007) Mater. Sci. Eng. A, 448, 165.

[28] Reed-Hill R.E. and Abbaschian R., (1992) Physical Metallurgy Principles, 3rd Ed., PWS-Kent, Boston.

[29] Christian J.W. and Mahajan S., (1995) Prog. Mater. Sci., 39, 1.

[30] Hall E.O., (1954) Twining and Diffusionless Transformations in Metals, Butterworth and Co. Ltd., London.

[31] Cahn R.W., (1954) Adv. Phys., 3, 363.

[32] Hertzberg R.W., (1983) Deformation and Fracture Mechanics of Engineering Materials, 2nd Ed., John Wiley and Sons, New York.

[33] Bever M.B., Holt D.L. and Titchener A.L., (1973) Prog. Mater. Sci., 17, 5.

[34] Sevillano J.Gil, Houtte P. Van and Aernoudt E., (1980) Prog. Mater. Sci., 25, 135.

[35] Hirsch P.B., (1959) Internal Stresses and Fatigue in Metals, Elsevier, Amsterdam.

[36] Baley J.E. and Hirsch P.B., (1960) Philos. Mag., 5, 485.

[37] Baley J.E., (1960) Philos. Mag., 5, 833.

[38] Warrington D.H., (1960) Proc. Eur. Reg. Conf. on Electron Microscopy, Vol. I, p. 354, Delft.

[39] Embury J.D., Keh A.S. and Fisher R.M., (1966) Trans. AIME, 236, 1252.

[40] Hughes D.A. and Hansen N., (1997) Acta Mater., 45, 3871.

[41] Hansen N. and Juul Jensen D., (1999) Philosophical Transactions Of The Royal Society Of London Series A-Mathematical Physical And Engineering Sciences, 357, 1447.

[42] Hughes D.A., (2001) Mats. Sci. Eng. A, 319, 46.

[43] Korbel A., Embury J.D., Hatherly M., Martin P.L. and Erbsloh H.W., (1986) Acta Metall., 34, 1999.

[44] Hughes D.A., (1993) Acta Metall. Mater., 41, 1421.

[45] Drury M.D. and Humphreys F.J., (1986) Acta Metall., 34, 2259.

[46] Kuhlmann-Wilsdorf D., (1989) Materials Forum, 331-337, 689.

[47] Wassermann G. and Grewen J., (1962) Texturen Metallischer Werkstoffe, Springer-Verlag, Berlin.

[48] Dillamore I.L. and Roberts W.T., (1965) Met. Rev., 10, 271.

[49] Gittus J., (1978) Irradiation Effects in Crystalline Solids, Applied Science Publishers Ltd., London.

[50] Ullmaier H. and Schilling W., (1980) Radiation damage in metallic reactor materials, In: Physics of modern materials, Vol. I.IAEA, Vienna.

[51] Sizmann R., (1968) J. Nucl. Mater., 69, 386.

[52] Eyre B.L., (1974) Int. Met. Rev., 19, 240.

[53] Mitchell J.B., Logan C.N. and Echer C.J., (1973) J. Nucl. Mater., 48, 139.

[54] Mitchell J.B., Van Konynenburg R.A., Guinan M.W. and Echer C.J., (1975) Philos. Mag., 31, 919.

[55] Mitchell J.B., (1978) UCRL-52388. Livermore, Calif.: Lawrence Livermore Lab.

[56] Fleischer R.L., (1962) Acta Met., 10, 840.

[57] Higgy H.R. and Hammad F.H., (1975) J. Nucl. Mater., 55, 177.

[58] Mansur L.K., (1994) J. Nucl. Mater., 216, 97.

[59] Etoh Y., Shimada S., (1993) J. Nucl. Mater., 200, 59.

[60] Merle P., Loucif K., Adami L., Borrelly R., (1988) J. Nucl. Mater., 159,149.

[61] Griffiths M., (1988) J. Nucl. Mater., 159, 190.

[62] Eyre B.L., Matthews J.R., (1993) J. Nucl. Mater., 205, 1.

[63] Pecheur D., Lefebvre F., Motta A.T., Lemignan C., Charquet D., (1993) J. Nucl. Mater., 205, 445.

[64] Lee Y.S., Huang K.Y., Huang C.Y., Kai J.J., Hsieh W.F., (1993) J. Nucl. Mater., 205, 476.

[65] Cann C.D., So C.B., Styles R.C., Coleman C.E., (1993) J. Nucl. Mater., 205, 267.

[66] Stiegler J.O. and Mansur L.K., (1979) Ann. Rev. Mater. Sci., 9, 405.

[67] Kiritani M., (1994) J. Nucl. Mater., 216, 220.

[68] Vladimirov P. and Bouffard S., (2008) C. R. Physique, 9, 303.

[69] Savart F., (1829) Chim. Phys., 41, 61.

[70] Percy J., (1864) Metallurgy - Iron and Steel, London.

[71] Kalischer S., (1881) Ber. 14, 2747.

[72] Sorby H.C., (1887) J. Iron Steel Inst., 31.1, 253.

[73] Verlinden B., Driver J., Samajdar I. and Doherty R.D. (2007) Thermo-Mechanical Processing of Metallic Materials, Elsevier, Amsterdam.

[74] Carpenter H.C.H. and Elam C.F., (1920) J. Inst. Metall., 24(2), 83.

[75] Altherthum H., (1922) Z. Metall., 14, 417.

[76] Ewing J.A. and Rosenhain W., (1900) Phil. Trans. Royal Soc., 193A, 353.

[77] Humfrey J.C.W, (1902) Phil. Trans. Royal Soc., 200, 225.

[78] Clareborough L.M., Hargreaves M.E. and Loretto M.H., (1963) in Recovery and Recrystallization of metals, ed. Himmel, Interscience, 43.

[79] Barioz C., Brechet Y., Legresy J.M., Cheynet M.C., Courbon J., Guyot P. and Ratnaud G.M., (1992) Proc. 3rd Int. Conf. on Aluminium, Trondheim., 347.

[80] Perryman E.C.W., (1955) Trans. Aime., 203, 1053.

[81] Leslie W.C., Michalak J.T. and Aul F.W., (1963) in Iron and its Dilute Solid Solutions. ed. Spencer and Werner. Interscience, New York, 119.

[82] Masing G. and Raffelsieper J., (1950) Z. Metallk. 41, 65.

[83] Michalak J.T. and Paxton H.W., (1961) Trans. Metall. Soc. A.I.M.E., 221, 850.

[84] Haase O. and Schimd E., (1925) J. Phys., 33, 413.

[85] Drourd R., Washburn J. and Parker E.R., (1953) Trans. Metall. Soc. A.I.M.E., 197, 1226.

[86] Scherrer P., (1918) Nachr. Gött., 2, 98.

[87] Stokes A.R. and Wilson A.J.C., (1944) Proc. Phys. Soc. London, 56, 174.

[88] Wilson A.J.C., (1942) Proc. Royal Soc., A180, 277.

[89] Warren B.E., Averbach B.L., (1950) J. Appl. Phys., 21, 595.

[90] Warren B.E., Averbach B.L., (1952) J. Appl. Phys., 23, 497.

[91] Bertaut E.F., (1950) Acta Cryst., 3, 14.

[92] Barret C.S., (1950) Trans. AIME., 188, 123.

[93] Paterson M.S., (1952) J. Appl. Phys., 23, 805.

[94] Warren B.E., (1959) Prog. Met. Phys., 8, 147.

[95] Rietveld H.M., (1967) Acta Cryst., 22, 151.

[96] Douglass D.L., (1971) The Metallurgy of Zirconium, Atomic Energy Review Supplement, International Atomic Energy Agency, Vienna.

[97] Banerjee S. and Kamath H.S., (2005) Sixteenth Annual Conference of Indian Nuclear Society, Mumbai, India.

[98] Carpenter G.J.C., Northwood D.O., (1975) J. Nucl. Mater., 56, 260.

[99] Alexander W.K., Fidleris V., Holt R.A., (1977) ASTM STP 633, 344.

[100] Holt R.A., (1980) J. Nucl. Mater., 90, 193.

[101] Demin N.A. and Konobeev Yu. V., (1980) Atomic Energy, 48, 22.

[102] Scherrer P., (1918) Nachr. Gott., 2, 98.

[103] de Keijser ThH, Langford J.I., Mittemeijer E.J. and Vogels A.B.P., (1982) J Appl Cryst, 15, 308.

[104] Langford J.I., (1978) J Appl Cryst, 11, 10.

[105] Balzar D. and Ledbetter H., (1993) J Appl Cryst, 26, 9.

[106] Selivanov V.N. and Smislov E.F., (1991) Zavod Lab, 57, 28.

[107] Williamson G.K. and Hall W.H., (1953) Acta Metall, 1, 22.

[108] Lutterotti L. and Scardi P., (1990) J Appl Cryst, 23, 246.

[109] Rietveld H.M., (1967) Acta Cryst, 22, 151.

[110] Rietveld H.M., (1969) J Appl Cryst, 2, 65.

[111] Frevel L.K., (1987) Powder Diffr, 2, 237.

[112] Parrish W., Huang T.C. and Ayers G.L., (1976) Trans Amer Cryst Assoc, 12, 55.

[113] Cox D.E., Toby B.H. and Eddy M.M., (1988) Austral. J.Phys., 41, 117.

[114] Caglioti G., Paoletti A. and Ricci F.P., (1958) Nucl. Instrum. Methods., 35, 223.

[115] Nandi R.K. and Sen Gupta S.P., (1978) J Appl Cryst, 11, 6.

[116] Kielkopf J.F., (1973) J. Opt. Soc. Am., 63, 987.

[117] Dollase W.A., (1986) J Appl Cryst, 19, 267.

[118] Will G., Belloto M., Parrish W. and Hatr M., (1988) J Appl Cryst, 21, 182.

[119] Young A.R and Wiles B.D, (1982) J Appl Cryst, 15, 430.

[120] Will G., Parrish W. and Huang T.C., (1983) J Appl Cryst, 16, 611.

[121] Dollase W.A. and Reeder R.J., (1986) Am. Mineral, 71, 163.

[122] Pesonen A., (1979) J Appl Cryst, 12, 460.

[123] Paakkari T., Blomberg M., Serimaa R. and Jarvinen M., (1988) J Appl Cryst, 21, 393.

[124] Langford J.I., (1987) Prog. Cryst. Growth and Charact., 14. 185.

[125] Toraya H., (1995) The Rietveld Method, (ed) R A Young (Oxford: IUCr/OUP) Chap 14, p. 254.

[126] Langford J.I. and Louer D., (1996) Rep. Prog. Phys., 59, 131.

[127] Taupin D., (1973) J Appl Cryst, 6, 266.

[128] Langford J.I., (1980) Accuracy in Powder Diffraction, S Block and C R Hubbard (eds.) NBS Spec. Pub. No. 457 (Gaithersburg MA: US Dept of Commerce), p.255.

[129] Enzo S., Fagherazzi G., Benedetti A. and Polizzi S., (1988) J Appl Cryst, 21, 536.

[130] Benedetti A., Fagherazzi G., Enzo S. and Battagliarin M., (1988) J Appl Cryst, 21, 543.

[131] Scardi P., Kothari D.C. and Guzman L., (1991) Thin Solid Films, 195, 213.

[132] Scardi P., Lutterotti L. and Di Maggio R., (1991) Powder Diffr., 6, 20.

[133] Langford J. I., (1992) Accuracy in Powder Diffraction II, E Prince and J K Stalick (eds.), NIST Spec. Pub. No. 846 (Gaithersburg MA: US Dept of Commerce), p.110.

[134] Balzar D., (1992) J Appl Cryst, 25, 559.

[135] Balzar D. and Ledbetter H., (1993) J Appl Cryst, 26, 97.

[136] Balzar D. and Ledbetter H., (1995) Adv. X-ray Anal., 38, 397.

[137] Shee S. K., Pradhan S. K. and De M., (1998) J. Alloy and Comp., 265, 249.

[138] Wilson A.J.C., (1952) Acta. Cryst., 5, 318.

[139] Wilkens M., (1970) Fundamental Aspects of Dislocation Theory, NBS Special Publication No. 317 II, J. A. Simmons, R. de Wit, and R. Bullough, (eds.), Washington DC; US Department of Commerce, 1195.

[140] Wilkens M., (1979) J. Appl. Cryst., 12, 119.

[141] Ungar T., Mughrabi H., Ronnpagel D. and Wilkens M., (1984) Acta. Met., 32, 333.

[142] Kuzel Jr. R. and Klimanek P., (1989) J. Appl. Cryst., 22, 299.

[143] Groma I., Ungar, T. and Wilkens, M., (1988) J. Appl. Cryst., 21, 47.

[144] Petersen K., Ivans J.H. and Cotterell R.M.J., (1975) Phil. Mag., 32, 427.

[145] Seeger A., (1973) J. Phys. F: Metal Phys., 3, 248.

[146] Puska M.J., Makinen S., Mannien M. and Nieminen R.M., (1989) Phys. Rev., B39, 7666.

[147] Siegel R.W., (1980) Ann. Rev. Mater. Sci., 10, 393

[148] Siegel R.W., (1982) Advanced Techniques for Characterizing Microstructures, Wiffen F.W., Spitznagel J.A., (eds.), p. 413.

[149] Kirkegaard P., Eldrup M., Mogensen O.E. and Pedersen N.J., (1981) Comput. Phys. Commun., 23, 307.

[150] Puska M.J. and Nieminen R.M., (1983) J. Phys. F: Metal Phys., 13, 333.

[151] Sabol G., Klip G.R., Balfour M.G. and Roberts E, (1989) Zirconium in nuclear industry, Eighth international Symposium, ASTM STP 227, 1023.

[152] Sabol G.P., Schoenberger G. and Balfour M.G., (1991) IAEA Tech. Comm. Meeting on Materials for Advanced Water-Cooled Reactors, Plzen, Czech and Slovak Federal Republic, 50.

[153] Nikulina A.V., Markelov V.A., Peregud M.M., Voevodin V.N., Panchenko V.L. and Kobylyansky G.P., (1996) J. Nucl. Mater., 238, 205.

[154] Mukherjee P., Nambissan P.M.G., Sen Pintu, Barat P. and Bandyopadhyay S.K., (1999) J. Nucl. Mater., 273, 338.

[155] Biersack J.P. and Haggmark L.G., (1980) Nucl. Instrum. and Meth., 174, 257, The Stopping and Range of Ions in Matter (SRIM 2000) software developed by Ziegler J. and Biersack J.P. is available on the Website http://www.research.ibm.com/ionbeams.

[156] Abromeit C., (1994) J. Nucl. Mater., 216, 78.

[157] Sarkar A., Mukherjee P. and Barat P., (2008) J. Nucl Mater., 372, 285.

[158] Mukherjee P., Barat P., Bandyopadhyay S.K., Sen P., Chottopadhyay S.K., Chatterjee S.K. and Mitra M.K., (2002) J. Nucl. Mater., 305, 169.

[159] Mukherjee P., Sarkar A. and Barat P., (2005) Mater. Char., 55, 412.

[160] Mukherjee P., Nambissan P.M.G., Sen Pintu, Barat P. and Bandyopadhyay S.K., (1999) J. Nucl. Mater., 273, 338.

[161] Mukherjee P., Nambissan P.M.G., Barat P., Sen P., Bandyopadhyay S.K., Chakravartty S.K., Wadekar S.L., Banerjee S., Chottopadhyay S.K., Chatterjee S.K. and Mitra M.K., (2001) J. Nucl. Mater., 297, 341.

[162] Robles J.M. Campillo, Ogando E. and Plazaola F., (2007) J. Phys. Condens. Matter, 19, 176222.

[163] Hatakeyama M., Toyama T., Yang J., Nagai Y., Hasegawa M., Ohkubo T., Eldrup M. and Singh B.N., (2009) J. Nucl. Mater., 386, 852.

[164] Upadhyaya D.D. and Muraleedharan R.V., (1987) Bull. Mater. Sci., 9, 235.

[165] Cottrell A.H., (1967) An introduction to metallurgy, London, Edward Arnold.

[166] Warren B.E., Averbach B.L., (1950) J Appl Phys, 21, 595.

[167] Warren B.E., (1969) X-ray diffraction. Reading (MA): Addision-Wesley, p. 251.

[168] Ungár T., Mughrabi H., Rönnpagel D., Wilkens M.,(1984) Acta Metall, 32, 333.

[169] Groma I., Ungár T., Wilkens M. (1988) J Appl Cryst, 21, 47.

[170] Groma I., Ungár T., Wilkens M. (1989) J Appl Cryst, 22, 26.

[171] Groma I. (1998) Phys Rev B, 57, 7535.

[172] Ungár T., Révész A., Borbély A. (1998) J Appl Cryst, 31, 554.

[173] Aqua E.N., Owens C.M., (1967) Trans TMS-AIME, 239, 155.

[174] Kuzel R., Kilmanek P., (1988) J Appl Cryst, 21, 59.

[175] Kuzel R., Kilmanek P., (1988) J Appl Cryst, 21, 363.

[176] Kuzel R., Kilmanek P., (1989) J Appl Cryst, 22, 299.

[177] Mukherjee P., Sarkar A.,Barat P.,Bandyopadhyay S.K., Sen Pintu, Chattopadhyay S.K. et al., (2004) Acta Mater., 52, 5687.

[178] Mukherjee P., Chattopadhyay S.K., Chatterjee S.K., Meikap A.K., Barat P., Bandyopadhyay S.K., (2000) Metall and Mat Trans A, 31A, 2405.

[179] Chatterjee S.K., Halder S.K., Sengupta S.P., (1976) J Appl Phys, 47, 411.

[180] Aldridge S.A., Cheadle B.A., (1972) J Nucl Mater, 42, 32.

[181] Holt R.A., (1976) J Nucl Mater, 59, 234.

[182] Beck P.A., (1954) Adv. Phys., 3, 245.

[183] Bever M.B., (1957) Creep and Recovery, ASM, Cleveland, 14.

[184] Titchener A.L, Bever M.B., (1958) Prog. Met. Phys., 7, 247.

[185] Nes E., (1995) Acta Metall. Mater., 43, 2189.

[186] Clareborough L.M., Hargreaves M.E. and West G.W., (1955) Proc. R. Soc. Lond., A232, 252.

[187] Clareborough L.M., Hargreaves M.E. and West G.W., (1956) Phil. Mag., 1, 528.

[188] Clareborough L.M., Hargreaves M.E. and Loretto M.H., (1963) in Recovery and Recrystallization in Metals, ed. Himmel, Interscience, 43.

[189] Schimdt J. and Haessner F., (1990) Z. f. Phys. B. Condensed Matter., 81, 215.

[190] Drouard R., Washburn J. and Parker E.R., (1953) Trans. Metall. Soc. A.I.M.E., 197, 1226.

[191] Cottrell A.H. and Ayetkin V., (1950) J. Inst. Metals., 77, 389.

[192] Kuhlmann D.,Masing G. and Raffelsiefer J., (1949) Z. Metallk., 40, 241.

[193] Masing G. and Raffelsieper J., (1950) Z. Metallk., 41, 65.

[194] Hirsh P.B. and Humphreys F.J., (1969) in Physics of Strength and Plasticity, ed. A. Argon, MIT Press, 189.

[195] Gould D., Hirsh P.B. and Humphreys F.J., (1974) Phil. Mag., 30, 1353.

[196] Stewart A.T. and Martin J.W., (1975) Acta Metall., 23, 1.

[197] Humphreys F.J. and Hirsh P.B., (1976) Phil. Mag., 34, 373.

[198] Michalak J.D. and Paxton H.W., (1961) Trans. Metall. Soc. A.I.M.E., 221, 850.

[199] Van Drunen G. and Saimoto S., (1971) Acta Metall., 19, 213.

[200] Li J.C.M., (1966) in Recrystallization, Grain Growth and Textures. ASM, Ohio, 45.

[201] Prinz F., Argon A.S. and Moffa W.C., (1982) Acta Metall., 30, 821.

[202] Kuhlmann, (1948) Z. Fur. Phys., 124, 468.

[203] Friedel J., (1964) Dislocations, Addison-Wesley, London.

[204] Bailey J.E. and Hirsch P.B., (1960) Phil. Mag., 5, 485.

[205] Carrington W., Hale K.F. and McLean D., (1960) Proc. Royal. Soc. Lond., 259A, 303.

[206] Hu H., (1962) Tans. Metall. Soc. A.I.M.E., 224, 75.

[207] Lytton J.L., Westmacott K.H. and Potter L.C., (1965) Trans. Metall. Soc. A.I.M.E., 233, 1757.

[208] Hasegawa T. and Kocks U.F., (1979) Acta Metall., 27, 1705.

[209] Humphreys F.J. and Chan H.M., (1996) Mater. Sci. Technol., 12, 143.

[210] Moldovan D., Wolf D., Phillpot S.R. and Haslam A.J., (2002) Acta Mater., 50, 3397.

[211] Haslam A.J., Phillpot S.R., Wolf D., Moldovan D. and Gleiter H., (2001) Mater. Sci. Eng. A, 318, 293.

[212] Smith C.J.E. and Dillamore I.L., (1970) Met. Sci., 4, 161.

[213] Sandström R., Lehtinen E., Hedman B., Groza I. and Karlson J., (1978) J. Mater. Sci., 13, 1229.

[214] Varma S.K. and Willets B.L., (1984) Metall. Trans. A, 15, 1502.

[215] Varma S.K. and Wesstrom B.C., (1988) J. Mater. Sci. Lett., 7, 1092.

[216] Varma S.K., (1986) Mater. Sci. Eng., 82, L19.

[217] Furu T., Nes E., (1992) in: Fuentes, Sevillano (Eds.), Growth Rates of Recrystallized Grains in Highly Deformed Commercial Purity Aluminium, an Experimental and Modelling Study, Recrystallization92, San Sebastian, Spain,, pp. 311.

[218] Beck P.A., Ricketts B.G. and Kelly A.,(1959) Trans. Metall. Soc. A.I.M.E. 180, 160.

[219] Humphreys A.O. and Humphreys F.J., (1994) Proc. 4th Int Conf. on Aluminium, Atlanta, 1, 211.

[220] Ferry M. and Humphreys F.J., (1996) Acta Mater., 44, 1293.

[221] Huang Y. and Humphreys F.J., (2000) Acta Mater., 48, 2017.

[222] Humphreys F.J. and Martin J.W., (1968) Philos. Mag., 17, 365.

[223] Sandström R., (1977) Acta Metall., 25, 905.

[224] Selection of materials for PFBR nuclear steam supply system componentstechnical note: PFBR-MDG-2002-01, Kalpakkam.

[225] Latha S., Mathews M.D., Parameswaran P., Bhanu Sankara Rao K. and Mannan S.L., (2008) Int. J. Press. Vessels Pip., 85, 866.

[226] David C., Panigrahi B.K., Balaji S., Balamurugan A.K., Nair K.G.M., Amarendra G., Sundar C.S. and Raj Baldev, (2008) J. Nucl. Mater., 383, 132.

[227] Ghosh J., Mukherjee P., Chattopadhayay S.K., Chatterjee S.K., Meikap A.K. and Barat P, (2004) Met. Mater. Trans. A, 35A, 3319.

LIST OF PUBLICATIONS

1. **Studies of Microstructural Imperfections of powdered Zirconium Based alloys:** P.S. Chowdhury, A.Sarkar, P. Mukherjee, N. Gayathri, M. Bhattacharya, P. Barat. **Materials Characterization 61 (2010) 1061–1065.**

2. **In situ studies of evolution of microstructure with temperature in heavily deformed Ti-modified austenitic stainless steel by X-ray Diffraction technique:** P.S. Chowdhury, N. Gayathri, P. Mukherjee, M. Bhattacharya, A. Chatterjee, A Dutta, P. Barat. **Materials Science and Engineering A 528 (2011) 967–972.**

3. **Post irradiated microstructural characterization of Zr-1Nb alloy by X-ray diffraction technique and positron annihilation spectroscopy:** P.S.Chowdhury, P.Mukherjee, N.Gayathri, M.Bhattacharya, A.Chatterjee, P.Barat, P.M.G Nambissan. **Bulletin of Materials Science 34 (2011) 507-513.**

Reprints

MATERIALS CHARACTERIZATION 61 (2010) 1061–1065

available at www.sciencedirect.com

ScienceDirect

www.elsevier.com/locate/matchar

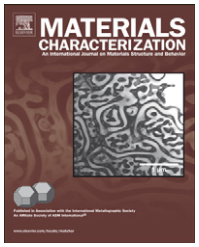

Studies of microstructural imperfections of powdered Zirconium-based alloys

P.S. Chowdhury[a], A. Sarkar[b], P. Mukherjee[a,*], N. Gayathri[a], M. Bhattacharya[a], P. Barat[a]

[a] Variable Energy Cyclotron Centre, 1/AF Bidhannagar, Kolkata-700 064, India
[b] Mechanical Metallurgy Section, Bhabha Atomic Research Centre, Mumbai-400085, India

ARTICLE DATA

Article history:
Received 24 March 2010
Received in revised form
21 June 2010
Accepted 26 June 2010

Keywords:
X-ray diffraction
Microstructure
Deformed Zirconium alloys

ABSTRACT

Different model based approaches of X-ray diffraction line profile analysis have been applied on the heavily deformed zirconium-based alloys in the powdered form to characterize the microstructural parameters like domain size, microstrain and dislocation density. In characterizing the microstructure of the material, these methods are complimentary to each other. Though the parameters obtained by different techniques are differently defined and thus not necessarily comparable, the values of domain size and microstrain obtained from the different techniques show similar trends.

1. Introduction

Zirconium alloys are used in Pressurized Heavy Water Reactors and undergo dimensional changes during service which are largely dependent on the initial microstructure of the alpha phase, which constitutes over 90% of the material volume. The mechanical properties of Zr-based alloys components in reactor are largely controlled by the alpha phase texture and its dislocation structure. The determination of bulk dislocation densities in metals is typically undertaken by analysis of X-ray diffraction lines for various diffracting planes. A number of different theories have been developed to relate various dislocation distributions to the shape or breadth of an X-ray diffraction line [1–7]. In most cases, the two main contributions of dislocation to line broadening are (1) the non-uniform elastic strain distribution arising from the presence of dislocations, usually referred to as microstrain; and (2) the finite size of the region bounded by dislocations from which the diffraction is coherent, usually referred to as domain size. The size contribution comes from the mean separation of dislocations and the contribution is inversely proportional to the dislocation density. On the other hand microstrain arises from the internal stress fields due to the presence of dislocations [8]. For heavily deformed Zr alloys with a random distribution of dislocations, i.e., no dislocation polygonization or pileup, it has been assumed in some treatments that the coherent diffracting domain size corresponds to the average distance between dislocations [9].

One method commonly used to separate the strain and domain size components of the broadening is that given by Warren and Averbach [1]. This method has been adopted for the determination of dislocation densities in deformed Zr and Zr alloys [10–12]. In the case where all dislocations have the same Burgers vector, the conversion to dislocation density is achieved by the use of appropriate calibration factors, determined by direct measurements of dislocation densities using transmission electron microscopy. This method in itself is subject to a large degree of experimental error, primarily because dislocation structures are complex (mixed screw and edge character) and are also not uniformly distributed throughout a given material. Moreover, the sample preparation for Transmission Electron Microscope (TEM) is highly time consuming and may

* *Corresponding author*. Tel.: +91 33 2318 4460; fax: +91 33 2334 6871.
E-mail address: paramita@vecc.gov.in (P. Mukherjee).

1044-5803/$ – see front matter © 2010 Elsevier Inc. All rights reserved.
doi:10.1016/j.matchar.2010.06.019

cause some changes in the defect structure during sectioning and polishing. The technique is also not suitable for characterizing the heavily deformed materials as the strain fields generated due to the presence of the dislocations overlap. On the contrary, the X-ray diffraction Line Profile Analysis (XRDLPA) evaluates the microstructural parameters in a statistical manner, averaged over a volume of 10^9 μm^3 [13]. Moreover, the analysis is much easier, reliable and quick and the specimen preparation requires very little time.

In our earlier observation [14], we have carried out detailed microstructural studies on lattice imperfections in heavily deformed Zircaloy-2, Zr-2.5 wt.% Nb and Zr–1Nb–1Sn–0.1 Fe (trade name Zirlo) using Warren–Averbach Technique. In all these alloys, the average domain size appeared to be smaller compared to that in pure Zr due to the presence of second phase (β-phase) and intermetallic particles. Microstrain values were found to be more in case of Zircaloy-2 and Zr–1Nb–1Sn–0.1 Fe as compared to pure Zr.

In the present study, we have carried out microstructural characterization using Integral Breadth method from single peak analysis, Modified Rietveld Method based on whole powder pattern fitting technique and double Voigt analysis on these heavily deformed powder samples of zirconium-based alloys. Although the Warren–Averbach technique is model independent and it is possible to obtain much more information such as column length distribution function, the behaviour of strain as a function of the averaging distance in domains etc., the method has serious drawbacks. Zr-based alloys with high symmetry and almost no overlapping peaks could provide information on microstructual parameters quite accurately using the Warren–Averbach technique as observed in our earlier studies [14]. In this work, we have tried to see the feasibility of the model based approaches on line profile analysis of these alloys.

2. Experimental Procedure

The alloy ingots were prepared by double vacuum arc melting followed by β-quenching. The ingots were hot extruded at 1073 K and then air-cooled. A small piece of sample was cut from the alloy ingots and annealed at 1023 K for 5 h. The powders were obtained by careful hand filing of this annealed sample. The flat diffractometer samples from these powders have been prepared by making briquettes in standard sample holders using solution of Canada balsam in xylene as binder [15]. X-ray diffraction profiles have been recorded using a Bruker AXS D8 advance diffractometer using CuK_α radiation. All the diffraction profiles were obtained by varying 2θ from 25° to 100° with a step scan of 0.02° and a scan time of 0.5 s/step. The diffraction profiles were corrected for the instrumental broadening using a silicon sample, which had large crystallites and was free from defects.

3. Method of Analysis

Diffraction of radiation on matter corresponds to a Fourier transform from real space to momentum space; hence the X-ray diffraction pattern of a sample represents a complete mapping of its structure and microstructure in the momentum space which is often called reciprocal lattice in periodic structure. In most investigations, the structural information is extracted from the diffraction pattern namely the angular positions and intensities of the Bragg peaks. Here, however, we are interested in the microstructure. Generally, the line width of a Bragg peak is due to the instrumental width of the diffractometer, broadening due to the small cell or domain and microstrain within the domain. The analysis of line shapes allows one to characterize the microstructure more thoroughly in terms of microstrain and average domain size. The Simplified Breadth Method using the Voigt function modelling for single peak analysis, the Modified Rietveld Method using whole powder pattern fitting technique and the double Voigt method have been adopted here in order to analyze the diffraction peaks of Zircaloy-2 and Zr-2.5 wt.% Nb. All these three techniques are based on the analysis of the shapes of the broadened diffraction profiles. For the Simplified Breadth Method, we have fitted the individual peak by a Voigt function to find out the volume weighted average domain size (D_v) and the microstrain (ε). In the Modified Rietveld Method, all the diffraction peaks were fitted simultaneously with suitable weightage by a pseudo-Voigt (pV) function. The surface weighted average domain size (D_s), effective domain size (D_e) along different crystallographic directions and the average microstrain values $\left\langle \varepsilon_L^2 \right\rangle^{\frac{1}{2}}$ within the domain were then evaluated.

In this connection, it is worth mentioning that the β-phase (b.c.c) which is present in Zr-2.5 wt.% Nb alloys could not be detected by X-ray diffraction. It is well known that the maximum solubility of Nb in α-Zr is about 1.5 wt.% [16] and the rest of the Nb occurs remains in the β-phase. As the annealing was carried out at 1023 K for 5 h, decomposition of β phase occurs as fine discrete particles at the α grain boundaries [17]. This β phase is homogeneously distributed as fine particles throughout the matrix and the size of the β particle is much lower than the detectable limit of the X-ray diffractometer [16,17]. So, the analysis in each case was based on single phase α (h.c.p) only.

3.1. *Simplified Breadth Method*

In this method [18], each diffraction peak is fitted by a Voigt function if the shape factor ϕ (defined by FWHM/Integral breadth) of the peak is in between 0.63 and 0.94, where FWHM is Full Width at Half Maximum. Here, the Cauchy component of the Voigt function is entirely attributed to the domain size while the Gaussian component is attributed to the microstrain. The relation between D_v (volume weighted domain size), ε (upper value of the microstrain), β_c and β_G is given by Langford [19].

$$D_v = \frac{\lambda}{\beta_c \cos\theta} \tag{1}$$

and

$$\varepsilon = \frac{\beta_G}{\tan\theta} \tag{2}$$

where β_c and β_G represent the Cauchy and the Gauss component of the integral breadth respectively.

3.2. Modified Rietveld Method

In this method, the diffraction profiles have been modelled by a pseudo-Voigt (*pV*) function which is a linear combination of a Cauchy and a Gaussian function. The program LS1 [20] used for this purpose includes the simultaneous refinement of the crystal structure and the microstructural parameters like the domain size and the microstrain within the domain. The method involves the Fourier analysis of the broadened peaks. An isotropic model was assumed and the lattice parameters, surface weighted average domain size (D_s) and the average microstrain $\langle \varepsilon_L^2 \rangle^{\frac{1}{2}}$ were used simultaneously as the fitting parameters to obtain the best fit. The dislocation densities ρ have been measured from the relation [21] $\rho = \sqrt{\rho_D \rho_S}$, where $\rho_D = 3/D_S^2$ (dislocation density due to domain size) and $\rho_S = k\langle \varepsilon_L^2 \rangle / \bar{b}^2$(dislocation density due to strain), k is a material constant and $\bar{b}$ is the modulus of Burger's vector, $\frac{1}{3}[11\bar{2}0]$.

3.3. Double Voigt Technique

Cauchy or Gaussian function exclusively cannot model the peak broadening. Therefore, the size and strain effects are approximated by a Voigt function [22], which is a convolution of a Cauchy and a Gaussian function. The equivalent analytical expressions for Warren–Averbach size–strain separation [1] are then obtained. The Fourier coefficients $F(L)$ in terms of a distance, L, perpendicular to the diffracting planes is obtained by Fourier transform of the Voigt function [22] and can be written as

$$F(L) = \left(-2L\beta_C - \pi L^2 \beta_G^2\right) \tag{3}$$

where, β_C and β_G are respectively the Cauchy and Gauss components of total integral breadth β. β_C and β_G can be written as:

$$\beta_C = \beta_{SC} + \beta_{DC} \tag{4}$$

$$\beta_G^2 = \beta_{SG}^2 + \beta_{DG}^2 \tag{5}$$

where, β_{SC} and β_{DC} are the Cauchy components of size and strain integral breadth respectively and β_{SG} and β_{DG} are the corresponding Gaussian components.

The size and distortion coefficients are obtained considering at least two reflections from the same family of crystallographic planes. The surface weighted average domain size D_S and strain $\langle \varepsilon^2(L) \rangle^{\frac{1}{2}}$ are given by the equations:

$$D_S = 1 / 2\beta_{SC} \tag{6}$$

$$\langle \varepsilon^2(L) \rangle = \left[\beta_{DG}^2 / (2\pi) + \beta_{DC} / (\pi^2 L)\right] / S^2 \quad \text{where } S = \frac{2\sin\theta}{\lambda} \tag{7}$$

The volume weighted domain size [18] is given by: $D_V = \frac{1}{\beta_S}$ where $\beta_S = \frac{\beta\cos\theta}{\lambda}$, integral breadth in the units of S, $(\text{Å})^{-1}$.

The volume weighted column length distribution functions are given by:

$$P_v(L) \propto L \frac{d^2 A_S(L)}{dL^2} \tag{8}$$

Table 1 – Values of D_V and ε for heavily deformed powdered samples of Zirlo, Zr-2.5 wt.% Nb and Zircaloy-2 obtained by single peak analysis. The maximum errors in $D_V$and ε are ±25 Å and $\pm 0.5 \times 10^{-3}$, respectively.

Peak	Zirlo		Zr-2.5 wt.% Nb		Zircaloy 2	
	D_v (Å)	ε (10^{-3})	D_v (Å)	ε (10^{-3})	D_v (Å)	ε (10^{-3})
(1,0,0)	151	4.98	210	3.53	265	3.42
(0,0,2)	431	5.99	249	3.56	257	2.7
(1,0,1)	225	5.33	183	4.36	312	4.25
(1,0,2)	–	–	151	4.31	160	6.11
(1,1,0)	384	4.98	98	1.34	169	2.47
(1,0,3)	184	3.62	102	1.61	120	6.06
(0,0,4)	288	3.79	87	1.98	147	1.43

For a size-broadened profile, the size coefficient is given as:

$$A_S(L) = exp(-2L\beta_{SC} - \pi L^2 \beta_{SG}^2) \tag{9}$$

From Eq. (8), we get,

$$\frac{d^2 A_S(L)}{dL^2} = \left[\left(2\pi L\beta_{SG}^2 + 2\beta_{SC}\right)^2 - 2\pi\beta_{SG}^2\right] A_S(L) \tag{10}$$

Selivanov and Smislov [23] showed that Eq. (10) is a satisfactory approximation of size distribution functions.

4. Results and Discussions

Table 1 shows the values of D_v and ε for heavily deformed powdered samples of Zircaloy-2, Zirlo and Zr-2.5 wt.% Nb obtained by single peak analysis. The domain size (D_v) obtained from individual peak is found to be lowest in case of Zr-2.5 wt.% Nb as compared to both Zircaloy-2 and Zirlo in majority of the peaks. This is due to the fact that the Nb restricts the grain growth and as a result the average domain size becomes finer for the presence of higher volume fraction of β-phase. The microstrain values did not vary significantly with the variation of compositions as observed in Table 1.

Fig. 1 shows a typical Rietveld fit for the deformed Zirlo sample. Table 2 gives the results obtained from the Modified Rietveld technique. It is seen that the values of D_S are comparable with the results obtained by double Voigt technique (Table 3). The domain size is smaller for the presence of two phase structure i.e., $\alpha+\beta$ in both Zirlo and Zr-2.5 wt.% Nb. The similar observation has also been

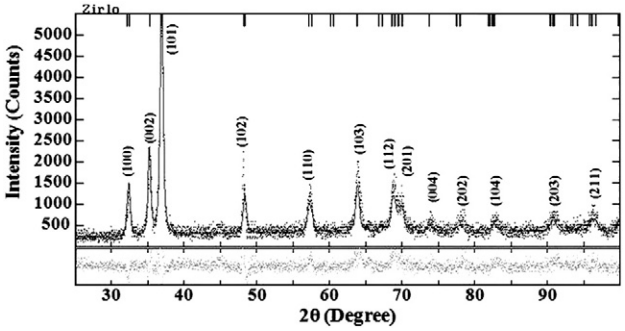

Fig. 1 – Typical Rietveld fit for deformed powdered Zirlo sample.

Table 2 – Values of D_s $\langle \varepsilon_L^2 \rangle^{\frac{1}{2}}$ and ρ for heavily deformed powdered samples of Zirlo, Zr-2.5 wt.% Nb and Zircaloy-2 obtained by Modified Rietveld analysis.

Sample	D_s (Å) maximum error = ±12	$\langle \varepsilon_L^2 \rangle^{\frac{1}{2}}$ (10^{-3}) maximum error = $\pm 5 \times 10^{-5}$	$\rho(10^{15})$ (m^{-2}) maximum error = $\pm 5 \times 10^{13}$
Zirlo	103	1.17	8.09
Zr-2.5 wt.% Nb	100	1.31	9.30
Zircaloy-2	168	1.51	6.38

obtained in our earlier work [14]. Zircaloy-2 being the single phase alloy has a larger domain size. In the early stage of deformation, the predominant slip occurs on (100) plane which is the primary glide plane and the dislocations form coplanar arrays. As deformation proceeds, cross slip takes place and multiplication process operates. The cold worked structure forms high dislocation density regions or tangles, which soon develop into tangled networks or cells. Thus the characteristic microstructure of this alloy in the cold worked state is a cellular substructure resulting from the entanglement of network of dislocations. In this analysis, the average microstrain $\left(\langle \varepsilon^2(L) \rangle^{\frac{1}{2}}\right)$ values did not change significantly in these three alloys.

On the other hand, both Zr-2.5 wt.% Nb and Zirlo have fine distribution of β phase. The dislocations generated during deformation of the soft phase β formed loops around α, which is the hard phase, and created dislocation cell structures or domains. This occurs as the generation of dislocations retains the continuity between the two phases, which is necessary to avoid any void and micro-cracks during deformation.

In the double Voigt analysis, both the size and strain broadened profiles were approximated by a Voigt function and the Cauchy and the Gaussian components of the size and strain broadened profiles (β_{SC}, β_{SG}, β_{DC} and β_{DG}) were separated along <001> and listed in Table 3. From Table 3, it is observed that, in general the size-broadened profiles had both Cauchy and Gaussian components of the integral breadths, except for Zr-2.5 wt.% Nb. In that case, the size-broadened profile is generally Cauchy in nature and strain broadening profile is Gaussian. The D_S values are found to be less in case of both Zirlo and Zr-2.5 wt.% Nb as observed by Modified Rietveld Technique. Fig. 2 shows the variation of microstrain $\left(\langle \varepsilon^2(L) \rangle^{\frac{1}{2}}\right)$ with the Fourier length L for the deformed powdered samples. It seen that the ε values are almost similar for all three samples. Fig. 3 shows the volume weighted column length distribution function $P_v(L)$ of the deformed powdered samples with L. We did not find any systematic

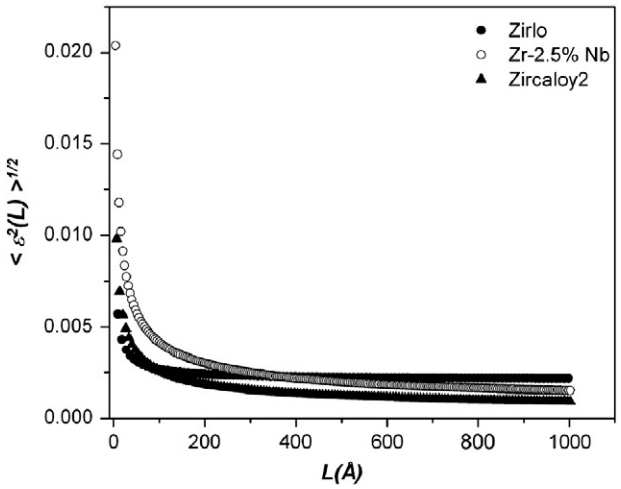

Fig. 2 – Variation of microstrain $\left(\langle \varepsilon^2(L) \rangle^{\frac{1}{2}}\right)$ with Fourier length (L) for deformed powdered samples of Zirlo, Zr-2.5 wt.% Nb and Zircaloy-2 obtained by double Voigt method.

variation in the values of D_v with the change in composition. The size distribution has been significantly narrowed down for Zirlo as seen in Fig. 3.

The model based approaches like the individual profile fitting using Simplified Breadth Method, Modified Rietveld technique and double Voigt analysis have been applied to many studies in the field of materials science. In characterizing the microstructure of the material, these methods are complimentary to each other. The individual peak profile fitting as done in Simplified Breadth Method and double Voigt analysis does not require any structural model which makes the analysis much simpler. In the initial stage of data analysis, these techniques play an important role as we have limited knowledge about the material. The Modified Rietveld technique requires the assumption of the shape profile of the diffraction peaks.

This study helped us to understand the suitability of these techniques for the analysis of the microstructure of the heavily deformed samples of Zirconium-based alloys. Among these techniques, the Simplified Breadth Method and the double Voigt analysis gave information of the microstructure based on only the individual peak analysis. On the contrary, the Modified Rietveld Method gave quantitative information of the microstructural parameters considering all the diffraction peaks. Hence, we find that Modified Rietveld technique is the most suitable technique for the analysis of the microstructure of the deformed solid samples.

Table 3 – Values of D_S, D_V and $\langle \varepsilon^2(L) \rangle^{\frac{1}{2}}$ for heavily deformed powdered samples of Zirlo, Zr-2.5 wt.% Nb and Zircaloy-2 obtained by double Voigt method.

Sample	β_{SC} (10^{-2})	β_{SG} (10^{-2})	β_{DC} (10^{-2})	β_{DG} (10^{-2})	D_S (Å) maximum error = ±15	$\langle \varepsilon^2(L) \rangle^{\frac{1}{2}}$ (10^{-3}) maximum error = $\pm 5 \times 10^{-5}$	D_V (Å) maximum error = ±17
Zirlo	0.43	0.31	0.02	0.18	116	2.46	156
Zr-2.5 wt.% Nb	0.42	–	–	0.32	117	3.38	233
Zircaloy-2	0.29	0.20	0.10	0.04	172	2.77	236

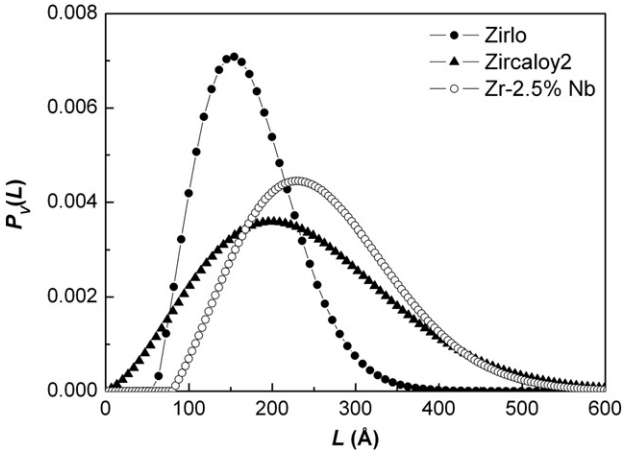

Fig. 3 – Volume weighted column length distribution function for deformed powdered samples of Zirlo, Zr-2.5 wt.% Nb and Zircaloy-2 obtained by double Voigt method.

5. Conclusion

Different model based approaches of X-ray Diffraction Line Profile Analysis have been used to characterize the microstructure of the heavily deformed Zirconium-based alloys. These techniques are suitable as the analysis is much easier, reliable and quick and can be easily adopted in the shop floor practice where characterization of the average microstructural parameters is mandatory. These techniques help to achieve the information of the microstructural parameters like cell size or domain size, dislocation density, microstrain within the domains, averaged over a volume of 10^9 μm^3.

REFERENCES

[1] Warren BE, Averbach BL. The effect of cold-work distortion on X-ray patterns. J Appl Phys 1950;21:595.
[2] Warren BE. X-ray diffraction. Reading (MA): Addision-Wesley; 1969. p. 251.
[3] Ungár T, Mughrabi H, Rönnpagel D, Wilkens M. X-ray line-broadening study of the dislocation cell structure in deformed [001]-orientated copper single crystals. Acta Metall 1984;32:333–42.
[4] Groma I, Ungár T, Wilkens M. Asymmetric X-ray line broadening of plastically deformed crystals. I. Theory. J Appl Cryst 1988;21:47–54.
[5] Groma I, Ungár T, Wilkens M. Asymmetric X-ray line broadening of plastically deformed crystals. II. Evaluation procedure and application to [001]-Cu crystals. J Appl Cryst 1989;22:26–34.
[6] Groma I. X-ray line broadening due to an inhomogeneous dislocation distribution. Phys Rev B 1998;57:7535.
[7] Ungár T, Révész A, Borbély A. Dislocations and grain size in electrodeposited nanocrystalline Ni determined by the modified Williamson–Hall and Warren–Averbach procedures. J Appl Cryst 1998;31:554–8.
[8] Langford JL. Use of pattern decomposition or simulation to study microstructure: theoretical consideration. In: Snyder RL, Fiala J, Bunge HJ, editors. Defects and microstructure analysis by diffraction. New York: International Union of Crystallography, Oxford University Press Inc; 1999.
[9] Aqua EN, Owens CM. The microstructural characterization of cold-rolled Zircaloy-4 sheet. Trans TMS-AIME 1967;239: 155–61.
[10] Kuzel R, Kilmanek P. X-ray diffraction line broadening due to dislocations in non-cubic materials. I. General considerations and the case of elastic isotropy applied to hexagonal crystals. J Appl Cryst 1988;21:59–66.
[11] Kuzel R, Kilmanek P. X-ray diffraction line broadening due to dislocations in non-cubic materials. II. The case of elastic anisotropy applied to hexagonal crystals. J Appl Cryst 1988;21: 363–8.
[12] Kuzel R, Kilmanek P. X-ray diffraction line broadening due to dislocations in non-cubic crystalline materials. III. Experimental results for plastically deformed Zirconium. J Appl Cryst 1989;22: 299–307.
[13] Mukherjee P, Sarkar A, Barat P, Bandyopadhyay SK, Sen Pintu, Chattopadhyay SK, et al. Deformation characteristics of rolled Zirconium alloys: a study by X-ray diffraction line profile analysis. Acta Mater 2004;52:5687–96.
[14] Mukherjee P, Chattopadhyay SK, Chatterjee SK, Meikap AK, Barat P, Bandyopadhyay SK, et al. Microstructural studies on lattice imperfections in deformed Zirconium-base alloys by X-ray diffraction. Metall & Mat Trans A 2000;31A:2405–10.
[15] Chatterjee SK, Halder SK, Sengupta SP. An X-ray diffraction study of lattice imperfections in cold-worked silver–gallium (α-phase) alloys. J Appl Phys 1976;47:411.
[16] Aldridge SA, Cheadle BA. Age hardening of Zr-2.5 wt.% Nb slowly cooled from the ($\alpha+\beta$) phase field. J Nucl Mater 1972;42: 32–42.
[17] Holt RA. Recovery of cold-work in extruded Zr-2.5 wt.% Nb. J Nucl Mater 1976;59:234–42.
[18] de Keijser ThH, Langford JI, Mittemeijer EJ, Vogels ABP. Use of the Voigt function in a single-line method for the analysis of X-ray diffraction line broadening. J Appl Cryst 1982;15:308–14.
[19] Langford JI. A rapid method for analysing the breadths of diffraction and spectral lines using the Voigt function. J Appl Cryst 1978;11:10–4.
[20] Lutterotti L, Scardi P. Simultaneous structure and size–strain refinement by the Rietveld method. J Appl Cryst 1990;23: 246–52.
[21] Williamson GK, Smallman RE. Dislocation densities in some annealed and cold-worked metals from measurements on the X-ray Debye–Scherrer spectrum. Philos Mag 1956;1:34.
[22] Balzar D, Ledbetter H. Voigt-function modeling in Fourier analysis of size- and strain-broadened X-ray diffraction peaks. J Appl Crystallogr 1993;26:97–103.
[23] Selivanov VN, Smislov EF. Analysis of polydispersity in the approximation of the X-ray diffraction profile by the Feught function. Zavod Lab 1991;57:28–9.

Materials Science and Engineering A 528 (2011) 967–972

Contents lists available at ScienceDirect

Materials Science and Engineering A

journal homepage: www.elsevier.com/locate/msea

In situ studies of evolution of microstructure with temperature in heavily deformed Ti-modified austenitic stainless steel by X-ray diffraction technique

P.S. Chowdhury[a], N. Gayathri[a], P. Mukherjee[a,*], M. Bhattacharya[a], A. Chatterjee[a], A. Dutta[b], P. Barat[a]

[a] *Variable Energy Cyclotron Centre, 1/AF Bidhannagar, Kolkata 700064, India*
[b] *Department of Metallurgical and Materials Engineering, Jadavpur University, Kolkata 700032, India*

ARTICLE INFO

Article history:
Received 26 July 2010
Received in revised form
10 September 2010
Accepted 30 September 2010

Keywords:
X-ray diffraction
Microstructural evolution
Austenitic stainless steel
Annealing

ABSTRACT

The mechanism of the evolution of the deformed microstructure at the earliest stage of annealing where the existence of the lowest length scale substructure paves the way to the formation of the so-called subgrains, has been studied for the first time by X-ray diffraction technique. The study has been performed at high temperature on heavily deformed Ti-modified austenitic stainless steel. Significant changes were observed in the values of the domain size, both with time and temperature. Two different types of mechanism have been proposed to be involved during the microstructural evolution at the earliest stages of annealing. The nature of the growth of domains with time at different temperatures has been modelled using these mechanisms. High-resolution transmission electron microscopy has been used to view the microstructure of the deformed and annealed sample and the results have been corroborated successfully with those found from the X-ray diffraction techniques.

1. Introduction

Microstructures arising out due to deformation in solid polycrystalline materials are quite complex and rich in detail, encompassing many more features like texture, grain orientation and rotation than just the microstructure formed due to the generation and entanglement of dislocations. Annealing of these deformed materials results in a change of the microstructure owing to the change in the configurations of dislocation but at the same time the process involves a change in the texture and other microstructural parameters. Extensive early work on the recovery of deformed materials has been reviewed by Beck [1], Bever [2], Titchener and Bever [3]. However, during the later years, the search for quantitative physically based models for the annealing process has shown renewed interest [4]. Various stages in the recovery during annealing are the formation of dislocation tangles and cells, annihilations of dislocation within cells, subgrain formation and subgrain growth [5]. The study of the evolution of the microstructural features during disentanglement of the dislocation network in the very early stages of annealing has not been addressed so far. This study can be carried out during annealing of an aggregate of powder sample in heavily deformed state which has high density of dislocations in the form of tangles. Moreover, the information of the preferred orientation in the powder sample is eliminated due to the randomization of the crystallographic orientation.

There are some evidences of subgrain formation and rotation during the last stages of recovery process where thin foils of few alloy systems were studied *in situ* at high temperature using High Voltage Electron Microscope [6]. Studies of subgrain growth in polycrystals have also been carried out using Molecular Dynamics simulation [7,8]. The sizes of the subgrains in these studies were found to vary within a range of 0.1 μm to few microns. But in the very early stages of microstructural evolution during annealing, the length scales of the substructures are much less than these subgrains. Humphreys and Hatherly [9] have emphasised that the understanding of the mechanism of the formation of the subgrains from the lower length scale substructures is difficult or rather impossible as the microstructural evolution during this stage cannot be observed *in situ*. The overlap of the strain field due to the presence of high density dislocation tangles in deformed sample imposes a limitation to view the region by Transmission Electron Microscope in the very early stages of annealing. On the contrary, X-ray diffraction (XRD) technique can be a unique characterisation tool to obtain the statistically averaged information of the evolution of the spatially heterogeneous substructure of the deformed polycrystalline materials *in situ* during annealing as the wavelength of X-ray is comparable with the length scale of these dislocation substructures. For the first time we have used XRD technique to study the microstructural changes during the very early stage of annealing. In the following text these substructures will be referred to, as domain.

There are many theoretical and experimental studies involving the kinetics of the subgrain growth during the recovery period of the annealing process [10–18]. Sandström [19] have proposed a

* Corresponding author. Tel.: +91 33 2318 4460; fax: +91 33 2334 6871.
E-mail address: paramita@vecc.gov.in (P. Mukherjee).

0921-5093/$ – see front matter © 2010 Elsevier B.V. All rights reserved.
doi:10.1016/j.msea.2010.09.102

Table 1
Chemical composition in wt% of Alloy D9.

C	Mn	Ni	Cr	Mo	N	Ti	S	P	Fe
0.05	1.50	15.04	15.09	2.26	0.006	0.21	0.003	0.01	Balance

model describing the subgrain growth to occur in different ways: by migration of sub-boundaries or dissolution of sub-boundaries. The dynamical process involved during the earliest stage of annealing leading to the formation of domains of size around 10 nm from loose dislocation tangles has not been addressed so far due to the experimental limitation to view the domains of such length scale. Moreover the process of rearrangement of dislocations being very fast, it was not feasible to capture the evolution of the domain in the earliest stage of annealing under TEM for pure metals or very dilute alloys. The process of rearrangement of dislocations can be studied at this stage only if the kinetics can be slowed down by addition of alloying elements. There are substantial evidences that fine particle dispersion may exert strong pinning effect on the growth of subgrains [20,21].

We have carried out our studies on Ti-modified austenitic stainless steel (D9), rich in alloying elements, which is an important structural material for Prototype Fast Breeder Reactors [22]. This material shows a very good combination of high temperature tensile and creep strength properties, irradiation creep resistance and resistance to irradiation induced void swelling [23,24]. We have extracted the powder sample from the bulk annealed material by introducing severe deformation using fine jewellery file. The evolution of the microstructural changes as a function of temperature and time of the powdered sample has been studied *in situ* with the help of high temperature X-ray diffractometer. We have studied the variation of the domain size and microstrain using X-ray diffraction Line Profile Analysis (XRDLPA) systematically as a function of temperature and time to understand the evolution of microstructure in the very early stages of annealing.

2. Experimental

The chemical composition of alloy D9 is given in Table 1. The steel was obtained in the form of rods of 30 mm diameter in the hot rolled condition. Rods of 26 mm diameter were machined from these hot rolled rods and given a solution annealing treatment at 1373 K for 1/2 h followed by water quenching.

The highly deformed D9 powder was prepared from these annealed D9 rods with the help of finely threaded jewellery files. Fine particles in the size range 74–88 μm were extracted from this D9 powder using 170 and 200 mesh sieves.

The High Temperature X-ray Diffraction experiments were carried out on these samples using the Bruker AXS D8 Advance Diffractometer with the Anton Paar high temperature attachment HTK 16. The attachment consisted of a Platinum (Pt) strip heater on which the sample is mounted. The whole stage was isolated from the surroundings by a vacuum chamber which was connected to a turbo molecular pump to maintain a high vacuum. During the experiments, the vacuum inside the chamber was better than 5×10^{-5} mbar.

A required amount of the D9 powder sample was collected on a slide and then mixed with a few drops of isopropyl alcohol and a drop of Zapon^{TM} which acted as a binder. This mixture was then pasted uniformly on the Pt strip heater in a rectangular shape. Special care was taken during the mounting of the sample to maintain the uniformity in the dimension and packing, for all the experiments.

Two different experiments using high temperature X-ray Diffractometer were carried out on the samples using Co-K_α radiation. In one of the experiments, an attempt was made to study the kinetics of the evolution of the microstructure of the samples at different elevated temperatures 673 K, 773 K, 823 K, 838 K, 845 K, 853 K and 873 K. Since, the rearrangement of dislocations is a thermally assisted phenomenon, we had to restrict the annealing studies up to 873 K so that the related kinetics of the microstructural evolution at a very early stage could be detected by XRD. In each case the sample was brought to the desired temperature at a rate of 1.66 K/s and then the X-ray scan was started. To understand the kinetics of the microstructural evolution, it is required to collect the information of the evolution *in situ* at a close interval of time. Since the time required for a full profile scan was much larger (almost around 30 min with the scan step of 0.02° taken at 0.5 s/step) the study was limited to the highest intensity peak (1 1 1) only which is also the slip plane of the Ti-modified austenitic stainless steel. The scan was performed between 48° and 53.5° which required a minimum scan time of 222 s including the instrument adjustment time after optimizing different instrumental parameters for obtaining an acceptable peak to background ratio for the (1 1 1) peak. One hundred and forty five number of X-ray scans for (1 1 1) peak were collected successively within a time of 9 h to understand the kinetics.

In the other experiment, the X-ray data was collected *in situ* at room temperature and subsequently at different elevated temperatures ranging from 323 K to 873 K. At each temperature, the scan range of 2θ was 26° to 122° with a step of 0.02° taken at 0.5 s/step. Each sample was heated to the required set temperature and a soaking time of 9 h was allowed for the sample to stabilise its microstructural evolution before acquisition of the data. The experiment was performed several times to check the reliability and repeatability of the observed data.

TEM studies were carried out on the deformed and annealed (annealed at 873 K for 9 h) powder samples. In each case, a small quantity of the powder was suspended in acetone solution and the solution was sonicated for 7 h. A drop of this solution was dropped onto TEM grids and was allowed to dry and stored in a vacuum dessicator. The micrographs were obtained using a JEOL 200 kV TEM at the unit of Nanoscience and Technology, IACS, Kolkata, India.

3. Method of analysis

3.1. Single peak analysis

The single peak analysis of the diffraction pattern of the (1 1 1) plane has been performed to characterise the *in situ* time dependent evolution of the microstructure at different elevated temperatures. The true integral breadth (β) of each XRD (1 1 1) peak profile was evaluated after correcting for the Debye Waller factor at that particular temperature and also for the instrumental broadening contribution. This β was used to calculate the volume weighted average domain size (D_v) from the Scherrer's equation [25]:

$$D_v = \frac{0.9\lambda}{\beta \cos\theta} \quad (1)$$

3.2. Modified Rietveld method

The microstructural variation with temperature has been studied by full powder pattern fitting technique using the Modified Rietveld method on the diffraction profiles. In this method, the diffraction profiles have been modelled by the pseudo-Voigt function using the program LS1 [26]. This program includes the simultaneous refinement of the crystal structure and the microstructural parameters like the domain size and the microstrain within the domain. The method involves the Fourier analysis of the broadened peaks. Considering an isotropic model, the lattice parameter (a), surface weighted average domain size (D_s) and the

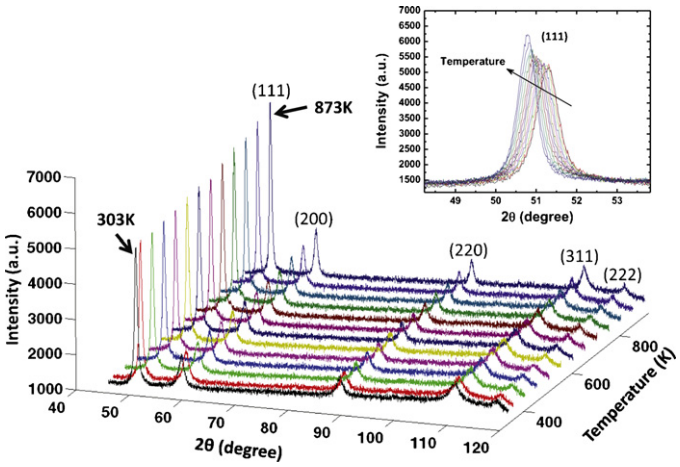

Fig. 1. XRD profiles of heavily deformed D9 powder sample at different temperatures.

average microstrain $\langle \varepsilon_L^2 \rangle^{1/2}$ were used simultaneously as the fitting parameters to obtain the best fit. Having obtained the values of D_s and $\langle \varepsilon_L^2 \rangle^{1/2}$, the average domain size and microstrain were further refined using anisotropic model to estimate the effective domain size (D_e) for each crystallographic plane.

4. Results and discussion

The variation of β with time is obtained from the single peak analysis at different temperatures. The value of β becomes almost stationary at different temperatures after 9 h. Hence it can be assumed that there is saturation in the evolution of the microstructure which helped us to choose a definite soaking time at each temperature for the second experiment.

Fig. 1 represents the XRD profile of the samples at room temperature and at higher temperatures after soaking of 9 h. The figure clearly reveals the changes in the intensity patterns due to the change in the temperature. The inset of Fig. 1 shows changes in the intensity of the (1 1 1) peak in an expanded scale.

Fig. 2 represents the Rietveld fit of a typical XRD profile at a temperature of 823 K. The variations of D_s (Table 2) and $\langle \varepsilon_L^2 \rangle^{1/2}$ of these samples are shown as a function of temperature in Fig. 3 and Fig. 4 respectively.

Significant changes were observed in the values of D_s with temperature. The average size of the domain was found to be around 14 nm at room temperature. It is seen that initially the increase in D_s is quite small up to the temperature around 673 K but a steep rise is observed after this temperature, reaching a value of ~29 nm at 873 K. The formation of domains at room temperature and at high temperature depends on the arrangement of dislocations during

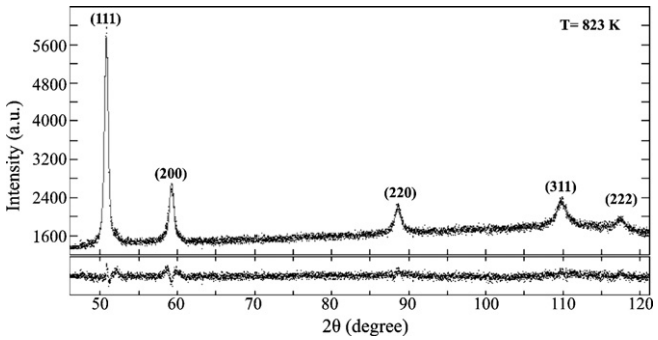

Fig. 2. Rietveld fit of a typical XRD profile at a temperature of 823 K.

Table 2
Variation of surface weighted average domain size D_s for the D9 powder sample as a function of temperature.

Temperature (K)	Surface weighted average domain size D_s (nm)
303	14.19 ± 0.10
323	14.59 ± 0.30
373	14.99 ± 0.10
423	15.42 ± 0.26
473	15.74 ± 0.41
523	15.98 ± 0.31
573	16.56 ± 0.12
583	16.32 ± 0.11
593	16.68 ± 0.30
603	16.89 ± 0.49
613	16.82 ± 0.31
623	16.92 ± 0.43
633	17.00 ± 0.32
643	17.18 ± 0.32
653	16.92 ± 0.47
663	17.41 ± 0.18
673	18.11 ± 0.37
683	18.21 ± 0.37
693	18.21 ± 0.24
703	18.21 ± 0.24
713	19.00 ± 0.30
723	19.65 ± 0.21
733	20.07 ± 0.42
743	20.23 ± 0.43
753	20.63 ± 0.48
763	21.15 ± 0.50
773	21.61 ± 0.51
823	24.29 ± 0.82
873	28.86 ± 0.64

the process of deformation and their mobility by glide and climb during annealing [27]. The steep increase in D_s after 673 K can be attributed to the higher probability of dislocation rearrangement and annihilation at high temperature by the process of climb which provides an additional degree of freedom for the movement of dislocations.

The variation of the values of the effective domain size D_e at different crystallographic planes shows strong anisotropy at all temperatures (Fig. 5 and Table 3). The increase in D_e with temperature up to 673 K may be attributed to the glide process. The movements of dislocations in the crystallographic planes (1 1 1) and (2 2 0) occur by easy glide and hence the variation in D_e with temperature is monotonic. On the contrary, the movement of dislocations by glide is restricted for the crystallographic planes (2 0 0) and (3 1 1) and an anomalous behaviour of D_e with temperature

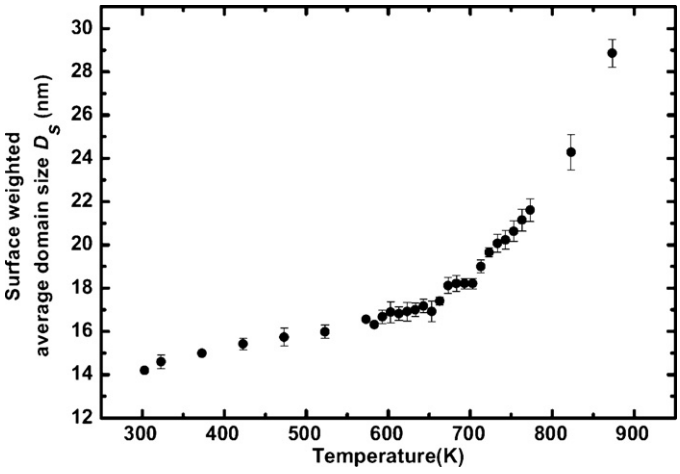

Fig. 3. Variation of surface weighted average domain size D_s for the D9 powder sample as a function of temperature.

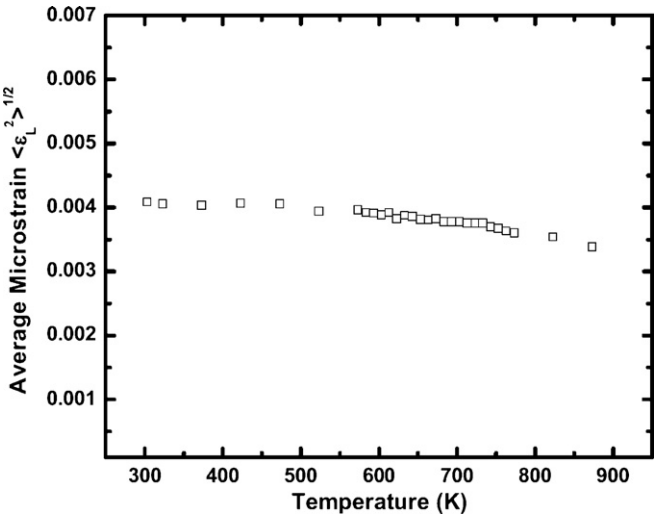

Fig. 4. Variation of average microstrain $\langle \varepsilon_L^2 \rangle^{1/2}$ in the D9 powder sample as a function of temperature.

Table 3
Variation of effective domain size D_e with temperature along different crystallographic planes.

Temperature (K)	Effective domain size D_e with temperature along different crystallographic planes (nm), maximum error = ±0.65 nm			
	D_e (111)	D_e (200)	D_e (220)	D_e (311)
303	15.66	14.93	18.31	15.13
323	15.93	14.18	18.68	14.68
373	16.07	14.90	18.84	15.23
423	16.11	13.73	18.73	14.41
473	16.42	16.05	19.17	16.15
523	16.87	10.62	19.73	12.68
573	17.62	15.28	20.61	15.95
623	18.11	18.23	21.33	18.20
673	18.64	17.50	21.73	17.82
723	20.17	14.00	23.52	15.93
773	21.17	17.83	24.54	18.80
823	23.95	21.38	27.72	22.11
873	28.31	28.03	32.74	28.11

up to 673 K is observed. However at high temperature, the climb process becomes active which minimises this anomaly.

On the other hand, the microstrain values $\langle \varepsilon_L^2 \rangle^{1/2}$ (Fig. 4) did not change significantly up to the temperature of 873 K. This observation is quite expected in case of the alloy D9 which is rich in alloying elements. The high solute content in the alloy restricts the movement of dislocations [28], preventing the microstrain to be relaxed even up to 873 K. Hence it can be conjectured that the change in peak profiles is primarily governed by the variation in the domain size. In our next part of the discussion, the variation in the peak broadening with temperature and time has been considered to arise solely from the domain size.

In order to study the kinetics of the growth of the domains, the β of the (1 1 1) peak estimated from our first experiment were used to obtain the evolution of normalised D_v (with respect to D_0 at each data set, where D_0 is the initial domain size) with time at different temperatures, as shown in Fig. 6. It is clearly evident from the figure that the growth rate of domains at the initial stage is significantly high as compared to that of the later stage. In a heavily deformed sample, the high population of loosely bound dislocations introduced into the sample form tangles as shown schematically in Fig. 7(a). When thermal energy is supplied to the sample, these dislocations rearrange themselves as shown in Fig. 7(b) resulting in a decrease in the configurational entropy of the system. Consequently the internal energy is also lowered, which in effect, reduces the total free energy (Helmholtz free energy) of the system. Thus the overall dynamical process leads to the formation of domains as shown in Fig. 7(c, d). Due to this rearrangement of dislocations, the localized density of dislocations at the domain boundary becomes very high as compared to the interior of the domain. As a result, the probability of annihilation of these dislocations increases leading to the growth of the domains as shown in Fig. 7(e). Thus it can be

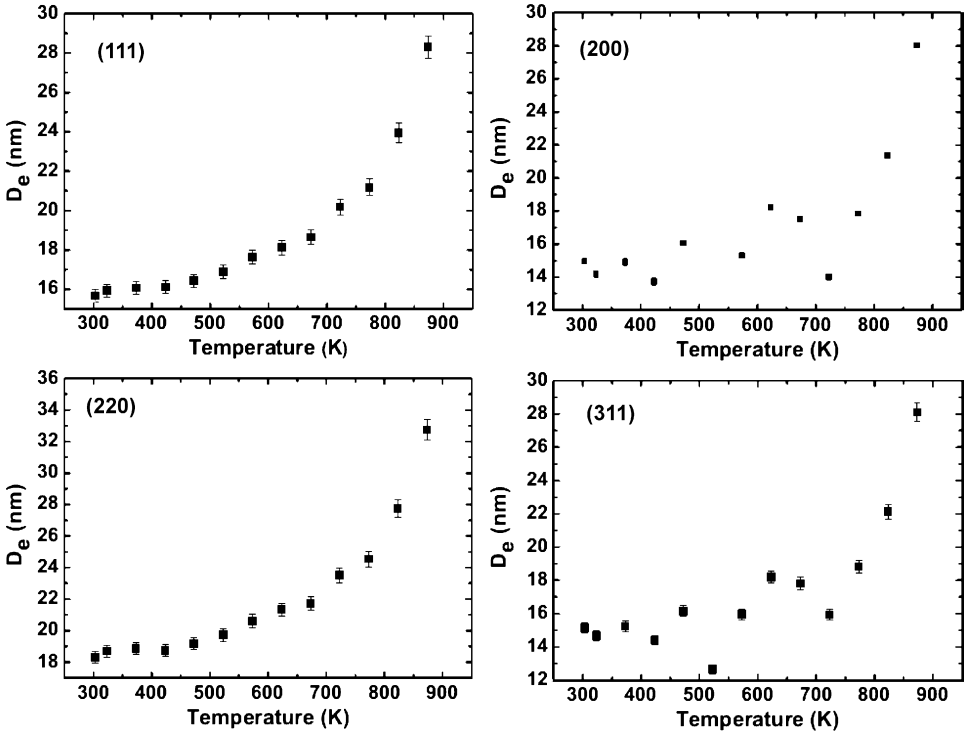

Fig. 5. Variation of effective domain size D_e with temperature along different crystallographic planes.

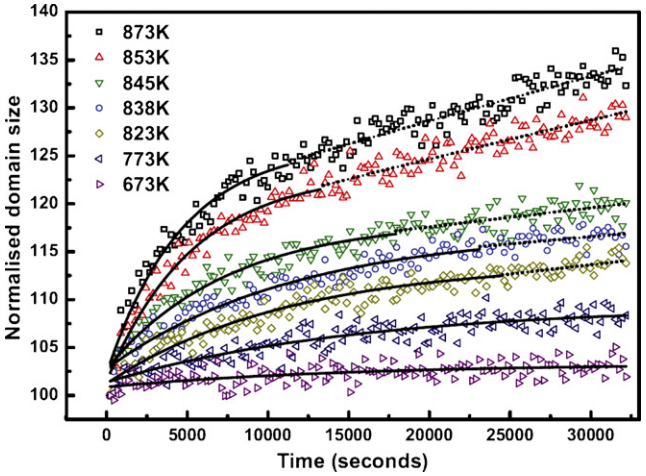

Fig. 6. Evolution of normalized volume weighted domain size D_v with time at different temperatures for the D9 powder sample. The solid and the dotted lines represent the final fit of the experimental data using Eqs. (2) and (3) respectively.

conjectured that the evolution of domain growth in the very early stages of annealing as seen in Fig. 6, is governed by two simultaneous mechanisms, one is rearrangement of dislocations which is predominant in the initial stage (stage I), and the other is their annihilation which is dominant in the later stage (stage II). We have not considered the dynamics of domain rotations in our discussion as it is well known that this plays a significant role at high temperature [9].

In the initial stage, the loosely bound dislocations participate in the formation of domains and this process continues till a low angle tilt boundary with high dislocation density is achieved and the formation of domains is almost complete. Consequently, the rate of increase in domain size is significantly higher in stage I as compared to stage II (Fig. 6). In stage II, this rate decreases drastically as the domains almost attain a fixed size and the entangled dislocations at the domain boundary annihilate each other.

These two distinctly different dynamical processes responsible for the evolution of the domains in the very early stage of annealing can be mathematically modelled as follows:

Had the process of rearrangement of dislocations been the sole mechanism for the increase in the size of the domains, these would certainly lead to a saturated average domain size (D_m). Hence, at any instance of time for a fixed temperature, the rate of increase of domain size (D_v) will be proportional to the difference ($D_m - D_v$), i.e.

$$\frac{dD_v}{dt} = k_1(D_m - D_v)$$

where k_1 is the rate constant. This leads to

$$D_v(t) = D_m - (D_m - D_v|_{t=0}) \exp\left(\frac{-t}{\tau}\right) \quad (2)$$

where $\tau = 1/k_1$, which is the characteristic time of the dynamical process.

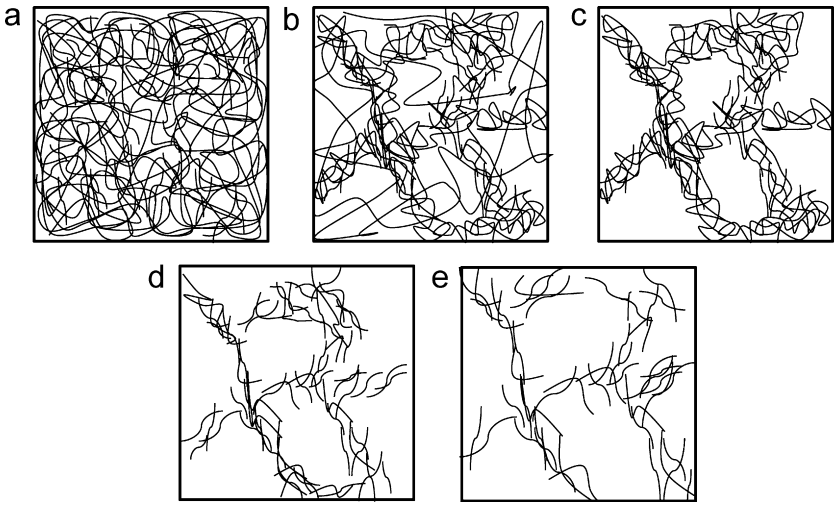

Fig. 7. Schematic representation of the (a) randomly distributed dislocations in heavily deformed sample, (b) initial stage of dislocation rearrangement, (c) formation of domains with rearrangement of dislocation, (d) annihilation of dislocation and (e) growth of domains due to dislocation annihilation.

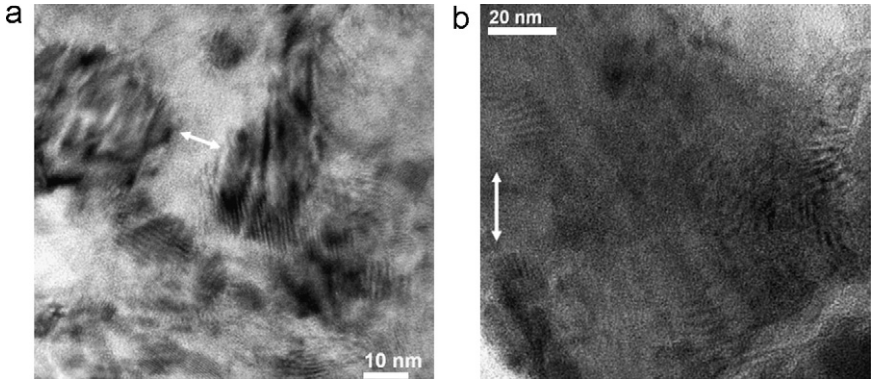

Fig. 8. Transmission Electron Micrographs for (a) heavily deformed D9 powder sample, (b) sample after 9 h annealing at a temperature of 873 K.

In the dynamical process involving annihilation of dislocations in stage II, the annihilation rate will be high for small sized domains as the average density of dislocations per unit volume is more for small domains, resulting in higher probability of annihilation. Hence the rate of increase of the domain size can be mathematically modelled as:

$$\frac{dD_v}{dt} = \frac{k_2}{D_v^n}$$

where k_2 is the rate constant. This leads to the equation

$$D_v^2 = D_0^2 + Bt \quad (3)$$

with $n = 1$. Here, D_0 is the initial average domain size of this process and B is a constant.

Eqs. (2) and (3) have been used to model the increase in the domain size as seen in Fig. 6. The solid and the dotted lines represent the final fit of the experimental data using Eqs. (2) and (3) respectively. It is seen clearly from Fig. 6 that the first mechanism (rearrangement of dislocations) switches over to the second mechanism (annihilation of dislocation) at a lower time with the increase in temperature. This can be explained by the thermally activated climb process which becomes easier at high temperature; thus facilitating the rearrangement and annihilation of the dislocations to take place much faster. However, below 823 K it is interesting to note that the data at temperatures 673 K and 773 K could be fitted with Eq. (2) only. This signifies that the small increase in the domain size results due to the rearrangement of the dislocations only. Hence it can be conclusively stated that below 823 K, even if the annealing is done for a sufficiently long time, complete recovery would never be achieved in Ti-modified austenitic stainless steel.

TEM studies were carried out at room temperature on heavily deformed powder sample and on annealed sample at 873 K for 9 h and the micrographs are shown in Fig. 8(a) and (b) respectively. Fig. 8(a) shows the presence of highly strained regions due to the formation of high dislocation tangles throughout the matrix as expected in a heavily deformed structure. Annealing at 873 K for 9 h still did not result in significant removal of these structures which is clearly seen by the presence of strained region even at 873 K in Fig. 8(b). It is also seen that the spacing between the consecutive distorted regions is of the order of 10 nm for heavily deformed sample and 20 nm for the annealed sample. These values correspond to the coherent region (domain) as detected by the XRD.

5. Conclusion

The microstructural evolution of heavily deformed D9 powder samples during the very early stage of annealing has been studied *in situ* with time and temperature by high temperature X-ray diffraction techniques. A systematic increase in the domain size was observed with the increase in temperature. The kinetics of the microstructural evolution has been found to follow mainly two different mechanisms, one is the rearrangement of dislocations and another is their annihilation. The climb process becomes active at high temperature which finally governs the kinetics of both rearrangement and annihilation of dislocations.

Acknowledgement

One of the authors (A. D.) acknowledges CSIR, India for providing financial support.

References

[1] P.A. Beck, Adv. Phys. 3 (1954) 245–324.
[2] M.B. Bever, Creep and Recovery, ASM, Cleveland, 1957, pp. 14–15.
[3] A.L. Titchner, M.B. Bever, Prog. Met. Phys. 7 (1958) 247–338.
[4] E. Nes, Acta Metall. Mater. 43 (1995) 2189–2207.
[5] F.J. Humphreys, M. Hatherly, Recrystallization and Related Annealing Phenomena, Elseiver Ltd, Oxford, 2004, p. 170.
[6] F.J. Humphreys, H.M. Chan, Mater. Sci. Technol. 12 (1996) 143–148.
[7] D. Moldovan, D. Wolf, S.R. Phillpot, A.J. Haslam, Acta Mater. 50 (2002) 3397–3414.
[8] A.J. Haslam, S.R. Phillpot, D. Wolf, D. Moldovan, H. Gleiter, Mater. Sci. Eng. A 318 (2001) 293–312.
[9] F.J. Humphreys, M. Hatherly, Recrystallization and Related Annealing Phenomena, Elseiver Ltd, Oxford, 2004, p. 202.
[10] R. Sandström, E. Lehtinen, B. Hedman, I. Groza, J. Karlson, J. Mater. Sci. 13 (1978) 1229–1242.
[11] T. Furu, E. Nes, in: Fuentes, Sevillano (Eds.), Growth Rates of Recrystallized Grains in Highly Deformed Commercial Purity Aluminium, an Experimental and Modelling Study, Recrystallization'92, San Sebastian, Spain, 1992, pp. 311–316.
[12] Y. Huang, F.J. Humphreys, Acta Mater. 48 (2000) 2017–2030.
[13] C.J.E. Smith, I.L. Dillamore, Met. Sci. 4 (1970) 161–167.
[14] S.K. Varma, B.L. Willets, Metall. Trans. A 15 (1984) 1502–1503.
[15] S.K. Varma, B.C. Wesstrom, J. Mater. Sci. Lett. 7 (1988) 1092–1093.
[16] S.K. Varma, Mater. Sci. Eng. 82 (1986) L19–L22.
[17] P.A. Beck, B.G. Ricketts, A. Kelly, Trans. Metall. Soc. A.I.M.E. 180 (1949) 160.
[18] M. Ferry, F.J. Humphreys, Acta Mater. 44 (1996) 1293–1308.
[19] R. Sandström, Acta Metall. 25 (1977) 897–904.
[20] F.J. Humphreys, J.W. Martin, Philos. Mag. 17 (1968) 365–403.
[21] R. Sandström, Acta Metall. 25 (1977) 905–911.
[22] Selection of materials for PFBR nuclear steam supply system components—technical note # PFBR-MDG-2002-01, Kalpakkam.
[23] S. Latha, M.D. Mathews, P. Parameswaran, K. Bhanu Sankara Rao, S.L. Mannan, Int. J. Press. Vessels Pip. 85 (2008) 866–870.
[24] C. David, B.K. Panigrahi, S. Balaji, A.K. Balamurugan, K.G.M. Nair, G. Amarendra, C.S. Sundar, Baldev Raj, J. Nucl. Mater. 383 (2008) 132–136.
[25] P. Scherrer, Nachr. Gott. 2 (1918) 98–100.
[26] L. Lutterotti, P. Scardi, J. Appl. Crystallogr. 23 (1990) 246–252.
[27] G.E. Dieter, Mechanical Metallurgy, third ed., McGraw-Hill Book Company Limited, London, 1988.
[28] B. Verlinden, J. Driver, I. Samajdar, R.G. Doherty, Thermo-Mechanical Processing of Metallic Materials, first ed., Elsevier Ltd, Netherlands, 2007.

Bull. Mater. Sci., Vol. 34, No. 3, June 2011, pp. 507–513. © Indian Academy of Sciences.

Post irradiated microstructural characterization of Zr–1Nb alloy by X-ray diffraction technique and positron annihilation spectroscopy

P S CHOWDHURY, P MUKHERJEE*, N GAYATHRI, M BHATTACHARYA, A CHATTERJEE, P BARAT and P M G NAMBISSAN†

Variable Energy Cyclotron Centre, 1/AF Bidhan Nagar, Kolkata 700 064, India
†Saha Institute of Nuclear Physics, 1/AF Bidhan Nagar, Kolkata 700 064, India

MS received 12 September 2010; revised 22 December 2010

Abstract. **Zr–1Nb samples were irradiated with 116 MeV O^{5+} ions at different doses ranging from 5×10^{17} to 8×10^{18} O^{5+}/m^2. X-ray diffraction line profile analysis was performed to characterize the microstructural parameters of these samples. Average domain size, microstrain and dislocation density were estimated as a function of dose. An anomaly was observed in the values of these parameters at a dose of 2×10^{18} O^{5+}/m^2. Positron annihilation spectroscopy was used to determine the existence and nature of vacancy clusters in the samples. Isochronal annealing was carried out for a sample to study the evolution of defect clusters.**

Keywords. **Microstructure; defects; X-ray diffraction technique; positron annihilation spectroscopy.**

1. Introduction

Zirconium based alloys are used extensively as the nuclear structural materials in the pressurized heavy water reactors. These alloys have a combination of good corrosion resistance, mechanical properties at elevated temperatures and resistance to irradiation induced dimensional changes (Sabol *et al* 1989). Still there is a search for new zirconium alloys for meeting the demands of high burn up fuels, higher coolant temperature and partial boiling of coolant. In this respect, binary Zr–Nb alloys containing about 0·5–2% Nb and quaternary Zr–Nb–Sn–Fe alloys have shown considerable promise (Sabol *et al* 1989, 1991; Nikulina *et al* 1996).

The mechanical properties of zirconium based alloys at high temperature are mainly affected by alloying elements, precipitates and microchemistry. Several advanced zirconium based alloys, such as Zirlo (Zr–1Nb–1Sn–0·1Fe), Zr–1Nb, Zr–0·1Nb–1·0Sn–0·2Fe–0·1Cr have been developed as candidate materials for fuel cladding tube which can support higher fuel burn up and a higher operating temperature. The irradiation induced point defects play a significant role on the microstructure, mechanical and creep properties of these alloys (Nikulina *et al* 1996). Several irradiation studies have been performed on zirconium based alloys over the past forty years. It is found that the nature of production of defects is very complex and depends on initial microstructure, alloying elements, type of ions, dose and dose rate. Particularly at low dose and dose rate, a transient regime is observed before attaining a steady state regime where the microstructure is dose dependent. In our earlier study (Mukherjee *et al* 1999) of the microstructure of proton irradiated Zr–1Nb–1Sn–0·1Fe at different doses, we have observed that Nb and Sn played a significant role in suppressing the vacancy agglomeration by forming the solute atom vacancy complexes.

In order to understand the mechanism of evolution of defects in the transient regime, Zr–1Nb samples were irradiated at room temperature with 116 MeV O^{5+} at low doses and at low dose rate. The microstructural parameters of the irradiated samples have been characterized by X-ray diffraction line profile analysis (XRDLPA) and positron annihilation spectroscopy (PAS). During the XRD experiment, X-ray probes an average volume of 10^9 μm^3. Thus the global microstructural information on the irradiated samples could be extracted in a statistical manner using XRDLPA. On the contrary, PAS provides the intrinsic characteristics of the lattice defects in a much shorter length scale. Hence, information obtained from these two techniques are complementary and possibly gives a detailed account of the irradiated microstructure in a non-destructive way.

2. Experimental

Zr–1Nb alloy was prepared by hot extrusion and beta-quenching followed by a second hot extrusion and cold rolling. These deformed samples were then annealed at 580°C for 1 h. The thickness of the sample was 0·6 mm.

Samples of dimension 10×10 mm were cut and then irradiated with 116 MeV O^{5+} from variable energy cyclotron (VEC), Kolkata. The irradiation doses were 5×10^{17},

*Author for correspondence (paramita@veccal.ernet.in)

1×10^{18}, 2×10^{18} and 8×10^{18} O^{5+}/m^2. The beam current was kept constant at 150 nA. The flange used in the irradiation was cooled by continuous flow of water. During irradiation, the average temperature of the sample did not rise above 313 K as measured by the thermocouple connected to the closest proximity of the sample. The rise of temperature up to 313 K was attained within 160 s in each case and then became stable at that temperature.

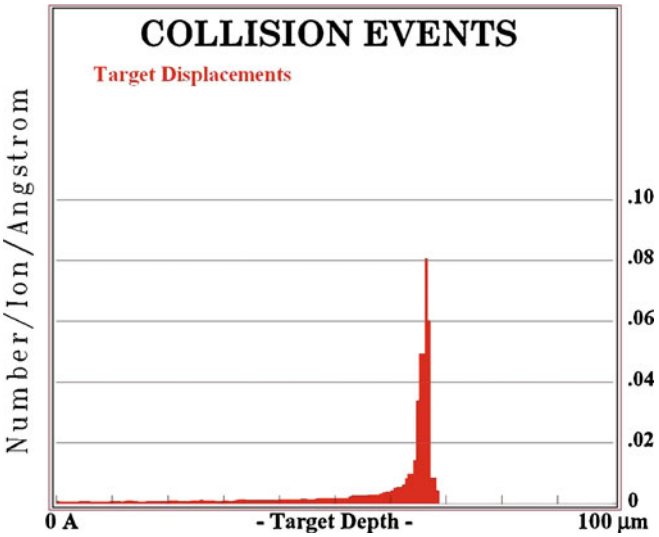

Figure 1. Target displacements by 116 MeV O^{5+} ions on Zr–1Nb alloy.

X-ray diffraction profiles for each irradiated sample have been recorded with the help of Bruker D-8 Advance diffractometer using Cu-Kα radiation. The range of 2θ was 30°–101° with a step scan of 0·02°. The time per step was 20 s.

PAS was performed on the unirradiated and irradiated samples. The positron source used was ^{22}Na with a strength ~10 µCi. The source was covered with a very thin nickel foil (~2 µm thickness) and was sandwiched between two samples having same irradiation doses, such that the irradiated surfaces of the samples face each other. This source-sample assembly was then placed between two BaF_2 detectors. The time resolution of the prompt gamma–gamma coincidence of the circuit was 200 ps as measured by a ^{60}Co gamma source. PAS measurements were also carried out on the specimen irradiated at a dose of 1×10^{18} O^{5+}/m^2 after different stages of isochronal annealing in a temperature range 373–1073 K at an interval of 100 K.

3. Method of analysis

Apart from the instrumental broadening, the broadenings associated with different Bragg peaks in the X-ray diffraction pattern arise due to the microstructural imperfections inside the polycrystalline sample, like domain size and microstrain. This microstructural information can be extracted successfully by analysing the X-ray diffraction pattern using different model based approaches. The Williamson–Hall technique and the modified Rietveld method have been adopted to

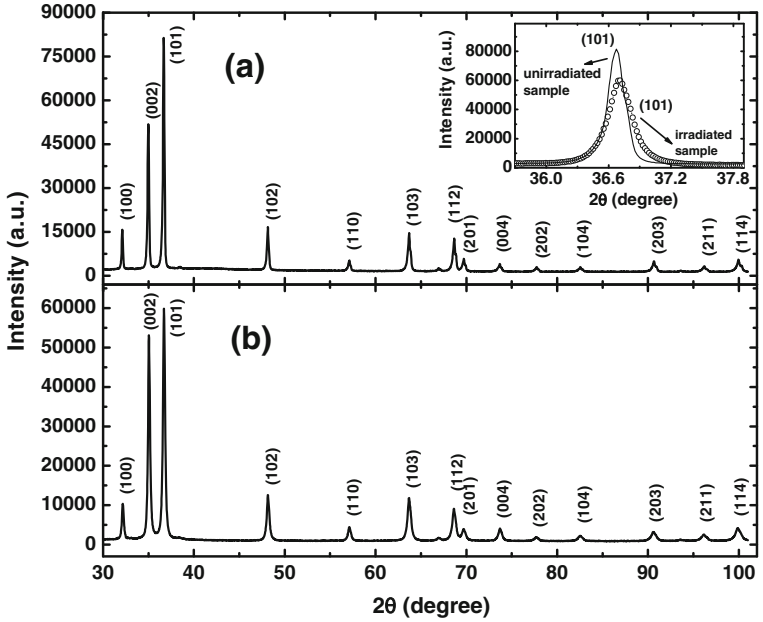

Figure 2. XRD profiles for **(a)** unirradiated sample and **(b)** sample irradiated with 8×10^{18} O^{5+}/m^2. The broadening of the (101) peak for the irradiated sample with respect to the unirradiated one has been shown clearly in the inset.

study the microstructural variation as a function of dose from XRDLPA. The data obtained from PAS have been analysed using the conventional two-state trapping model.

3.1 *Williamson–Hall technique*

According to the Williamson–Hall technique (Williamson and Hall 1953), it is assumed that, both the size and strain broadened profiles are Lorentzian. Based on this assumption, a mathematical relation was established (Williamson and Hall 1953) between the integral breadth (β), the volume weighted average domain size (D_v) and the upper limit of the microstrain (ε) as follows:

$$\frac{\beta\cos\theta}{\lambda} = \frac{1}{D_v} + 2\varepsilon S, \tag{1}$$

where $S = (2\sin\theta/\lambda)$.

The plot of $(\beta\cos\theta/\lambda)$ versus S gives the value of ε from the slope and D_v from the ordinate intercept.

3.2 *Modified Rietveld method*

In this method, the diffraction profiles have been modeled by the pseudo-Voigt function using the program LS1 (Lutterotti and Scardi 1990). This program simultaneously refines the crystal structures, microstructural parameters like surface weighted average domain size (D_S), average microstrain $\langle\varepsilon_L^2\rangle^{1/2}$ and the preferred orientation parameter, assuming the isotropicity in the domain size and microstrain. Preferred orientation correction parameter $P(\alpha)$ (Dollase 1986; Will *et al* 1988) has the form

$$P(\alpha) = \left(r^2\cos^2\alpha + \frac{\sin^2\alpha}{r}\right)^{-\frac{3}{2}}, \tag{2}$$

where α is the angle between *hkl* and the preferred oriented plane and r is an adjustable parameter. XRD peak profile of Zr–1Sn–1Nb–0·1Fe shows strong crystallographic texture along certain crystallographic directions, particularly (002) and (101). The h, k, l values of these planes were incorporated in the programme as preferred oriented planes and the best fit was sought in each case. Having obtained the values of average D_S and $\langle\varepsilon_L^2\rangle^{1/2}$ from isotropic model, the average domain size and strain were further refined to calculate effective domain size and microstrain for each crystallographic plane. Considering the X-ray line profiles to be symmetric in shape, the distributions of dislocations were assumed to be random. The average dislocation density (ρ) has been estimated from the relation (Williamson and Smallman 1956)

$$\rho = (\rho_D\rho_S)^{\frac{1}{2}},$$

where $\rho_D = 3/D_S^2$ (density of dislocation due to domain) and $\rho_S = k\langle\varepsilon_L^2\rangle/b^2$ (density of dislocation due to strain), k is the material constant and b the modulus of the Burger's vector $\frac{1}{3}[11\bar{2}0]$.

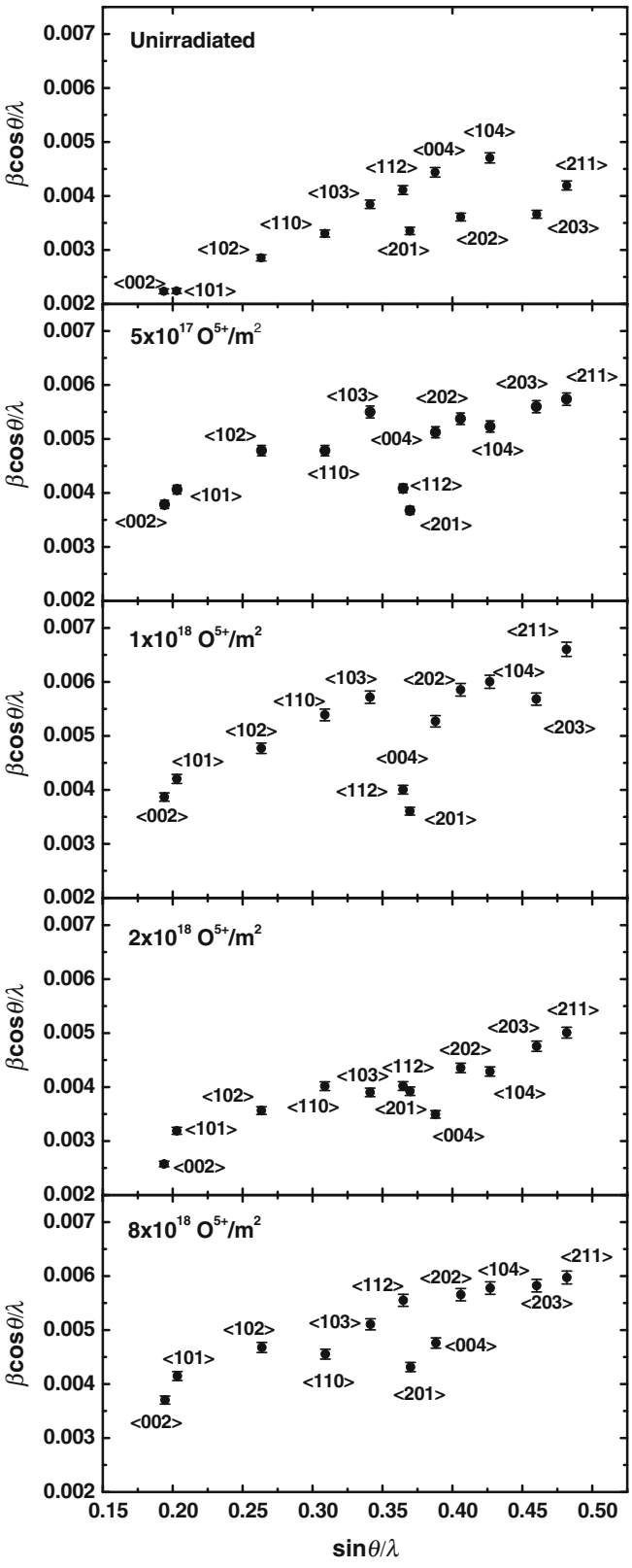

Figure 3. Williamson–Hall plot of Zr–1Nb samples at different irradiation doses.

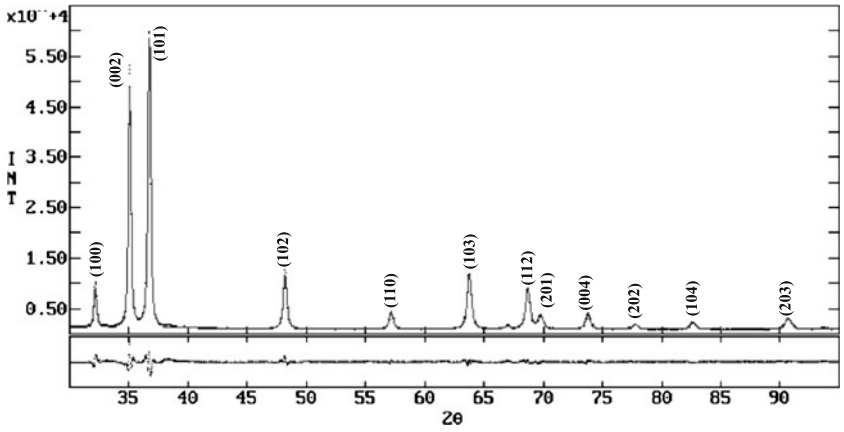

Figure 4. Rietveld fit for the diffraction profile of the oxygen-irradiated Zr–1Nb sample at a dose of 8×10^{18} O^{5+}/m^2. Residuals of the fit are also shown in the lower box.

3.3 *Analysis of PAS data*

The data obtained from PAS has been analysed using the conventional two-state trapping model (Hautojarvi and Corbel 1995). It is assumed in this model that the positrons can either annihilate in the free state in the bulk with a rate λ_b or annihilate after being trapped into a vacancy type defect with a reduced rate λ_t. At a given instant of time t, if n_b and n_t are the number of positrons in the bulk and the defects respectively, the two rate equations governing the annihilation processes can be written as (Hautojarvi and Corbel 1995)

$$\frac{dn_b}{dt} = -n_b\lambda_b - n_b\kappa_t, \tag{3}$$

and

$$\frac{dn_t}{dt} = -n_t\lambda_t + n_b\kappa_t, \tag{4}$$

where κ_t is the rate of trapping of positrons by the defects. Assuming that the positrons are initially released into the bulk and the number of trapped positrons $n_t = 0$ at $t = 0$, these equations can be solved to represent the measured positron lifetime spectrum as

$$N(t) = I_1 \exp(-t/\tau_1) + I_2 \exp(-t/\tau_2), \tag{5}$$

where $\tau_1 = (\lambda_b + \kappa_t)^{-1}$ and $\tau_2 = \lambda_t^{-1}$ are the two measured positron lifetimes and $I_1 + I_2 = 100\%$.

4. Results

The range of 116 MeV O^{5+} in Zr–1Nb is estimated to be around 66 μm by SRIM 2003 (Biersack and Haggman 1980). The radiation damage was assayed by the damage energy deposited causing displacement of atoms. Figure 1 shows the total target displacement of the collision events in Zr–1Nb alloy estimated using SRIM 2003. The maximum dpa at the peak region for the sample at a dose of 8×10^{18} O^{5+}/m^2 was found to be 0·15.

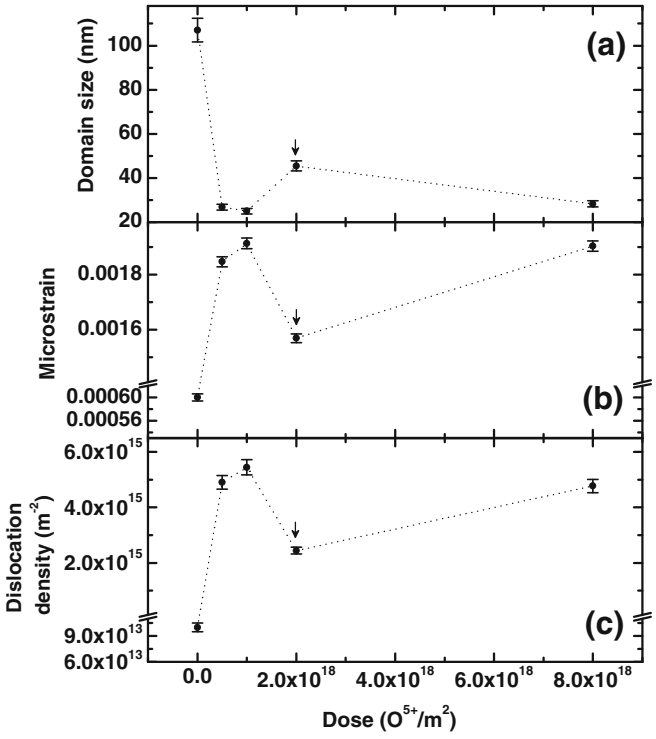

Figure 5. Variation of **(a)** average domain size, **(b)** average microstrain and **(c)** average dislocation density with different irradiation doses.

4.1 *X-ray diffraction line profile analysis (XRDLPA)*

Figure 2 represents the typical X-ray diffraction profiles of the unirradiated sample and the sample irradiated to a dose of 8×10^{18} O^{5+}/m^2. The broadening seen clearly in the XRD profile (inset of figure 2) of the irradiated sample has resulted

Table 1. Effective domain size, microstrain and dislocation density along different crystallographic planes for the Zr–1Nb sample irradiated to different doses (O^{5+}/m^2).

Dose (O^{5+}/m^2)	Domain size (nm) Error = ±2					Microstrain (10^{-3}) Error = ± 10^{-5}					Dislocation density (10^{15}) (m^{-2}) Error = ±(5.4×10^{13})				
	Unirradiated	5×10^{17}	1×10^{18}	2×10^{18}	8×10^{18}	Unirradiated	5×10^{17}	1×10^{18}	2×10^{18}	8×10^{18}	Unirradiated	5×10^{17}	1×10^{18}	2×10^{18}	8×10^{18}
002	107	30	30	51	34	0·6	1·91	1·94	1·52	1·94	0·1	4·52	4·60	2·10	4·05
101	106	30	26	46	34	0·6	1·86	1·95	1·55	1·70	0·2	4·37	5·24	2·39	3·52
102	109	30	29	49	34	0·7	1·89	1·94	1·53	1·85	0·1	4·46	4·83	2·20	3·84
103	111	30	29	50	34	0·7	1·90	1·94	1·53	1·89	0·2	4·49	4·71	2·15	3·95
112	107	29	26	47	32	0·7	1·88	1·92	1·54	1·89	0·2	4·66	5·16	2·32	4·24

due to the microstructural changes (particularly in the domain size and microstrain) caused by heavy ion irradiation.

Figure 3 shows the W–H plot for the unirradiated and the irradiated Zr–1Nb samples at different doses. The points corresponding to each crystallographic plane are found to be scattered in the plots for the unirradiated sample and also for the sample irradiated at a dose of 5×10^{17} O^{5+}/m^2. This scattered nature of the points in the plots implies a strong anisotropy in the domain size and microstrain along different crystallographic directions. But with increasing dose of irradiation, the points in the plots are found to be less scattered and almost shows a linear trend at the dose of 2×10^{18} O^{5+}/m^2. However, the relative intensities of the XRD peaks did not change much due to irradiation at different doses, which indicate that the initial texture has not changed due to irradiation. Hence, the scattered nature of the W–H plots is mainly due to changes in the microstructural parameters like domain size and microstrain caused by irradiation.

Figure 4 shows a typical Rietveld fit for the Zr–1Nb sample with highest dose of irradiation (8×10^{18} O^{5+}/m^2). The variations of D_s, $\langle \varepsilon_L^2 \rangle^{1/2}$ and ρ as a function of irradiation dose obtained from the modified Rietveld method have been shown in figure 5. A sharp decrease in the domain size (figure 5a) and increase in the microstrain (figure 5b) are observed at the initial stages of irradiation which tends to saturate at higher irradiation doses except at a dose of 2×10^{18} O^{5+}/m^2 (marked by arrow). Figure 5(c) reveals the variation of dislocation density as a function of irradiation dose. The density of dislocation increases with dose but shows an anomaly at that particular dose of 2×10^{18} O^{5+}/m^2. The values of the effective domain size D_e, microstrain and dislocation density along different crystallographic planes are shown in table 1. These data in table 1 also show the anomaly at the same dose of irradiation.

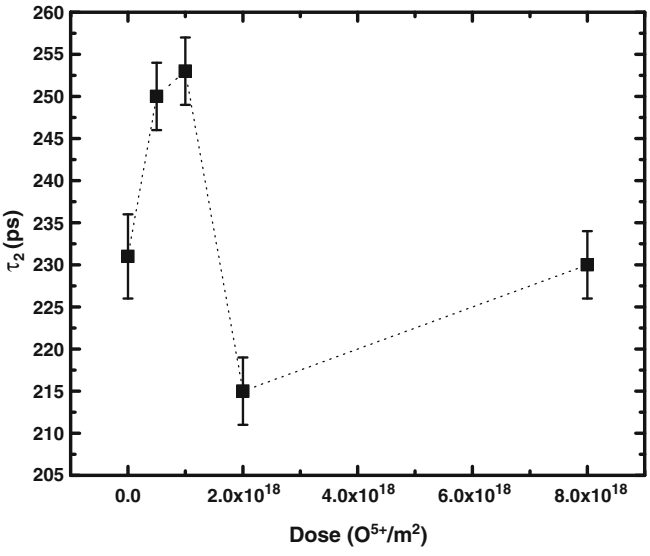

Figure 6. Variation of τ_2 with irradiation doses.

Table 2. Values of τ_1, τ_2 and I_2 for the unirradiated and irradiated samples.

Irradiation doses (O^{5+}/m^2)	τ_1 (ps)	τ_2 (ps)	I_2
Unirradiated	128 ± 3	231 ± 5	$43{\cdot}4 \pm 3{\cdot}4$
5×10^{17}	132 ± 2	250 ± 4	$47{\cdot}7 \pm 2{\cdot}4$
1×10^{18}	137 ± 3	253 ± 4	$50{\cdot}7 \pm 2{\cdot}8$
2×10^{18}	119 ± 4	215 ± 4	$56{\cdot}1 \pm 3{\cdot}8$
8×10^{18}	125 ± 4	230 ± 4	$52{\cdot}3 \pm 3{\cdot}7$

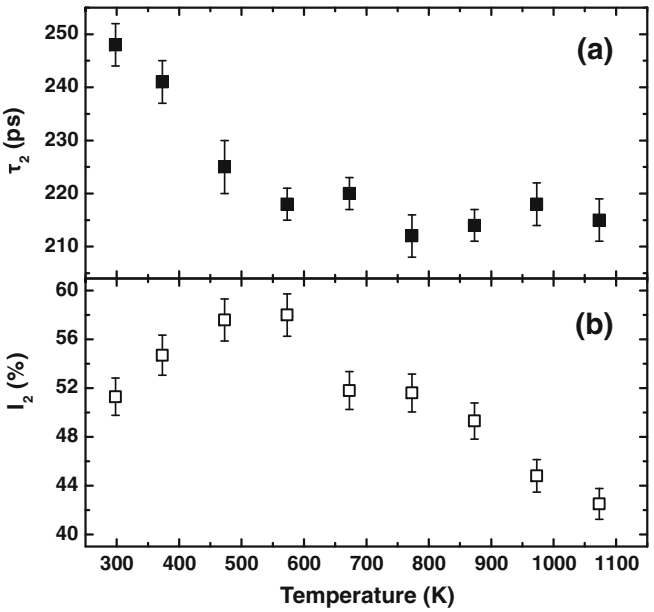

Figure 7. Variation of **(a)** τ_2 and **(b)** I_2 with isochronal annealing temperature.

4.2 *Positron annihilation spectroscopy (PAS)*

The variation of the positron life time τ_2 as a function of irradiation dose is shown in figure 6. In this case also, we observe similar kind of anomaly at the same dose of irradiation (2×10^{18} O^{5+}/m^2). The values of τ_1, τ_2 and I_2 found from the PAS study are listed in table 2.

Isochronal annealing studies by PAS have been performed on the sample with a dose of 1×10^{18} O^{5+}/m^2. Figure 7(a) shows the variation of τ_2 with respect to the annealing temperature. We observed a drastic fall of τ_2 up to a temperature of 573 K, followed by saturation to 215 ps at higher annealing temperatures. The variation of I_2 with temperature is shown in figure 7(b), which exhibits a peak at 573 K.

5. Discussion

The radiation damage by heavy ions (O^{5+}) is essentially characterized by the displacement cascade consisting of highly localized interstitials and vacancies. These mobile point defects interact with the microstructure by long range diffusion (Abromeit *et al* 1994). The main mechanism of the migration of point defects and their annihilation are based on three reaction paths (i) the loss of point defects at extended sinks such as surfaces, grain boundaries, and at the network of the existing dislocations, (ii) the nucleation of the clusters by the homogeneous reaction between the point defects of the same type and (iii) the growth of the defect clusters like the dislocation loops and voids by agglomeration of the point defects.

In the irradiated sample, the enhancement of radiation induced diffusion is solely responsible for the migration of vacancies, their agglomeration and collapsing in the shape of dislocation loops. The generation of dislocation by collapsing of vacancy clusters is only possible when there is vacancy concentration in excess of the equilibrium values. We could observe an order of magnitude increase in the density of dislocation at the initial stages of irradiation, which in turn can act as a sink for vacancies. Hence, the annihilation of vacancies also takes place during irradiation as a competing process to the generation of vacancies. With the increase in dose of irradiation, the annihilation of vacancies increases because of the formation of new dislocation loops due to the collapse of vacancy clusters. When the rate of annihilation of vacancies is comparable to the rate of its generation, a saturation of the dislocation density occurs. This effect has also been observed in our earlier studies on Zr–1Sn–1Nb–0·1Fe (Sarkar *et al* 2008; Mukherjee *et al* 2002, 2005) irradiated with $Ne^{6+}$and O^{5+} ions. But in case of proton (light ion) irradiation studies (Mukherjee *et al* 2001), we did not observe any clustering beyond trivacancy clusters even up to the highest dose of irradiation characterized by PAS. We also did not observe any significant change in the dislocation density in the proton irradiated Zr–1Nb–1Sn–0·1Fe samples (Mukherjee *et al* 2001).

In our present work, we have observed a sudden decrease in the dislocation density at a specific irradiation dose of 2×10^{18} O^{5+}/m^2 (figure 5c). To explain this anomaly we take recourse to the PAS results obtained in our samples. From figure 6, the value of the positron life time in the unirradiated sample (231 ps) corresponds to that of a monovacancy in pure Zr (228 ps) as reported in the literature (Campillo Robles *et al* 2007). The value of τ_2 in the irradiated samples indicates the presence of mono and di-vacancies except again at a dose of 2×10^{18} O^{5+}/m^2 where the value is 215 ps. This low value of τ_2 indicates that there are no dominant vacancies at this dose and thus can be attributed to the presence of dislocation loops alone (Hatakeyama *et al* 2009). The absence of vacancies and the lower value of dislocation density at this dose (figure 5c) can be explained as follows. At the particular dose of irradiation, if the rate of annihilation of vacancies into the sink (dislocation loops) dominates over the rate of their creation, a situation may arise where all the vacancies that are created gets annihilated in the sinks thus lowering the sink density (dislocation density) itself. In our earlier studies of irradiation on Zr–1Sn–1Nb–0·1Fe (Mukherjee *et al* 2002;

Sarkar *et al* 2008) by Ne^{6+} and O^{5+} energetic ions we did not observe this anomaly.

In case of the isochronal annealing studies on the 1×10^{18} O^{5+}/m^2 sample, the drastic fall of τ_2 (figure 7a) up to a temperature of 573 K has been observed due to the annihilation of the vacancies. As observed in figure 7(b), the initial increase in I_2 can be attributed to the increase in the concentration of mono-vacancies resulting from the dissociation of vacancy-impurity complexes. Upadhyaya and Muraleedharan (1987) observed the dissociation of vacancy–impurity complexes in Zr–0·5Nb system around a temperature of 523 K. According to Cottrell (1967), the following relation approximately describes the binding energy of a vacancy with a foreign atom which has a size misfit, "η", with the matrix lattice:

$$E_b = 8\pi\mu r_0^3 \eta^2, \tag{6}$$

where μ is the shear modulus of the matrix, r_0 the matrix atom radius and

$$\eta = \pm\left(\frac{r_1 - r_0}{r_0}\right), \tag{7}$$

where r_1 is the impurity atom radius. Using (6), E_b for vacancy–niobium complexes in zirconium matrix is found to be around 0·08 eV which corresponds to a temperature around 619 K. This value approximately matches with the peak temperature observed in figure 7(b).

6. Conclusions

The microstructural parameters like average domain size, microstrain and dislocation density of the 116 MeV O^{5+} irradiated Zr–1Nb alloy have been obtained reliably using XRDLPA in the low dose regime. An anomaly was observed in the value of these parameters at a specific dose of 2×10^{18} O^{5+}/m^2 which indicates that the irradiation induced microstructure in this alloy is very much dose dependent in this low dose regime. PAS results also reveal the same anomaly at this specific dose corroborating the above results. Isochronal annealing studies using PAS gives the signature of the presence of vacancy–solute atom complexes at the initial stages of annealing, which gets dissociated at higher annealing temperatures.

References

Abromeit C 1994 *J. Nucl. Mater.* **216** 78

Biersack J P and Haggmark L G 1980 *Nucl. Instrum. Methods* **174** 257 (The Stopping and Range of Ions in Matter (SRIM 2000) software developed by Ziegler J and Biersack J P is available on the Website http://www.research.ibm.com/ionbeams)

Campillo Robles J M, Ogando E and Plazaola F 2007 *J. Phys. Condens. Matter* **19** 176222

Cottrell A H 1967 *An introduction to metallurgy* (London: Edward Arnold)

Dollase W A 1986 *J. Appl. Crystallogr.* **19** 267

Hatakeyama M, Toyama T, Yang J, Nagai Y, Hasegawa M, Ohkubo T, Eldrup M and Singh B N 2009 *J. Nucl. Mater.* **386** 852

Hautojarvi P and Corbel C 1995 *Positron spectroscopy of defects in metals and semiconductors*, in *Positron spectroscopy of solids* (eds) A Dupasquier and AP Mills, IOS press, p. 491

Lutterotti L and Scardi P 1990 *J. Appl. Crystallogr.* **23** 246

Mukherjee P, Nambissan P M G, Sen Pintu, Barat P and Bandyopadhyay S K 1999 *J. Nucl. Mater.* **273** 338

Mukherjee P, et al 2001 *J. Nucl. Mater.* **297** 341

Mukherjee P, Barat P, Bandyopadhyay S K, Sen P, Chottopadhyay S K, Chatterjee S K and Mitra M K 2002 *J. Nucl. Mater.* **305** 169

Mukherjee P, Sarkar A and Barat P 2005 *Mater. Char.* **55** 412

Nikulina A V, Markelov V A, Peregud M M, Voevodin V N, Panchenko V L and Kobylyansky G P 1996 *J. Nucl. Mater.* **238** 205

Sabol G, Klip G R, Balfour M G and Roberts E 1989 *Zirconium in nuclear industry*, *Eighth international symposium* (ASTM STP), Philadelphia, **1023** 227

Sabol G P, Schoenberger G and Balfour M G 1991 *IAEA tech. comm. meeting on materials for advanced water-cooled reactors*, *Plzen, Czech and Slovak Federal Republic*, IAEA, p. 50

Sarkar A, Mukherjee P and Barat P 2008 *J. Nucl Mater.* **372** 285

Upadhyaya D D and Muraleedharan R V 1987 *Bull. Mater. Sci.* **9** 235

Will G, Belloto M, Parrish W and Hatr M 1988 *J. Appl. Crystallogr.* **21** 182

Williamson G K and Hall W H 1953 *Acta Metall.* **1** 22

Williamson G K and Smallman R E 1956 *Philos. Mag.* **1** 34